



Fersch, R. G. et al. (0217) Determination of the proton spin structure functions for $0.05 < Q^2 < 5 \text{ GeV}^2$ using CLAS. Physical Review C, 96(6), 065208.

There may be differences between this version and the published version. You are advised to consult the publisher's version if you wish to cite from it.

<http://eprints.gla.ac.uk/157014/>

Deposited on: 9 February 2018

Enlighten – Research publications by members of the University of Glasgow_
<http://eprints.gla.ac.uk>

Determination of the proton spin structure functions for $0.05 < Q^2 < 5 \text{ GeV}^2$ using CLAS

R.G. Fersch,^{45, 7} N. Guler,^{31, 37} P. Bosted,^{39, 45} A. Deur,³⁹ K. Griffioen,⁴⁵ C. Keith,³⁹ S.E. Kuhn,³¹ R. Minehart,⁴⁴ Y. Prok,³¹ K.P. Adhikari,²⁶ S. Adhikari,¹¹ Z. Akbar,¹² M.J. Amarian,³¹ S. Anefalos Pereira,¹⁸ G. Asryan,⁴⁶ H. Avakian,^{39, 18} J. Ball,⁶ I. Balossino,¹⁷ N.A. Baltzell,³⁹ M. Battaglieri,¹⁹ I. Bedlinskiy,²³ A.S. Biselli,^{9, 4} W.J. Briscoe,¹⁴ W.K. Brooks,^{40, 39} S. Bültmann,³¹ V.D. Burkert,³⁹ Frank Thanh Cao,⁸ D.S. Carman,³⁹ S. Careccia,^{15, 31} A. Celentano,¹⁹ S. Chandavar,³⁰ G. Charles,³¹ T. Chetry,³⁰ G. Ciullo,^{17, 10} L. Clark,⁴² L. Colaneri,⁸ P.L. Cole,^{16, 39} N. Compton,³⁰ M. Contalbrigo,¹⁷ O. Cortes,¹⁶ V. Crede,¹² A. D'Angelo,^{20, 34} N. Dashyan,⁴⁶ R. De Vita,¹⁹ E. De Sanctis,¹⁸ C. Djalali,³⁶ G.E. Dodge,³¹ R. Dupre,²² H. Egiyan,^{39, 45} A. El Alaoui,⁴⁰ L. El Fassi,²⁶ L. Elouadrhiri,³⁹ P. Eugenio,¹² E. Fanchini,¹⁹ G. Fedotov,^{36, 35} A. Filippi,²¹ J.A. Fleming,⁴¹ T.A. Forest,¹⁶ M. Garçon,⁶ G. Gavalian,^{39, 27} Y. Ghandilyan,⁴⁶ G.P. Gilfoyle,³³ K.L. Giovanetti,²⁴ F.X. Girod,^{39, 6} C. Gleason,³⁶ E. Golovatch,³⁵ R.W. Gothe,³⁶ M. Guidal,²² L. Guo,^{11, 39} K. Hafidi,¹ H. Hakobyan,^{40, 46} C. Hanretty,³⁹ N. Harrison,³⁹ M. Hattawy,¹ D. Heddle,^{7, 39} K. Hicks,³⁰ M. Holtrop,²⁷ S.M. Hughes,⁴¹ Y. Ilieva,^{36, 14} D.G. Ireland,⁴² B.S. Ishkhanov,³⁵ E.L. Isupov,³⁵ D. Jenkins,⁴³ K. Joo,⁸ D. Keller,⁴⁴ G. Khachatryan,⁴⁶ M. Khachatryan,³¹ M. Khandaker,^{28, *} A. Kim,⁸ W. Kim,²⁵ A. Klein,³¹ F.J. Klein,⁵ V. Kubarovsky,^{39, 32} V.G. Lagerquist,³¹ L. Lanza,²⁰ P. Lenisa,¹⁷ K. Livingston,⁴² H.Y. Lu,³⁶ B. McKinnon,⁴² C.A. Meyer,⁴ M. Mirazita,¹⁸ V. Mokeev,^{39, 35} R.A. Montgomery,⁴² A. Movsisyan,¹⁷ C. Munoz Camacho,²² G. Murdoch,⁴² P. Nadel-Turonski,³⁹ S. Niccolai,²² G. Niculescu,²⁴ I. Niculescu,²⁴ M. Osipenko,¹⁹ A.I. Ostrovidov,¹² M. Paolone,³⁸ R. Paremuzyan,²⁷ K. Park,^{39, 25} E. Pasyuk,^{39, 2} W. Phelps,¹¹ J. Pierce,^{44, 29} S. Pisano,¹⁸ O. Pogorelko,²³ J.W. Price,³ D. Protopopescu,^{27, †} B.A. Raue,^{11, 39} M. Ripani,¹⁹ D. Riser,⁸ A. Rizzo,^{20, 34} G. Rosner,⁴² P. Rossi,^{39, 18} P. Roy,¹² F. Sabatié,⁶ C. Salgado,²⁸ R.A. Schumacher,⁴ Y.G. Sharabian,³⁹ A. Simonyan,⁴⁶ Iu. Skorodumina,^{36, 35} G.D. Smith,⁴¹ D. Sokhan,⁴² N. Sparveris,³⁸ I. Stankovic,⁴¹ S. Stepanyan,³⁹ I.I. Strakovsky,¹⁴ S. Strauch,³⁶ M. Taiuti,^{13, ‡} Ye Tian,³⁶ B. Torayev,³¹ M. Ungaro,^{39, 32} H. Voskanyan,⁴⁶ E. Voutier,²² N.K. Walford,⁵ D.P. Watts,⁴¹ X. Wei,³⁹ L.B. Weinstein,³¹ N. Zachariou,⁴¹ and J. Zhang^{39, 31}

(The CLAS Collaboration)

¹Argonne National Laboratory, Argonne, Illinois 60439, USA

²Arizona State University, Tempe, Arizona 85287-1504, USA

³California State University, Dominguez Hills, Carson, California 90747, USA

⁴Carnegie Mellon University, Pittsburgh, Pennsylvania 15213, USA

⁵Catholic University of America, Washington, D.C. 20064, USA

⁶Irfu/SPHn, CEA, Université Paris-Saclay, 91191 Gif-sur-Yvette, France

⁷Christopher Newport University, Newport News, Virginia 23606, USA

⁸University of Connecticut, Storrs, Connecticut 06269, USA

⁹Fairfield University, Fairfield, Connecticut 06824, USA

¹⁰Università di Ferrara, 44121 Ferrara, Italy

¹¹Florida International University, Miami, Florida 33199, USA

¹²Florida State University, Tallahassee, Florida 32306, USA

¹³Università di Genova, 16146 Genova, Italy

¹⁴The George Washington University, Washington, DC 20052, USA

¹⁵Georgia College, Milledgeville, Georgia 31061, USA

¹⁶Idaho State University, Pocatello, Idaho 83209, USA

¹⁷INFN, Sezione di Ferrara, 44100 Ferrara, Italy

¹⁸INFN, Laboratori Nazionali di Frascati, 00044 Frascati, Italy

¹⁹INFN, Sezione di Genova, 16146 Genova, Italy

²⁰INFN, Sezione di Roma Tor Vergata, 00133 Rome, Italy

²¹INFN, Sezione di Torino, 10125 Torino, Italy

²²Institut de Physique Nucléaire, CNRS/IN2P3 and Université Paris Sud, Orsay, France

²³Institute of Theoretical and Experimental Physics, Moscow, 117259, Russia

²⁴James Madison University, Harrisonburg, Virginia 22807, USA

²⁵Kyungpook National University, Daegu 41566, Republic of Korea

²⁶Mississippi State University, Mississippi State, Mississippi 39762-5167, USA

²⁷University of New Hampshire, Durham, New Hampshire 03824-3568, USA

²⁸Norfolk State University, Norfolk, Virginia 23504, USA

²⁹Oak Ridge National Laboratory, Oak Ridge, Tennessee 37830, USA

³⁰Ohio University, Athens, Ohio 45701, USA

³¹Old Dominion University, Norfolk, Virginia 23529, USA

³²Rensselaer Polytechnic Institute, Troy, New York 12180-3590, USA

³³University of Richmond, Richmond, Virginia 23173, USA

³⁴Università di Roma Tor Vergata, 00133 Rome, Italy

³⁵Skobeltsyn Institute of Nuclear Physics, Lomonosov Moscow State University, 119234 Moscow, Russia

³⁶University of South Carolina, Columbia, South Carolina 29208, USA

³⁷*Spectral Sciences Inc., 01803 Burlington, Massachusetts, USA*

³⁸*Temple University, Philadelphia, Pennsylvania 19122, USA*

³⁹*Thomas Jefferson National Accelerator Facility, Newport News, Virginia 23606, USA*

⁴⁰*Universidad Técnica Federico Santa María, Casilla 110-V Valparaíso, Chile*

⁴¹*Edinburgh University, Edinburgh EH9 3JZ, United Kingdom*

⁴²*University of Glasgow, Glasgow G12 8QQ, United Kingdom*

⁴³*Virginia Tech, Blacksburg, Virginia 24061-0435, USA*

⁴⁴*University of Virginia, Charlottesville, Virginia 22901, USA*

⁴⁵*College of William and Mary, Williamsburg, Virginia 23187-8795, USA*

⁴⁶*Yerevan Physics Institute, 375036 Yerevan, Armenia*

(Dated: January 15, 2018)

We present the results of our final analysis of the full data set of $g_1^p(Q^2)$, the spin structure function of the proton, collected using CLAS at Jefferson Laboratory in 2000–2001. Polarized electrons with energies of 1.6, 2.5, 4.2 and 5.7 GeV were scattered from proton targets ($^{15}\text{NH}_3$ dynamically polarized along the beam direction) and detected with CLAS. From the measured double spin asymmetries, we extracted virtual photon asymmetries A_1^p and A_2^p and spin structure functions g_1^p and g_2^p over a wide kinematic range ($0.05 \text{ GeV}^2 < Q^2 < 5 \text{ GeV}^2$ and $1.08 \text{ GeV} < W < 3 \text{ GeV}$), and calculated moments of g_1^p . We compare our final results with various theoretical models and expectations, as well as with parametrizations of the world data. Our data, with their precision and dense kinematic coverage, are able to constrain fits of polarized parton distributions, test pQCD predictions for quark polarizations at large x , offer a better understanding of quark-hadron duality, and provide more precise values of higher-twist matrix elements in the framework of the operator product expansion.

PACS numbers: 13.60.Hb, 13.88.+e, 14.20.Dh

Keywords: Spin structure functions, nucleon structure

I. INTRODUCTION

Understanding the structure of the lightest stable baryon, the proton, in terms of its fundamental constituents, quarks and gluons, is a long-standing goal at the intersection of particle and nuclear physics. In particular, the decomposition of the total spin of the nucleon, $J = \frac{1}{2}$, into contributions from quark and gluon helicities and orbital angular momentum still remains an open challenge 30 years after the discovery of the “spin puzzle” by the European Muon Collaboration [1]. Although deep-inelastic electron and muon scattering (DIS), semi-inclusive DIS (SIDIS), proton-proton collisions, deeply virtual Compton scattering (DVCS) and deeply virtual meson production (DVMP), have all been used to understand nucleon spin, inclusive polarized lepton scattering remains the benchmark for the study of longitudinal nucleon spins. The inelastic scattering cross section can be described in the Born approximation (1-photon exchange) by four structure functions (F_1^p, F_2^p, g_1^p and g_2^p), all of which depend only on Q^2 , the 4-momentum transfer squared, and ν , the virtual photon energy. Two of these, g_1^p and g_2^p , carry fundamental information about the spin-dependent structure of the nucleon. The status of the world data for g_1^p and g_2^p and their theoretical interpretation are reviewed in Refs. [2, 3].

The new experimental data from Jefferson Laboratory

(JLab) reported in this paper, expand significantly the kinematic range over which g_1^p for the proton is known to high precision. In particular, data were collected down to the rather small $Q^2 \approx 0.05 \text{ GeV}^2$, over a wide range of final-state masses, W , that include the resonance region ($1 \text{ GeV} < W < 2 \text{ GeV}$) and part of the DIS region, ($2 \text{ GeV} < W < 3 \text{ GeV}$ with $Q^2 > 1 \text{ GeV}^2$). The DIS data can serve as a low- Q^2 anchor for the extraction (see Ref. [4]) of polarized parton distribution functions (PDFs) within the framework of the next-to-leading order (NLO) evolution equations [5–7], and they can be used to pin down higher-twist contributions within the framework of the operator product expansion (OPE) [8–10]. They also can test various predictions for the asymptotic behavior of the asymmetry $A_1^p(x)$ as the momentum fraction $x \rightarrow 1$. The data in the resonance region reveal new information on resonance transition amplitudes (and their interference with the non-resonant background), and they can be used to characterize the transition from hadronic to partonic degrees of freedom as Q^2 increases (parton-hadron duality). Finally, various sum rules that constrain moments of g_1^p at both high and low Q^2 can be tested.

All data presented in this paper, referred to as the EG1b experimental run, were collected with the CEBAF Large Acceptance Spectrometer (CLAS) [11] in Jefferson Laboratory’s Hall B during the time period 2000–2001. Previously, a smaller data set in similar but more restrictive kinematics was obtained with CLAS in 1998; those proton and deuteron results were published in Refs. [12] and [13], respectively. The present data set was taken with beam energies of 1.6, 2.5, 4.2 and 5.7 GeV on polarized hydrogen ($^{15}\text{NH}_3$) and deuteron ($^{15}\text{ND}_3$) targets. The results on the deuteron are presented in Ref. [14]. Preliminary pro-

* Present address: Idaho State University, Pocatello, Idaho 83209, USA

† Present address: University of Glasgow, Glasgow G12 8QQ, United Kingdom

‡ Present address: INFN, Sezione di Genova, 16146 Genova, Italy

ton results from the highest and lowest beam energies were published previously [15–17]. The present paper includes, for the first time, the full data set collected with CLAS in 2000-2001 on the proton, and summarizes all details of the experiment and the final analysis.

The first data on spin structure functions at low W , including the resonance region, and at moderate Q^2 , were measured at SLAC and published in 1980 [18], followed by more precise data published by the E143 Collaboration in 1996 [19]. A comparable data set to the one presented here, covering a wide kinematic range, was collected for the neutron, using polarized ^3He as an effective neutron target and the spectrometers in Jefferson Laboratory's Hall A [20, 21]. A more restricted data set on the proton and deuteron at an average Q^2 of 1.3 GeV^2 , covering the resonance region with both transversely and longitudinally polarized targets, was acquired in Jefferson Lab's Hall C [22]. Precise g_1^p and g_1^d data from the CLAS EG1-dvcs experiment were published recently [23]. These results provided measurements of these structure functions at $Q^2 > 1 \text{ GeV}^2$, giving results at higher x than accessible in EG1b; results from EG1b in this publication complement these results by improving the precision of g_1^p at lower Q^2 in and near the resonance region.

In the following, we introduce the necessary formalism and theoretical background (Sec. II), describe the experimental setup (Sec. III), discuss the analysis procedures (Sec. IV), present the results for all measured and derived quantities, as well as models and comparison to theory (Sec. V), and summarize our conclusions (Sec. VI).

II. THEORETICAL BACKGROUND

A. Formalism

Cross sections for inclusive high energy electron scattering off a nucleon target with 4-momentum p^μ and mass M depend, in general, on the beam energy E , the scattered electron energy E' and the scattering angle θ (all defined in the laboratory frame with the proton initially at rest)¹, or, equivalently, on the three relativistically invariant variables

$$Q^2 = -q^2 = 4EE' \sin^2 \frac{\theta}{2}, \quad (1)$$

$$\nu = \frac{p \cdot q}{M} = E - E', \quad (2)$$

and

$$y = \frac{p \cdot q}{p \cdot k} = \frac{\nu}{E}, \quad (3)$$

in which $q^\mu = k^\mu - k'^\mu$ is the four-momentum carried by the virtual photon, which (in the Born approximation) is equal

to the difference between initial (k) and final (k') electron four-momenta.

The first two variables can be combined with the initial four-momentum of the target nucleon to calculate the invariant mass of the final state,

$$W = \sqrt{(p + q)^2} = \sqrt{M^2 + 2M\nu - Q^2}, \quad (4)$$

and the Bjorken scaling variable,

$$x = \frac{Q^2}{2p \cdot q} = \frac{Q^2}{2M\nu}, \quad (5)$$

which is interpreted as the momentum fraction of the struck parton in the infinite momentum frame.

The following combinations of these variables are also useful:

$$\gamma = \frac{2Mx}{\sqrt{Q^2}} = \frac{\sqrt{Q^2}}{\nu}, \quad (6)$$

$$\tau = \frac{\nu^2}{Q^2} = \frac{1}{\gamma^2}, \quad (7)$$

and the virtual photon polarization ratio

$$\begin{aligned} \epsilon &= \frac{2(1-y) - \frac{1}{2}\gamma^2 y^2}{(1-y)^2 + 1 + \frac{1}{2}\gamma^2 y^2} \\ &= \left(1 + 2[1 + \tau] \tan^2 \frac{\theta}{2}\right)^{-1}. \end{aligned} \quad (8)$$

B. Cross sections and asymmetries

In the Born approximation the cross section for inclusive electron scattering with beam and target spin parallel ($\uparrow\uparrow$) or antiparallel ($\uparrow\downarrow$) to the beam direction can be expressed in terms of the four structure functions F_1^p, F_2^p, g_1^p and g_2^p , all of which depend on ν and Q^2 :

$$\begin{aligned} \frac{d\sigma^{\uparrow\downarrow/\uparrow\uparrow}}{d\Omega dE'} &= \sigma_M \left[\frac{F_2^p}{\nu} + 2 \tan^2 \frac{\theta}{2} \frac{F_1^p}{M} \pm 2 \tan^2 \frac{\theta}{2} \right. \\ &\quad \times \left. \left(\frac{E + E' \cos \theta}{M\nu} g_1^p - \frac{Q^2}{M\nu^2} g_2^p \right) \right], \end{aligned} \quad (9)$$

where the Mott cross section

$$\sigma_M = \frac{4\alpha^2 E'^2}{Q^4} \cos^2 \frac{\theta}{2}, \quad (10)$$

where α is the electromagnetic fine structure constant. We can now define the double spin asymmetry $A_{||}$ as

$$A_{||}(\nu, Q^2) = \frac{d\sigma^{\uparrow\downarrow} - d\sigma^{\uparrow\uparrow}}{d\sigma^{\uparrow\downarrow} + d\sigma^{\uparrow\uparrow}}. \quad (11)$$

Introducing the ratio R^p of the absorption cross sections for longitudinal over transverse virtual photons (γ^*),

$$R^p = \frac{\sigma_L(\gamma^*)}{\sigma_T(\gamma^*)} = \frac{F_2^p}{2xF_1^p} (1 + \gamma^2) - 1, \quad (12)$$

¹ For beam and target polarization along the beam axis, the azimuth ϕ can be ignored since no observable can depend on it.

(where L and T represent longitudinal and transverse polarization, respectively) we can define two additional quantities,

$$\eta = \frac{\epsilon\sqrt{Q^2}}{E - E'\epsilon} \quad (13)$$

and the “depolarization factor”

$$D = \frac{1 - E'\epsilon/E}{1 + \epsilon R^p}, \quad (14)$$

which allow us to express $A_{||}$ in terms of the structure functions:

$$\frac{A_{||}}{D} = (1 + \eta\gamma) \frac{g_1^p}{F_1^p} + \gamma(\eta - \gamma) \frac{g_2^p}{F_1^p}. \quad (15)$$

Alternatively, the double spin asymmetry $A_{||}$ can also be interpreted in terms of the virtual photon asymmetries

$$A_1^p(\gamma^*) \equiv \frac{\sigma_T^{\frac{1}{2}}(\gamma^*) - \sigma_T^{\frac{3}{2}}(\gamma^*)}{\sigma_T^{\frac{1}{2}}(\gamma^*) + \sigma_T^{\frac{3}{2}}(\gamma^*)} = \frac{g_1^p - \gamma^2 g_2^p}{F_1^p} \quad (16)$$

and

$$A_2^p(\gamma^*) \equiv \frac{\sigma_{LT}}{\sigma_T} = \frac{2\sigma_{LT}(\gamma^*)}{\sigma_T^{\frac{1}{2}}(\gamma^*) + \sigma_T^{\frac{3}{2}}(\gamma^*)} = \gamma \frac{g_1^p + g_2^p}{F_1^p}. \quad (17)$$

Here, $\sigma_T^{\frac{1}{2}}(\gamma^*)$ and $\sigma_T^{\frac{3}{2}}(\gamma^*)$ represent the transversely polarized photon cross-sections for production of spin- $\frac{1}{2}$ and spin- $\frac{3}{2}$ final hadronic states, respectively, and $\sigma_{LT}(\gamma^*)$ is the interference cross-section between longitudinal and transverse virtual photons. Note that both unpolarized structure functions F_1^p and F_2^p [as implicitly contained in D ; see Eqs. (12) and (14)] are contained in the definition of these asymmetries. Here, A_1^p is the asymmetry for transverse (virtual) photon absorption on a nucleon with total final-state spin projection $\frac{1}{2}$ or $\frac{3}{2}$ along the incoming photon direction, and A_2^p is an interference asymmetry between longitudinally and transversely polarized virtual photon absorption. The relationship to the measured quantity $A_{||}$ is

$$A_{||}(\nu, Q^2) = D[A_1^p(\nu, Q^2) + \eta A_2^p(\nu, Q^2)]. \quad (18)$$

$A_{||}$ is the primary observable determined directly from the data described in this paper. The structure functions g_1^p, g_2^p and the virtual photon asymmetries A_1^p, A_2^p are extracted from these asymmetries. In particular, given a model or data for F_1^p, R^p and A_2^p , A_1^p can be extracted directly using Eq. (18), and g_1^p can be extracted using

$$g_1^p = \frac{\tau}{1 + \tau} \left(\frac{A_{||}}{D} + (\gamma - \eta) A_2^p \right) F_1^p. \quad (19)$$

A simultaneous extraction of both asymmetries A_1^p and A_2^p from measurements of $A_{||}$ alone is possible by exploiting the dependence of the factors D and η in Eqs. (15) and (18) on the beam energy for the same kinematic point (ν, Q^2) . This is the super-Rosenbluth separation of Sec. VB.

C. Virtual photon absorption asymmetries

Data on the virtual photon absorption asymmetries A_1^p and A_2^p are of great interest in both the nucleon resonance and DIS regions.

For inelastic scattering leading to specific final (resonance) states, A_1^p can be interpreted in terms of the helicity structure of the transition from the nucleon ground state to the final state resonance. If the final state has total spin $S = \frac{1}{2}$, the absorption cross section $\sigma_T^{\frac{3}{2}}(\gamma^*)$ leading to final spin projection $S_z = \frac{3}{2}$ along the virtual photon direction obviously cannot contribute, requiring $A_1^p = 1$ [see Eq. (16)]. Vice versa, excitations of spin $S = \frac{3}{2}$ resonances like the $\Delta(1232)$ receive a strong contribution from $\sigma_T^{\frac{3}{2}}(\gamma^*)$ and therefore can have a negative A_1^p . Both A_1^p and A_2^p are directly related to the helicity transition amplitudes, $A_{\frac{3}{2}}(\nu, Q^2)$ (transverse photons leading to final-state helicity $\frac{3}{2}$), $A_{\frac{1}{2}}(\nu, Q^2)$ (transverse photons leading to final-state helicity $\frac{1}{2}$), and $S_{\frac{1}{2}}^*(\nu, Q^2)$ (longitudinal photons):

$$A_1^p = \frac{|A_{\frac{1}{2}}|^2 - |A_{\frac{3}{2}}|^2}{|A_{\frac{1}{2}}|^2 + |A_{\frac{3}{2}}|^2} \quad \text{and} \quad (20)$$

$$A_2^p = \sqrt{2} \frac{\sqrt{Q^2}}{q^*} \frac{S_{\frac{1}{2}}^* A_{\frac{1}{2}}}{|A_{\frac{1}{2}}|^2 + |A_{\frac{3}{2}}|^2}. \quad (21)$$

Here, q^* is the (virtual) photon three-momentum in the rest frame of the resonance. As an example, the $\Delta(1232)$ is excited by a (nearly pure) $M1$ transition at low Q^2 , with $A_{\frac{3}{2}} \approx \sqrt{3}A_{\frac{1}{2}}$ and therefore $A_1^p \approx -0.5$. In general, the measured asymmetries A_1^p and A_2^p at a given value of W provide information on the relative strengths of overlapping resonance transition amplitudes and the non-resonant background. By looking at the Q^2 -dependence of the asymmetry for a specific $S = \frac{3}{2}$ resonance (e.g., the D_{13}), one can study the transition from $A_{\frac{3}{2}}$ dominance at small Q^2 (including real photons) to the $A_{\frac{1}{2}}$ dominance expected from quark models and perturbative quantum chromodynamics (pQCD) at large Q^2 .

In the DIS region, $A_1^p(x)$ can yield information on the polarization of the valence quarks at large x . In a simple SU(6)-symmetric quark model, with three constituent quarks at rest, the polarization of valence up and down quarks yields $A_1^p(x) = 5/9$. Most realistic models predict that $A_1^p(x) \rightarrow 1$ as $x \rightarrow 1$, implying that a valence quark, which carries nearly all of the nucleon momentum in the infinite momentum frame, will be polarized along the proton's spin direction. However, the approach to the limit $x = 1$ is quite different for different models. In particular, relativistic constituent quark models [24] predict a much slower rise towards $A_1^p = 1$ than pQCD calculations [25, 26] that incorporate helicity conservation. Modifications of the pQCD picture to include orbital angular momentum [27] show an intermediate rise towards $x = 1$. Precise measurements of

A_1^p at large x in the DIS region are therefore of high importance.

The asymmetry A_2^p is not very well-known in the DIS region, and it has no simple interpretation. However, it is constrained by the Soffer inequality [28, 29]

$$|A_2^p| \leq \sqrt{R^p (1 + A_1^p)/2}. \quad (22)$$

Data on A_1^p have been extracted by collaborations at CERN, SLAC and DESY [1, 19, 30–41] (mostly in the DIS region), as well as by collaborations at Jefferson Laboratory [15, 17, 21, 42]. Data on A_2^p from the same labs and MIT Bates are more limited in the Q^2 range covered [22, 37, 41, 43–49].

D. The spin structure function $g_1^p(x, Q^2)$

In a simple quark-parton model, the structure function $g_1^p(x)$ is independent of Q^2 , and can be interpreted in terms of the difference $\Delta q(x) = q \uparrow(x) - q \downarrow(x)$ of parton densities for quarks with helicity aligned versus antialigned with the overall longitudinal nucleon spin, as a function of the momentum fraction x carried by the struck quark. In particular, for the proton

$$g_1^p(x) = \frac{1}{2} \sum_j e_j^2 [\Delta q_j(x) + \Delta \bar{q}_j(x)] \quad (23)$$

where the sum goes over all relevant quark flavors (up, down, strange, etc.) for quark densities q_j , and e_j are the corresponding electric charges (2/3, -1/3, -1/3, ...).

Within QCD, this picture is modified in two important ways:

1. The coupling of the virtual photon to the quarks is modified by QCD radiative effects (e.g., gluon emission).
2. The parton densities $\Delta q_j(x, Q^2)$ and $\Delta \bar{q}_j(x, Q^2)$, and hence $g_1^p(x, Q^2)$, become (logarithmically) dependent on the resolution Q^2 of the probe, as described by the DGLAP (Dokshitzer-Gribov-Lipatov-Altarelli-Parisi) evolution equations [5–7]. At NLO and higher, these equations couple quark and gluon PDFs at lower Q^2 to those at higher Q^2 via the so-called splitting functions. Therefore, measuring the Q^2 dependence of g_1^p with high precision over a wide range in Q^2 can yield additional information on the spin structure of the nucleon, including the contribution of the gluon helicity distribution $\Delta G(x)$.

Accurate data are therefore needed at both the highest accessible Q^2 (presently from the COMPASS Collaboration at CERN) and the lowest Q^2 that is still consistent with the pQCD description of DIS (the data taken at Jefferson Laboratory). In the region of lower Q^2 , additional scaling violations occur due to higher-twist contributions and target mass corrections, leading to correction terms proportional to

powers of $1/Q$. These corrections can be extracted from our data since they cover seamlessly the transition from $Q^2 \ll 1$ GeV² to the scaling region $Q^2 > 1$ GeV². An additional complication arises because at moderate to high x , low Q^2 corresponds to the region of the nucleon resonances ($W < 2$ GeV). In this case, one would expect the quark-parton description of g_1^p to break down, and hadronic degrees of freedom (resonance peaks and troughs) to dominate the behavior of $g_1^p(x)$, analogous to the asymmetry A_1^p discussed above.

Bloom-Gilman duality

Bloom and Gilman observed [50] that the unpolarized structure function $F_2^p(x, Q^2)$ in the resonance region resembles, on average, the same structure function at much higher Q^2 , in the DIS region, where the quark-parton picture applies. This agreement, which improves if one plots the data against the Nachtmann variable [51]

$$\xi = \frac{Q^2}{M(\nu + \sqrt{Q^2 + \nu^2})} = \frac{|\vec{q}| - \nu}{M}, \quad (24)$$

(where $|\vec{q}|$ is the magnitude of the virtual photon 3-momentum) is one example of “quark-hadron duality,” where both quark-parton and hadronic interpretations of the same data are possible. De Rujula *et al.* [52, 53] interpreted this duality as a consequence of relatively small higher-twist contributions to the structure functions. Duality has been observed both for the integral of structure functions over the whole resonance region, $W < 2$ GeV (“global duality”), as well as for averages over individual resonances (“local duality”) [54].

Initial duality data on polarized structure functions from SLAC [37] and HERMES [55, 56] have been followed by much more detailed examinations of duality in this case by experiments at Jefferson Laboratory [12, 22, 57], including results from a partial analysis of the present data set [16]. Reference [54] summarizes the conditions under which duality has been found to hold at least approximately. The complete data set discussed in this paper increases substantially the kinematic range over which high-precision data exist in the resonance region and beyond, and can be compared to extrapolations from the DIS region. A full analysis accounting for QCD scaling violations and target mass effects [58] can make this comparison more rigorous and quantitative.

E. The spin structure function $g_2^p(x, Q^2)$

The second spin-dependent structure function in inclusive DIS, $g_2^p(x, Q^2)$, does not have an intuitive interpretation in the quark-hadron picture. The sum of $g_1^p + g_2^p = g_T$ is proportional to A_2^p [Eq. (17)] and has a leading-twist contribution according to the Wandzura-Wilczek relation [59],

$$\bar{g}_T(x, Q^2) = \int_x^1 \frac{\bar{g}_1(y, Q^2)}{y} dy, \quad (25)$$

and a very small contribution from transverse quark polarization (which is suppressed by the small quark masses). Here, the notation \bar{g} denotes contributions from leading twist only. The higher twist contributions to g_T (and hence g_2^p) can be sizable, and they are not suppressed by powers of $1/Q$, which makes g_T or g_2^p a good experimental quantity with which to study quark-gluon correlations. In particular, the third moment,

$$d_2 = 3 \int_0^1 x^2 [g_T(x) - \bar{g}_T(x)] dx, \quad (26)$$

is directly proportional to a twist-3 matrix element that is connected to the so-called “color polarizabilities” χ_E and χ_B (see Sec. II G) and has recently been linked to the average transverse force on quarks ejected from a transversely polarized nucleon [60]. Finally, the Burkhardt-Cottingham sum rule [61] predicts that the integral

$$\int_0^{1+\epsilon} g_2^p(x, Q^2) dx = 0 \quad (27)$$

at all Q^2 , in which the upper integration limit $1+\epsilon$ indicates the inclusion of the elastic peak at $x = 1$.

The EG1b data on $A_{||}$ are not very sensitive to g_2^p or g_T , leading to relatively large statistical uncertainties on their extraction. For this reason, in this paper we only present limited results on g_2^p and no direct evaluations of the integrals, Eqs. (26) and (27). However, we use theoretical constraints [Eqs. (22) and (27)], and existing experimental data on g_2^p or A_2^p , to model $A_2^p(x, Q^2)$. We use this model to extract A_1^p and g_1^p from our data.

F. Elastic scattering

The virtual photon asymmetries A_1^p and A_2^p are also defined for elastic scattering from a nucleon N , $N(e, e')N$, and Eq. (18) applies in this case as well. Following our discussion in Sec. II C, $A_1^p = 1$ for elastic scattering, since the final state spin is $\frac{1}{2}$ and hence $\sigma_T^{\frac{3}{2}}(\gamma^*) = 0$. The elastic asymmetry A_2^p is given by

$$A_2^p(Q^2) = \sqrt{R^p} = \frac{G_E^p(Q^2)}{\sqrt{\tau} G_M^p(Q^2)}, \quad (28)$$

where G_E^p and G_M^p are the electric and magnetic Sachs form factors of the nucleon. This relationship can be used to determine the ratio G_E^p/G_M^p from double-polarized scattering; in our case, we use this ratio, which is well determined by JLab experiments [62, 63], to extract the product of beam and target polarization, $P_b P_t$:

$$A_{||}^{meas} = P_b P_t A_{||}^{theo}. \quad (29)$$

Here, $A_{||}^{meas}$ is the measured elastic double-spin asymmetry after all corrections for background contamination have been applied.

One can also extend the definition of $g_1^p(x)$ and $g_2^p(x)$ to include elastic scattering at $x = 1$ by adding the terms

$$g_1^{pel}(x, Q^2) = \frac{1}{2} \frac{G_E^p G_M^p + \tau G_M^{p^2}}{1 + \tau} \delta(x - 1) \quad \text{and} \\ g_2^{pel}(x, Q^2) = \frac{\tau}{2} \frac{G_E^p G_M^p - G_M^{p^2}}{1 + \tau} \delta(x - 1), \quad (30)$$

which yield finite contributions to the moments (integrals over x) that include the elastic contribution.

G. Moments

Moments of structure functions weighted by powers of x are useful quantities for investigating the QCD-structure of the nucleon. On the one hand, they can be connected, via sum rules, to local operators of quark currents or forward Compton scattering amplitudes. On the other hand, they are currently the only relevant quantities that can be calculated directly in lattice QCD or in effective field theories like chiral perturbation theory (χ PT).

The matrix element d_2 , introduced in Eq. (26), is one example of a moment (the third moment of a combination of g_1^p and g_2^p). In the following, we focus on moments of g_1^p since our data are most sensitive to this structure function. The most important moment is

$$\Gamma_1^p(Q^2) \equiv \int_0^1 g_1^p(x, Q^2) dx. \quad (31)$$

In the limit of very high Q^2 , this moment for the neutron (n) and the proton (p) is proportional to a combination of matrix elements of axial quark currents,

$$\Gamma_1^{p,n}(Q^2 \rightarrow \infty) = \pm \frac{1}{12} a_3 + \frac{1}{36} a_8 + \frac{1}{9} a_0, \quad (32)$$

in which $a_3 = g_A = 1.267 \pm 0.004$ (where g_A is the axial vector coupling constant) and $a_8 = F + D \approx 0.58 \pm 0.03$ (where F and D are SU(3) coupling constants) [64] are the isovector and flavor-octet axial charges of the nucleon, which have been determined from nucleon and hyperon β decay, and a_0 is the flavor-singlet axial charge, which measures the total contribution of quark helicities to the (longitudinal) nucleon spin,

$$S_z^{quarks} = \frac{1}{2} \Delta \Sigma = \frac{1}{2} a_0. \quad (33)$$

Combining Eq. (32) for the proton and the neutron yields the famous Bjorken sum rule [65, 66]:

$$\Gamma_1^p - \Gamma_1^n = \frac{1}{6} a_3 = 0.211. \quad (34)$$

At high but finite Q^2 , these moments receive pQCD corrections due to gluon radiative effects. At leading twist, this yields

$$\mu_2^p(Q^2) \equiv \Gamma_1^{p[LT]}(Q^2) = \\ = C_{ns}(Q^2) \left(\frac{1}{12} a_3 + \frac{1}{36} a_8 \right) + C_s(Q^2) \frac{1}{9} a_0(Q^2) \quad (35)$$

and

$$\mu_2^{p-n}(Q^2) \equiv \Gamma_1^{p[LT]}(Q^2) - \Gamma_1^{n[LT]}(Q^2) = C_{ns}(Q^2) \frac{1}{6} a_3. \quad (36)$$

Here, C_{ns} and C_s are flavor non-singlet and singlet Wilson coefficients [67] that can be expanded in powers of the strong coupling constant α_S and hence depend mildly on Q^2 , while the Q^2 dependence of the matrix element a_0 reflects the \overline{MS} renormalization scheme that is used here, in which $a_0 = \Delta\Sigma$, the contribution of the quarks to the nucleon spin.

At the even lower Q^2 of the present data, additional corrections due to higher-twist matrix elements proportional to powers of $1/Q$ become important. These matrix elements are discussed in the next section.

In addition to the leading first moment, odd-numbered higher moments of g_1^p can be defined as $\int_0^1 x^{n-1} g_1^p(x) dx$, $n = 3, 5, 7, \dots$. These moments are dominated by high x (valence quarks) and are thus particularly well determined by Jefferson Laboratory data. They can also be related to hadronic matrix elements of local operators or (in principle) evaluated using lattice QCD. In the following, we will make explicit use of the third moment, $a_2(Q^2) = \int_0^1 x^2 g_1^p(x, Q^2) dx$.

Higher twist and OPE

Higher-twist matrix elements reveal information about quark-gluon and quark-quark interactions, which are important for understanding quark confinement. A study of higher-twist matrix elements can be carried out in the OPE formalism, which describes the evolution of structure functions and their moments in the pQCD domain.

In OPE, the first moment of $g_1^p(x, Q^2)$ can be written as

$$\Gamma_1^p(Q^2) = \sum_{\tau=2,4,\dots} \frac{\mu_\tau(Q^2)}{Q^{\tau-2}}, \quad (37)$$

in which $\mu_\tau(Q^2)$ are sums of twist elements up to twist τ . The twist is defined as the mass dimension minus the spin of an operator. Twist elements greater than 2 can be related to quark-quark and quark-gluon correlations. Hence, they are important quantities for the study of quark confinement. The leading twist contribution is given by the twist-2 coefficient μ_2 defined in Eq. (35). The next-to-leading-order twist coefficient is

$$\mu_4(Q^2) = \frac{M^2}{9} [a_2(Q^2) + 4d_2(Q^2) + 4f_2(Q^2)], \quad (38)$$

in which a_2 (d_2) is a twist 2 (3) target mass correction that can be related to higher moments of g_1^p (g_1^p and g_2^p). The matrix element f_2 (twist-4) [8] can be extracted from the Q^2 -dependence of Γ_1^p . The matrix elements d_2 and f_2 are related to the color polarizabilities, which are the responses of the color magnetic and electric fields to the spin of the proton [68, 69],

$$\chi_E = \frac{2}{3}(2d_2 + f_2) \quad \text{and} \quad \chi_M = \frac{1}{3}(4d_2 - f_2). \quad (39)$$

Theoretical values for f_2 and the color polarizabilities have been calculated using quark models [70], QCD sum rules [71], and lattice QCD [72].

Moments at low Q^2

The first moment of g_1^p is particularly interesting since there is not only a sum rule for its high- Q^2 limit [Eq. (32)], but its approach to $Q^2 \rightarrow 0$ is governed by the Gerasimov-Drell-Hearn (GDH) sum rule [73, 74]. For real photons ($Q^2 = 0$) and nucleon targets, the GDH sum rule reads

$$\int_0^\infty \frac{d\nu}{\nu} [\sigma_T^{\frac{3}{2}}(\nu) - \sigma_T^{\frac{1}{2}}(\nu)] = -\frac{2\pi^2\alpha}{M^2} \kappa^2, \quad (40)$$

in which κ is the anomalous magnetic moment of the nucleon. This sum rule was based on a low-energy theorem for the forward spin-flip Compton amplitude $f_2(\nu)$ as $\nu \rightarrow 0$ which is connected to the left-hand side of Eq. (40) through a dispersion relation. The photon absorption cross sections $\sigma_T^{\frac{3}{2}, \frac{1}{2}}$ enter into A_1^p , A_2^p , g_1^p , and g_2^p [Eq. (16)], and consequently the GDH sum rule constrains the slope of the first moment³ of g_1^p as $Q^2 \rightarrow 0$:

$$\frac{d\Gamma_1^p(Q^2)}{dQ^2} = -\frac{\kappa^2}{8M^2}. \quad (41)$$

After generalizing the spin-dependent Compton amplitude to virtual photons, $S_1(\nu, Q^2)$, one can extend the GDH sum rule to non-zero Q^2 using a similar dispersion relation [75],

$$\frac{M^3}{4} S_1(0, Q^2) = \frac{2M^2}{Q^2} \Gamma_1^p(Q^2), \quad (42)$$

with $(M^3/4)S_1(0, Q^2) = -\kappa^2/4$ as $Q^2 \rightarrow 0$. $S_1(0, Q^2)$ can be expanded in a power series in Q^2 around $Q^2 = 0$. The coefficients of this expansion have been calculated up to NLO in χ PT [75], yielding predictions for both the first and second derivative of Γ_1^p near the photon point. Since χ PT can be considered as the low-energy effective field theory of QCD, Γ_1^p can extend our understanding of the strong interaction to lower Q^2 values inaccessible to pQCD.

² In this case, the elastic contribution Eq. (30) to the moment must be included; i.e., the integral must go over the range $[0 \dots 1 + \epsilon]$.

³ In the present context, all moments *exclude* the elastic contribution since it does not contribute to real photon absorption. Hence, $\Gamma_1^p(Q^2) \rightarrow 0$ as $Q^2 \rightarrow 0$.

Extending the analysis of low-energy Compton amplitudes to higher powers in ν , one can get additional sum rules [76]. In particular, one can generalize the forward spin polarizability, γ_0^p , to include virtual photons:

$$\gamma_0^p(Q^2) = \frac{16\alpha M^2}{Q^6} \int_0^1 x^2 [g_1^p(x, Q^2) - \gamma^2 g_2^p(x, Q^2)] dx. \quad (43)$$

This too can be calculated using χ PT [17, 77].

III. THE EXPERIMENT

The experiment was carried out at the Thomas Jefferson National Accelerator Facility (Jefferson Laboratory or JLab for short), using a longitudinally polarized electron beam with energies from 1.6 to 5.7 GeV, a longitudinally polarized solid ammonia target (NH_3 or ND_3), and the CEBAF Large Acceptance Spectrometer (CLAS). In this section, we present a brief overview of the experimental setup and methods of data collection.

A. The CEBAF polarized electron beam

The continuous-wave electron beam accelerator facility (CEBAF) at Jefferson Laboratory produced electron beams with energies ranging from 0.8 GeV to 5.7 GeV, polarizations up to 85%, and currents up to 300 μA . Detailed descriptions of the accelerator are given in Refs. [78–81].

Polarized electrons are produced by band-gap photoemission from a strained GaAs cathode. The circularly polarized photons for this process [82] are supplied by master-oscillator-power-amplifiers (MOPAs) or titanium:sapphire lasers configured in an ultra-high-vacuum system [79]. The circular polarization of the laser light can be reversed electronically by signals sent to a Pockels cell. A half-wave plate (HWP) can be inserted into the laser beam to change the polarization phase by 180° . The HWP was inserted and removed periodically throughout the experiment, to ensure that no polarity-dependent bias from the laser is present in the measured asymmetry.

The 100 keV electrons emerging from the GaAs entered the injector line [79, 83], where their energies were boosted prior to injection into the main accelerator, which consists of two superconducting linacs connected by recirculation arcs. Each linac segment contains a series of superconducting niobium radio frequency (RF) cavities, driven by 5 kW klystrons [78].

A harmonic RF separator system splits the interleaved beam bunches and delivers them to the appropriate experimental hall (A, B, or C) [78]. The electron current in Hall B ranged from 0.3 to 10 nA, selected according to the beam energy, the target type, and the spectrometer torus polarity.

B. Beam monitoring and beam polarimetry

The Hall B beam line incorporated several instruments to measure the intensity, position, and profile of the beam. A Faraday cup at the end of the beam line measured the absolute electron flux. A Møller polarimeter was inserted periodically into the beam to measure its polarization.

Three beam position monitors (BPMs) were located 36.0, 24.6, and 8.2 m upstream from the CLAS center. They measured the beam intensity and its position in the transverse xy plane. Each BPM was composed of three RF cavities. The BPM position measurements were cross-calibrated using the “harp” beam profile scanners—thin wires that were moved transverse to the beam direction—which also determined beam width and halo. One-second averages of the BPM outputs were used in a feedback loop to keep the beam centered on the target [11].

The beam electrons were collected by the Faraday Cup (FC) located 29.0 m downstream from the CLAS center. The FC was used to integrate the beam current. The FC was a lead cylinder with diameter of 15 cm and thickness of 75 radiation lengths (r.l.) placed co-axially to the beam line. Its weight was 4000 kg.

The charge collection in the FC [11] was coupled to the CLAS data acquisition system using a current-to-pulse rate converter. Both the total (ungated) and detector live-time-gated counts were recorded. The FC readout was also tagged by a helicity signal to normalize the current for different helicity states. The beam position monitors were periodically calibrated with the Faraday cup.

The Møller polarimeter, located at the entrance of Hall B, was used to measure the beam polarization. Møller polarimetry requires a target of highly magnetizable material in the beamline. Therefore, dedicated Møller data runs of approximately 30 min each were taken periodically throughout the experiment. The polarimeter consisted of a target chamber with a 25- μm -thick Permendur (49% Fe, 49% Co, 2% Va) foil oriented at $\pm 20^\circ$ with respect to the beam line, longitudinally polarized to 7.5% by a 120 G Helmholtz magnet [84]. Two quadrupoles separated the scattered electrons from the beam. Elastic electron-electron scattering coincidences were used to determine the beam polarization, from the well-known double spin asymmetry [85]. The Møller measurements typically had a statistical uncertainty of 1% and a systematic uncertainty of $\sim 2\text{--}3\%$ [11]. The average beam polarization was about 70%. Since we determined the product of beam and target polarization directly from our data, the Møller polarimeter served primarily to ensure that the beam remained highly polarized during the beam exposures, as well as to check the consistency of the polarization during the data analysis.

C. The polarized target [86]

Cylindrical targets filled with solid ammonia beads immersed in liquid ^4He were located at the center of CLAS, co-axial with the beam line. The protons in the ammonia

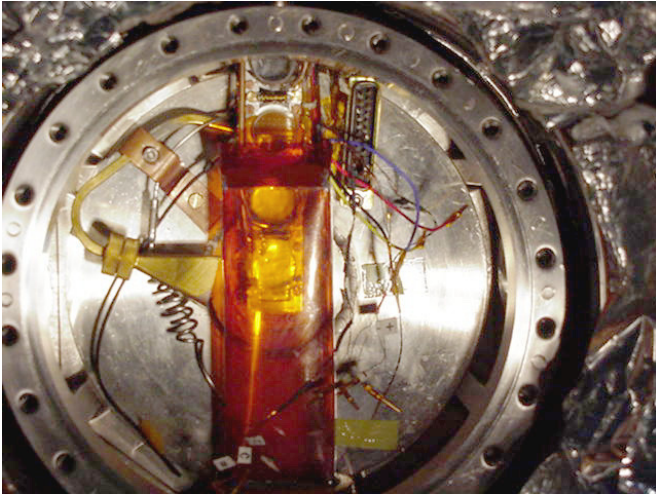


FIG. 1. (Color online) An internal view of the target chamber, viewed from upstream, showing the orange transparent Kapton cylindrical LHe minicup into which the target stick was inserted. Note the metal “horn,” the source of microwave emission, on the left side.

beads were polarized using the method of dynamic nuclear polarization (DNP), described in Refs. [87–89]. The required magnetic field was provided by a superconducting axial 5 T magnet (Helmholtz coils) whose field was uniform over the target, varying less than a factor of 10^{-4} over a cylindrical volume of 20 mm in length and diameter [86]. The target material was immersed in liquid helium (LHe) cooled to $\sim 1 - 1.5$ K using a ~ 0.8 -W ^4He evaporation refrigerator. The target system was contained in a cryostat designed to fit inside the central field-free region of CLAS, accessible for the insertion of the target material, and allowing detection of particles scattered into a 48° forward cone over the majority of the CLAS acceptance.

The cryostat contained four cylindrical target cells with axes parallel to the beam line, made of 2-mm-thick polychlorotrifluoroethylene (PCTFE), 15 mm in diameter and 10 mm in length, with 0.02-cm aluminum entrance windows and 0.03 cm Kapton exit windows. Tiny holes in the exit windows of the cells allow LHe to enter and cool the ammonia beads contained in two of the cells. A third cell contained a 2.2-mm-thick (1.1 % r.l.) disk of amorphous carbon, and the fourth was left empty. The carbon and empty cells were used for estimating nuclear backgrounds and for systematic checks. These target cells were mounted on a vertical target stick that could be removed from the cryostat for filling the ammonia cells and moved up and down to center the desired cell on the beam line. The targets were immersed in LHe inside a vertically oriented cylindrical container called the “minicup.” The minicup and the target chamber are shown in Fig. 1. Thin windows in the cryostat allowed scattered particles to emerge in the forward and side directions.

The DNP method of proton (or deuteron) polarization uses a hydrogenated (or deuterated) compound (e.g.,

$^{15}\text{NH}_3$) in which a dilute assembly of paramagnetic centers was produced by pre-irradiation with a low-energy electron beam. During the experiment the target material was exposed constantly to microwave radiation of approximately 140 GHz to drive the hyperfine transition that polarizes the proton spins. The microwave radiation was supplied by an extended interaction oscillator (EIO) that generated about 1 W of microwave power with a bandwidth of about 10 MHz. The microwaves were transmitted to whichever target cell was in the electron beam through a system of waveguides connected to a gold-plated rectangular “horn” (visible in Fig. 1). The microwave frequency could be adjusted over a bandwidth of 2 GHz to match the precise frequency required by the DNP. The negative and positive nuclear spin states were separated by ~ 400 MHz, so that either polarization state could be achieved by selecting the appropriate microwave frequency. Throughout the experiment, the sign of the nuclear polarization was periodically reversed to minimize the effects of false spin asymmetries.

During the experiment, the target polarization was monitored with an NMR system, which includes a coil wrapped around the outside of the target cell in a resonant RLC (tank) circuit. The circuit was driven by an RF generator tuned to the proton Larmor frequency (212.6 MHz). Depending on the sign of the target polarization, the coil either absorbed or emitted energy with a corresponding gain or loss in the resonant circuit. The induced voltage in the RLC circuit was measured and translated into the corresponding polarization of the sample.

To avoid depolarization from local heating, the beam was rastered over the face of the target in a spiral pattern, using two pairs of perpendicular electromagnets upstream from the target. Radiation damage to the target material from the electron beam was repaired by a periodic annealing process in which the target material was heated to 80–90 K. Annealing was done approximately once a week. After several annealing cycles, the maximum polarization tended to decrease, requiring the loading of fresh target material several times during the experiment. NH_3 material was replaced when the polarization reached a level of approximately 10% less than previous anneals. Target material was typically replaced after receiving a cumulative level of charge equivalent to that delivered by 2–3 weeks of 5 nA beam time.

The polarized target was operated for seven months during the EG1b experiment. The typical proton polarization maintained during the run was ~ 70 –75%, with a maximum value of 96% without beam on target, and always remaining above 50% during production running (more details on the target and its operation can be found in Ref. [86]).

D. The CLAS spectrometer

The CEBAF Large Acceptance Spectrometer (CLAS), described in detail in Ref. [11], was based on a six-coil toroidal superconducting magnet. Figure 2 shows a cutaway view of the detector along the beam line. Charged particles are tracked through each of the six magnetic field regions

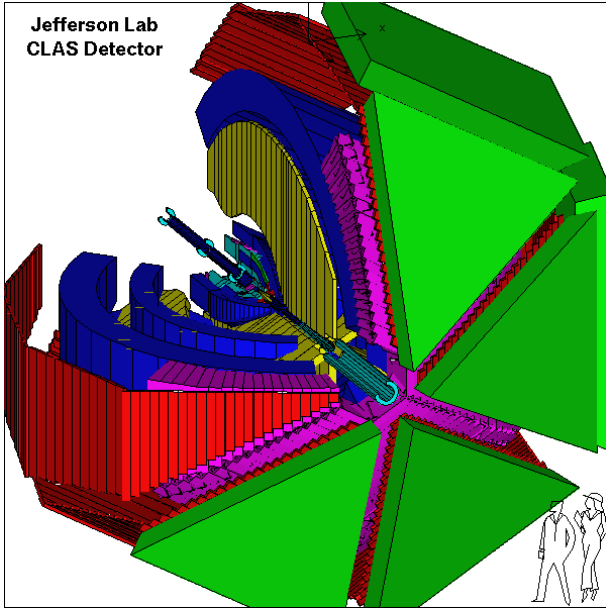


FIG. 2. (Color online) The CLAS spectrometer. Different colors represent different components of the detector (from the central target outward): three layers of drift chambers (DCs) (blue) and the torus magnet (yellow), Cerenkov counters (CCs) (magenta), TOF counters (SCs) (red) and electromagnetic calorimeters (ECs) (green). The electron beam travels through the central axis from upper left to lower right.

(hereby labeled “sectors”) between its coils, with three layers of multi-wire drift chambers (DC), numbered 1 to 3 consecutively from the target outward. [90].

Beyond the magnetic field region, charged particles were detected in a combination of gas Cerenkov counters, scintillation counters, and total absorption electromagnetic calorimeters. There was one set of scintillation counters (SC) [91] for each of the six sectors. These were used for triggering and for time-of-flight (TOF) measurements, with a typical time resolution of 0.2–0.3 ns. In the forward region of the detector, the SC was preceded by gas-filled Cerenkov counters (CC) [92] designed to distinguish electrons and pions. Finally, each sector included a total absorption sampling electromagnetic calorimeter (EC) [93] made of alternating layers of lead and plastic scintillator with a combined thickness of 15 r.l. The EC was used to measure the energy of the scattered electrons and to detect neutral particles.

Torus currents of 1500 A (at low beam energies) or 2250 A (at high beam energies) were employed in this experiment. For positive (negative) current, forward-going negative particles were bent inward (outward) with respect to the beam line. The two conditions were referred to as “inbending” and “outbending,” respectively. Inbending allowed for larger acceptance of electrons at large scattering angles (high θ) and higher luminosity, whereas outbending allowed for larger acceptance at small scattering angles (low θ). The reversibility of the magnet current also allowed systematic studies of charge-symmetric backgrounds.

E. Trigger and data acquisition

All analog signals from CLAS were digitized by FASTBUS and VME modules in 24 crates. The data acquisition could be triggered by a variety of combinations of detector signals. Our event trigger required signals exceeding minimum thresholds in both the EC and CC [94]. All photomultiplier-tube (PMT) time-to-digital-converter (TDC) and analog-to-digital-converter (ADC) signals (i.e., SC, EC, and CC signals) generated within 90 ns of the trigger were recorded, along with drift-chamber TDC signals [11]. The trigger supervisor (TS) generated busy gates and necessary resets, and directed all the signals to the data acquisition system (DAC). The DAC accepted event rates of 2 kHz and data rates of 25 MB/s [11].

The simple event builder (SEB), used for offline reconstruction of an event, used geometric parameters and calibration constants to convert the TDC and ADC data into kinematic and particle identification data. The SEB cycled through particles in the event to search for a single trigger electron—a negatively charged particle that produced a shower in the EC. If more than one candidate was found, the one with the highest momentum was selected. This particle was traced along its geometric path back to its intersection in the target to determine the path length, which, with the assumption that its velocity $v = c$, determined the event start time. From this start time, the TOF of other particles could then be determined from the SC TDC values. The TDC values from the EC were used when SC values were not available for a given particle.

IV. DATA ANALYSIS

A. Data and calibrations

The EG1b data were collected over a 7-month period from 2000 to 2001. More than 1.5×10^9 triggers from the NH_3 target were collected in 11 specific combinations (1.606+, 1.606−, 1.723−, 2.286+, 2.561−, 4.238+, 4.238−, 5.616+, 5.723+, 5.723−, and 5.743−) of beam energy (in GeV) and main torus polarity (+, −), hereby referred to as “sets.” Sets with similar beam energies comprise four groups with nominal average energies of 1.6, 2.5, 4.2 and 5.7 GeV. The kinematic coverage for each of these four energy groups is shown in Fig. 3.

Calibration of all detectors was completed offline according to standard CLAS procedures. These procedures use a subset of “sample” runs for each beam energy and torus polarity to determine calibration constants for all ADC and TDC channels. During analysis, these data were checked using these constants, and additional calibrations were performed whenever necessary.

The calibration of the TOF system (needed for accurate time-based tracking) resulted in an overall timing resolution of < 0.5 ns [91]. Minimization of the distance-of-closest-approach (DOCA) residuals in the DC led to typical values of 500 μm for the largest cell sizes (in region 3) [90]. The EC

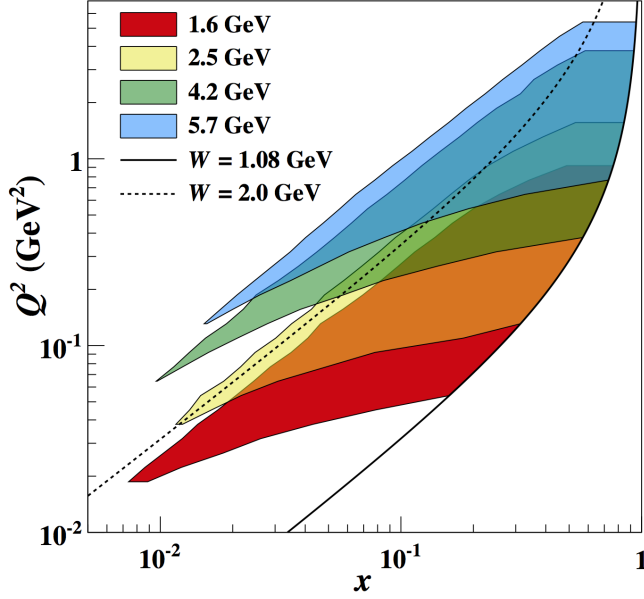


FIG. 3. (Color online) Kinematic coverage in Q^2 vs x for each of the 4 electron beam-energy groups in the EG1b experiment. The solid and dotted lines denote the $W = 1.08$ and 2.00 GeV thresholds, respectively.

provided a secondary timing measurement for forward-going particles, and played a role for the trigger and for particle identification [93]. The mean timing difference between the TOF and calorimeter signals was minimized, yielding an overall EC timing resolution of <0.5 ns.

After calibration, all raw data were converted into particle track information and stored (along with other essential run and event data) on data-summary tapes (DSTs).

B. Quality assessment

Quality checks were done to minimize potential bias introduced by malfunctioning detector components, changes in the target, and false asymmetries. DST data that did not meet the minimal requirements outlined in this section were eliminated from the analysis.

The electron count rate in each sector (normalized by the Faraday cup charge) was monitored throughout every run. DST files with count rates outside a prescribed range ($\pm 5\%$ and $\pm 8\%$ for beam energies <3 GeV and >3 GeV, respectively) were removed from the analysis in order to eliminate temporary problems, such as drift chamber trips, encountered during the experiment.

In order to minimize false asymmetries, the beam charge asymmetry $(Q_{\uparrow} - Q_{\downarrow})/(Q_{\uparrow} + Q_{\downarrow})$ for ungated cumulative charges $Q_{\uparrow}(Q_{\downarrow})$ for positive (negative) helicities was monitored. A cut of ± 0.005 on this asymmetry ensured that the false physics asymmetry due to this effect was much smaller than 10^{-4} .

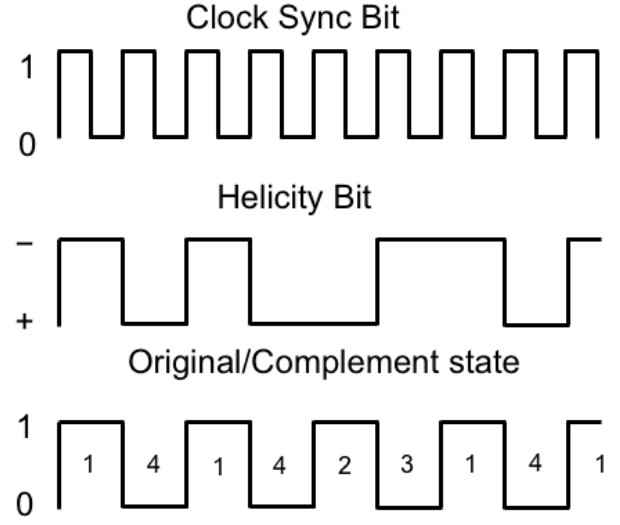


FIG. 4. Helicity signal logic. The clock signal (top) provided a rising edge every 30 ns. The helicity bit train (middle) was a pseudo-random stream of opposite bit pairs. The logic analyzed each helicity bit into four categories (bottom): 1, negative first bit followed by its complement; 4, positive second bit preceded by its complement; 2, positive first bit followed by its complement; and 3, negative second bit preceded by its complement. Buckets without a complementary partner were removed from the analysis.

Electron helicities were picked pseudorandomly at 30 Hz, always in opposite helicity pairs to minimize non-physical asymmetries. A synchronization clock bit with double the frequency identified missing bits due to detector dead-time or other uncertainties, allowing ordering of the pairs (see Fig. 4). All unpaired helicity states were removed from the analysis.

Plots of beam raster patterns were used to monitor target density and beam quality (see Fig. 5). Data obtained when raster patterns exhibited elevated count rates in regions where the beam was grazing the target cup were also excluded entirely from analysis.⁴

C. Event selection

As a starting point for the selection of events, particles with momentum $p \geq 0.20E_{beam}$ that fired both the CC and EC triggers were treated as electron candidates. Additional criteria, discussed below, were then applied to minimize background from other particles, primarily π^- .

⁴ In one unique case where empty-target runs meeting our selection criteria runs were not available, only data corresponding to anomalous raster regions were removed. A systematic normalization uncertainty of 2% on event counts from these runs, obtained from comparison to unaffected runs, is incorporated into our analysis.

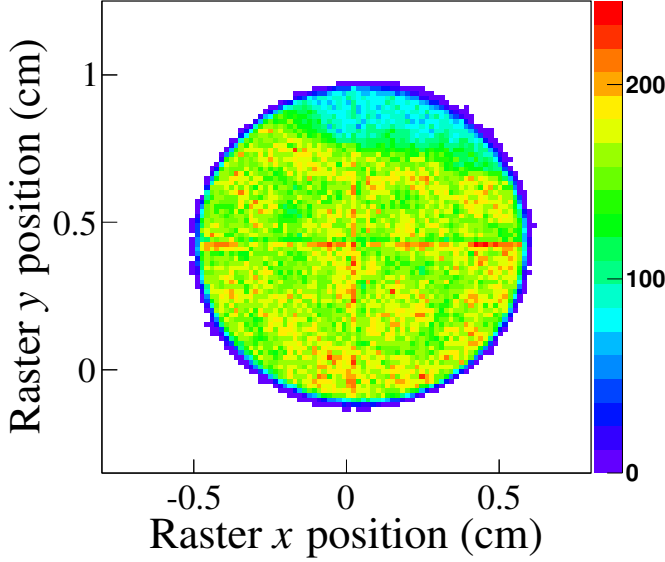


FIG. 5. (Color online) Raster pattern for a sample run, demonstrating some temporary settling of the target material. (The “crosshair” pattern is a non-physical relic of the coordinate reconstruction.)

1. Cherenkov counter cuts

The CCs use perfluorobutane (C_4F_{10}) gas, and have a threshold of ~ 9 MeV/ c for electrons and ~ 2.8 GeV/ c for pions. Between these two momenta, the CC efficiently separated pions from electrons. A minimum of 2.0 detected photoelectrons (p.e.) in the CC PMTs was required for electron candidates with $p < 3.0$ GeV/ c . For particles with higher momentum, a minimum cut of 0.5 p.e. was used only to eliminate contributions from internal PMT noise.

Geometric and time matching requirements between CC signals and measured tracks were used to reduce background. These cuts on the correlation of the CC signal with the triggering particle track removed the majority of the contamination dominating the lower part of the CC signal spectrum. The effect of these cuts is shown in Fig. 6. Pion contamination at low signal heights was reduced substantially with little loss of good events.

The determination of dilution factors (see Sec. IVE1) required a precise comparison of count rates for different targets. Therefore, detector acceptance and efficiency for runs on different targets had to remain constant. Inefficiencies in the CC were the main source of uncertainty in electron detection efficiency for CLAS. Therefore, tight fiducial cuts were developed to select the region where the CC was highly efficient. These cuts were used only for the dilution factor analysis.

The CC efficiency is defined by the integral of an assumed Poisson distribution yielding the percentage of electron tracks generating signals above the 2.0 p.e. threshold. It varied as a function of kinematics due to the CC mirror

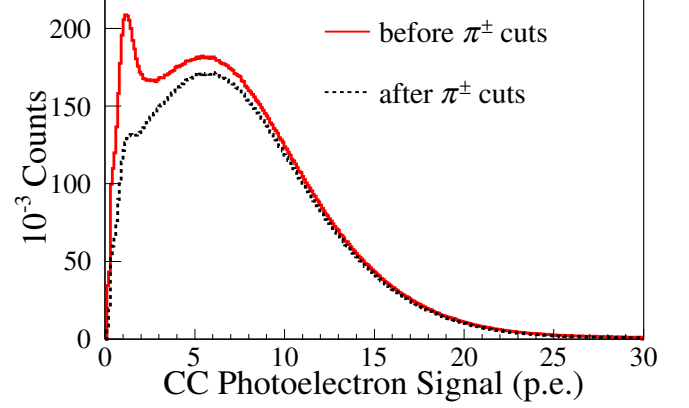


FIG. 6. (Color online) Cherenkov signal distributions before (red, solid line) and after (black, dotted line) requiring track matching.

geometry. The mean value of the signal distribution was determined as a function of electron momentum p and angles θ and ϕ using ep elastic events from several CLAS runs at beam energies of 1.5–1.6 GeV. The deduced efficiency map has a plateau of high efficiency in the center of each sector, which rapidly drops off to zero at the sector edges. For the fiducial cut, we developed a function of p , θ , and ϕ to define a boundary enclosing events with more than 80% CC efficiency in each 0.5 GeV momentum interval (see Fig. 7). Fiducial cuts were specific to each CLAS torus setting. Additional center-strip cuts in each sector were required to remove regions with inefficient detector elements.

2. Electromagnetic calorimeter cuts

Further suppression of pion backgrounds was provided by the EC, in which minimum ionizing particles (hadrons) deposited far less energy than showering electrons. A base cut was developed by observing the energy EC_{tot} deposited in the entire EC and the energy EC_{in} deposited only in the first 5 of 13 layers (see Fig. 8). A loose cut of $EC_{in} < 0.22$ GeV (including the sampling fraction [93]) was used as a first step in separating pions from electrons in the calorimeter.

The EC cuts were further refined by taking into account the relationship between the momentum of the particle and the energy deposited in the calorimeter. Since electrons deposited practically all of their energy in the calorimeter, a lower bound on EC_{tot}/p further reduced contributions from pions. For $p > 3$ GeV, where the CC spectrum fails to differentiate pions and electrons, a strict cut of $EC_{tot}/p > 0.89$ was applied, while a looser cut of $EC_{tot}/p > 0.74$ is used at $p < 3$ GeV. Figure 9 shows these cuts for events plotted in EC_{tot}/p versus the CC photoelectron signal.

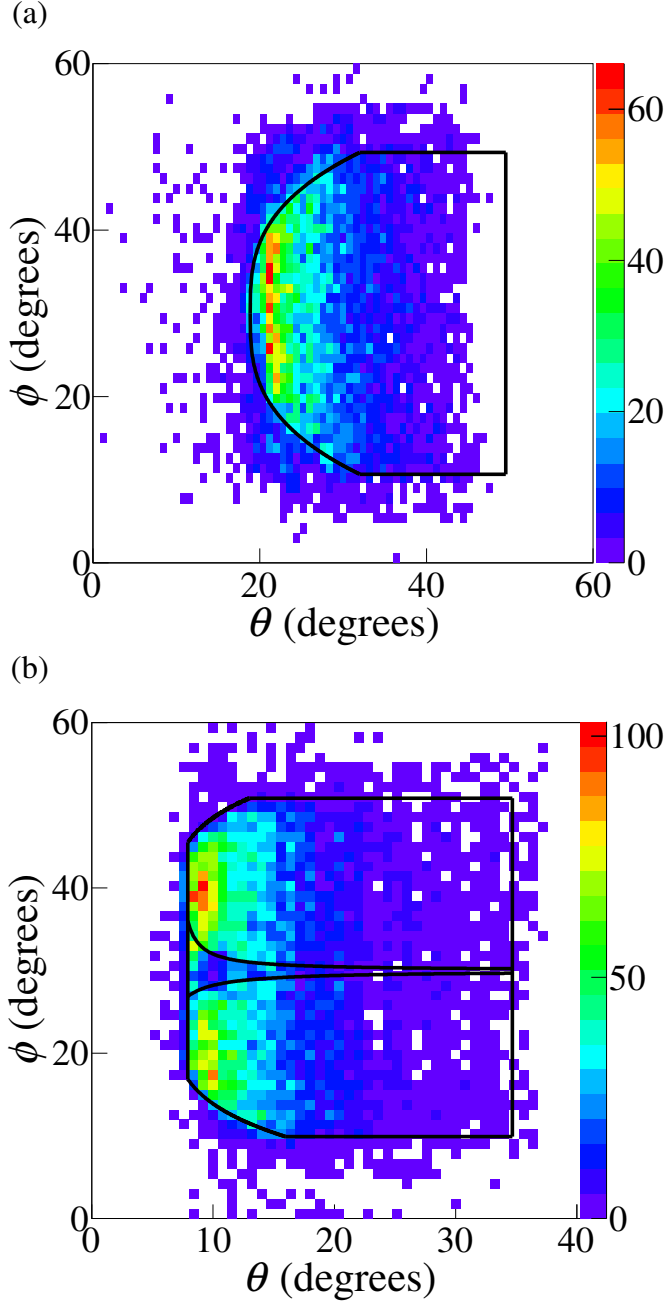


FIG. 7. (Color online) Sample fiducial cuts for (a) inbending and (b) outbending electrons, shown in ϕ vs θ for one CLAS sector.

3. Remaining π^- contamination

The remaining pion contamination was determined as a function of θ (5° bins) and p (0.3 GeV bins) as follows in each p , θ bin: A modified, extrapolated Poisson distribution fit to our CC p.e. spectrum was subtracted from the pion “peak” seen at low p.e. values (see Fig. 6) to get a low p.e. contamination estimate. Then, we analyzed only runs without the CC trigger in use, inverting all the electron se-

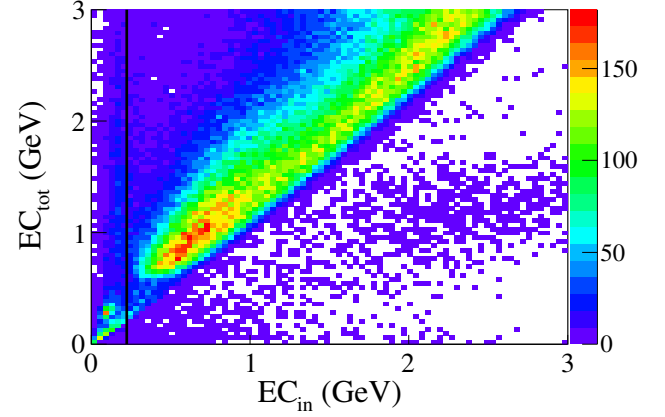


FIG. 8. (Color online) The total energy EC_{tot} deposited in the EC vs the energy EC_{in} deposited in the inner (front) layer of the EC only for electron candidates. The plot shows a clear separation of electrons from light hadrons (bottom left corner). A cut on EC_{in} (shown by the vertical line) removes most of the hadron background.

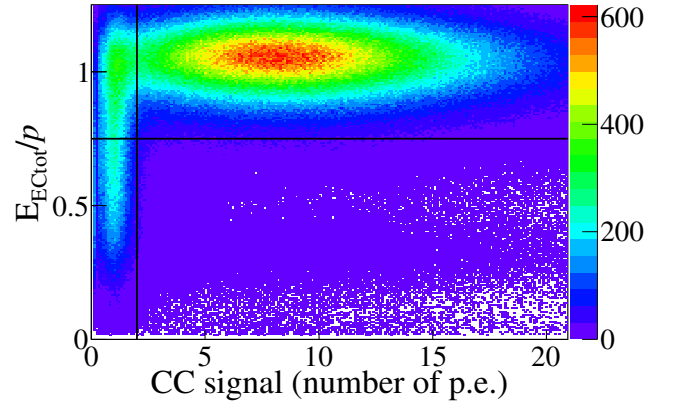


FIG. 9. (Color online) Scatter plot of EC_{tot}/p vs CC signal, at $p < 3$ GeV/c, after fiducial cuts. Only events to the right and above the straight lines are kept as inclusive electrons.

lection cuts on the EC, resulting in a test sample composed nominally of pions. This sample was then normalized to the low p.e. contamination estimate at p.e. < 2.0 . The normalized nominal pion data provided an estimate of the π^- contamination present at p.e. > 2.0 , where the inclusive electrons lie. Dividing by the total number of inclusive electrons yielded the contamination fraction $R^p(\theta, p)$.

Plots of the pion contamination fractions as a function of p and θ are shown in Fig. 10. These were seldom more than 1% of the total electron count. An exponential function

$$R(\theta, p) = e^{a+b\theta+cp+d\theta p} \quad (44)$$

was then fit to these points. Pion contamination corrections

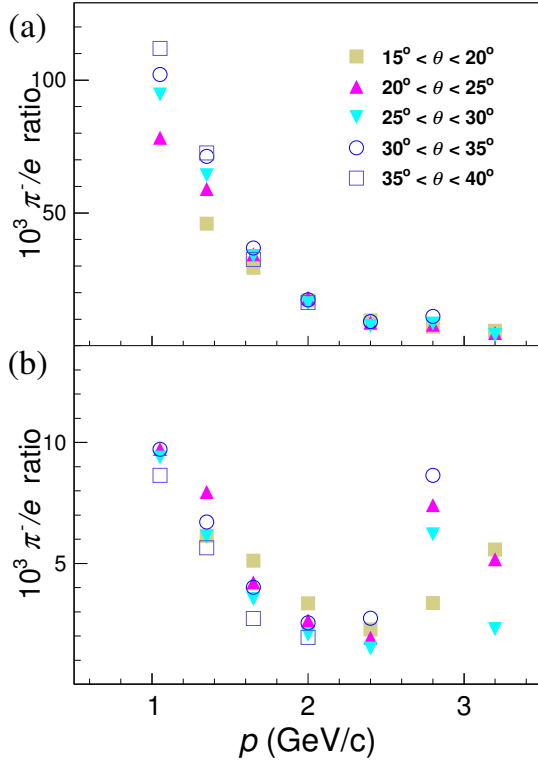


FIG. 10. (Color online) Pion contamination fraction (a) before and (b) after track-matching cuts for the 5.7 GeV beam energies, as a function of polar angle and momentum. The increase beyond $p = 2.8$ GeV/c indicates the threshold beyond which pions start to produce a signal in the CC.

could be made by adding

$$\Delta A_{raw} = \frac{R(\theta, p)(A_{raw} - A_\pi)}{1 - R(\theta, p)} \quad (45)$$

to the raw asymmetry A_{raw} . Since the effect is very small, and the inclusive pion asymmetry A_π is not well known, we applied no correction and instead treat ΔA_{raw} with $A_\pi = 0$ as the systematic uncertainty.

4. Background subtraction of pair-symmetric electrons

Dalitz decay of neutral pions [95] and Bethe-Heitler processes [96] can produce e^+e^- pairs at or near the vertex, contaminating the inclusive e^- spectrum. To determine this contamination, we assumed that the event reconstruction and detector acceptances for e^+ production were identical to those for their paired e^- when the main torus current was reversed, and that the overall cross-section is small enough that small differences in beam energy (e.g. 2.286 versus 2.561 GeV) minimally affected the production rate.

Each data set was correlated with another having a similar beam energy but opposite torus polarity. Events with

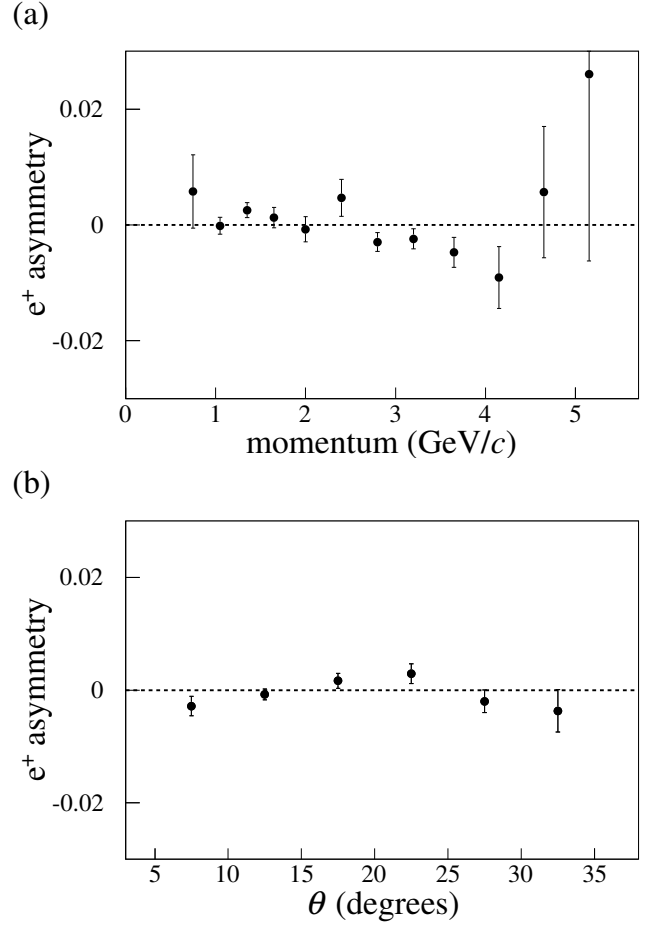


FIG. 11. Average positron asymmetries for the 5.7 GeV data set as a function of (a) momentum and (b) scattering angle θ .

leading positron triggers were analyzed identically to those with electron triggers. The overall double-spin asymmetry for e^+ triggers was small (see Fig. 11). The e^+/e^- contamination ratios R^p , which were largest at low momenta (Fig. 12), were fit with the parametrization of Eq. (44). Then, Eq. (45) (with $A_\pi \rightarrow A_{e^+}$) was used to determine a multiplicative background correction factor $C_{back} \equiv (A_{raw} + \Delta A_{raw})/A_{raw}$ to convert the raw asymmetry to the background-free physics asymmetry. Here we assumed that $A_{e^+} = 0$, consistent with the average from our measurements (see Fig. 11).

To estimate the systematic uncertainty from this background, two changes were made to C_{back} in the reanalysis. R^p was changed by half the difference between two equivalent determinations: one using outbending electrons and inbending positrons, and the other using the opposite torus polarities for either particle. Also, A_{e^+} was set to a nonzero value equal to 3 times the statistical uncertainty of the averaged positron asymmetry.

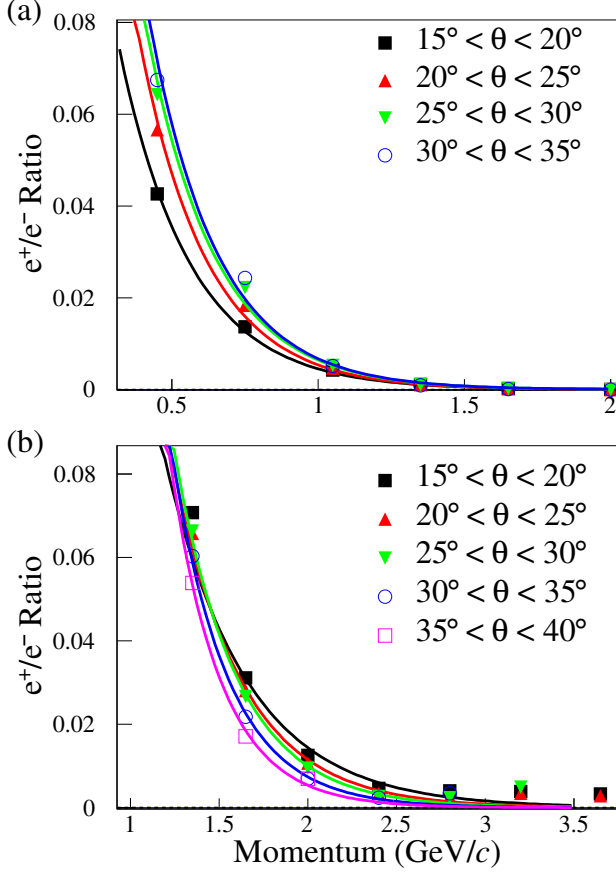


FIG. 12. (Color online) Ratios of e^+/e^- as a function of electron momentum p , at various θ angles, for the (a) 2.561– and (b) 5.727+ data sets.

5. Elastic $ep \rightarrow e'p$ event selection

Both the momentum corrections (Sec. IV D 2) and the determination of beam polarization \times target polarization (Sec. IV E 2) required identified elastic ep scattering events. For this purpose, we selected two-particle events containing an electron and one track of a positively charged particle. Electron PID cuts were relaxed to require only a minimum of 0.5 CC p.e. The E/p EC cut thresholds were lowered to 0.56 for $p < 3$ GeV/ c and 0.74 for $p > 3$ GeV/ c . These relaxed cuts increased the statistics while the exclusivity cuts discussed below removed all pion background.

A beam-energy-dependent cut on $|M_p - W|$ (where M_p is the proton mass), which ranged from 30 MeV at 1.6 GeV to 50 MeV at 5.7 GeV, suppressed inelastic contributions. Further kinematic constraints were applied on deviations of the missing momentum p , the proton polar angle θ , and the difference between the azimuthal proton and electron angles $\Delta\phi$, from those expected for elastic ep kinematics (see Fig. 13). Final cuts of $\Delta p < 0.15$ GeV, $\Delta\theta < 1.5^\circ$ and $\Delta\phi < 2.0^\circ$ identify elastic ep events, with typically less than 5% nuclear background (see Fig. 22).

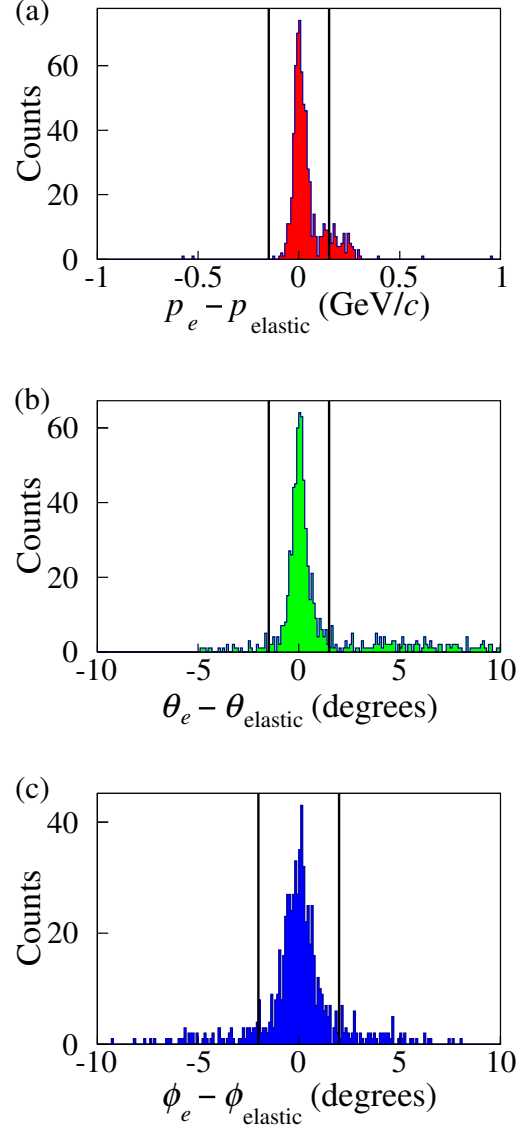


FIG. 13. (Color online) Kinematic cuts on (a) the difference between measured and expected momentum, (b) polar angle, and (c) azimuthal angle of elastic ep events. Each of the distributions has the other two cuts applied.

D. Event corrections

The reconstructed track parameters of each event were corrected for various distortions to extract the correct kinematic variables at the vertex. These kinematic corrections are explained in the following two subsections.

1. Phenomenological kinematics corrections

Kinematic corrections were implemented to account for the effects of energy loss from ionization, multiple scattering, and geometrical corrections to the reconstruction algo-

rithm (for target rastering and stray magnetic fields).

Rastering varies the xy position of the beam over the target in a spiral pattern with a radius of ~ 0.5 cm (see Fig. 5). The instantaneous beam position can be reliably extracted from the raster magnet current. The reconstructed z -vertex position (the z axis is along the beam line) and the “kick” in ϕ were corrected for this measured displacement of the interaction point from the nominal beam center [97], prior to the application of a nominal ($-58 < v_z < -52$ cm) vertex cut (see Fig. 14).

Collisional energy loss of both incident and scattered electrons within the target was accounted for by assuming a 2.8 MeV/(g/cm²) energy loss rate dE/dx for electrons [98]. The calculation, incorporating the target mass thickness, vertex position, and polar scattering angle θ , yielded typical energy losses of ~ 2 MeV before and after the event vertex. The energy loss of scattered hadrons was similarly estimated using the Bethe-Bloch formula [99].

Determination of the effects of multiple scattering on kinematic reconstruction was more complex, and was studied with the GEANT CLAS simulation package GSIM [100]. For multi-particle events, an average vertex position was determined by calculating a weighted average of individual reconstructed particle vertices. Comparing each particle vertex with this average gives a best estimate for the effect of multiple scattering on that particle on its way to the first drift chamber region. The GSIM model was then used to generate an adjustment $d\theta(\theta, 1/p)$ [101] to the measured scattering angle.

The GSIM package was also used to provide a leading-order correction due to magnetic field effects not incorporated into the main event reconstruction software. Particularly important is the extension of the target solenoid field into the inner layer DC. This study resulted in corrections applied to the polar angle $d\theta(\theta, 1/p)$ and the azimuthal angle $d\phi(\theta, 1/p)$ [101].

2. Empirical momentum corrections

Imperfect knowledge of the field map of the CLAS magnet, misalignment of the drift chamber wires or the drift chambers themselves relative to their nominal positions, effects of wire sag, and other possible distortions in the drift chamber wire positions used in the tracking code lead to deviations in the reconstructed kinematics of the scattered particles. An empirical method was developed [102] to correct the measured momenta of the particles, using parameters that were determined by exploiting the four-momentum (p_μ) conservation for both elastic ep and two-pion production $ep \rightarrow ep\pi^+\pi^-$ events.

The overall correction function depends on the momentum \vec{p} , the polar angle θ and the azimuthal angle ϕ . It includes 16 parameters for each sector, totaling 96 parameters, and 7 additional parameters to improve the fit in the case of negative torus magnet polarities. Corrections in the momentum and polar angle were calculated relative to the region 1 drift chamber. The azimuthal angle, having a larger

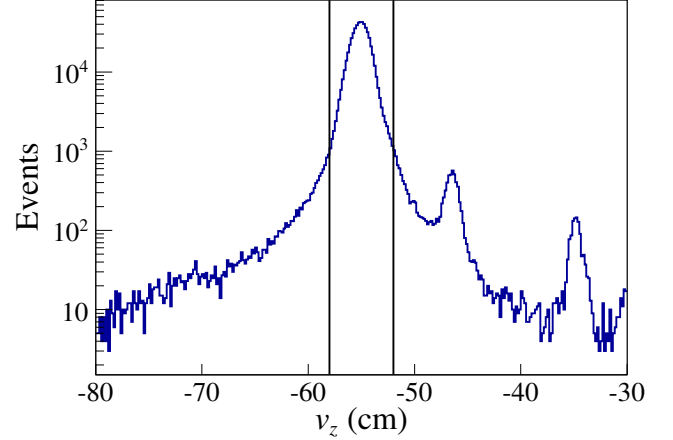


FIG. 14. (Color online) Vertex z positions for electrons after corrections for the raster. Secondary peaks correspond to target windows. A vertex cut of ($-58 < v_z < -52$ cm) was applied as shown to select events from the target.

intrinsic uncertainty, was kept fixed since it was shown to be correct within this uncertainty for elastic events.

The parameters were optimized by minimization of

$$\chi^2 = \sum_i \sum_\mu \frac{\Delta p_\mu^2}{\sigma_{p_\mu}^2} + \sum_e \frac{(W_c - M_p)^2}{(0.020 \text{ GeV})^2}, \quad (46)$$

over i total events and e elastic events. Here, p_μ are the components of the missing four-momentum and σ_{p_μ} are the expected resolutions of each component, $\sigma_{p_x} = \sigma_{p_y} = 0.014$ GeV and $\sigma_{p_z} = \sigma_E = 0.020$ GeV, M_p is proton mass, and W_c is the missing mass of the inclusive elastic event.

After looping over all events, an additional term $\sum_{par} par^2 / \sigma_{par}^2$, with estimated intrinsic uncertainties σ_{par} for each parameter par , was added to the total χ^2 for each parameter. This limited parameters to reasonable ranges, avoiding “runaway” solutions anywhere in the parameter space.

In order to avoid preferential weighting due to detector acceptances, elastic ep events were divided into 1° θ bins and given a relative weighting proportional to their distribution in θ . Inclusion of $ep\pi^+\pi^-$ events ensured that the corrections maintained validity over the full space of θ and p . MINUIT-based minimization of χ^2 [103] was iterated until stable values were reached, and the width of the missing momenta and energy distributions was reduced as shown in Fig. 15.

The relative absence of exclusive scattering events at $\theta \lesssim 12^\circ$ necessitated an additional forward scattering correction using inclusive elastic scattering data. Therefore, an additional adjustment $\Delta p(\theta, \phi)$ containing three more fit parameters was applied in a similar manner, except that only the difference $W - M_p$ was minimized, leading to even better resolution in the elastic peak.

Application of the kinematic corrections resulted in final ep accuracy of ~ 1.0 MeV/ c for spatial momentum cor-

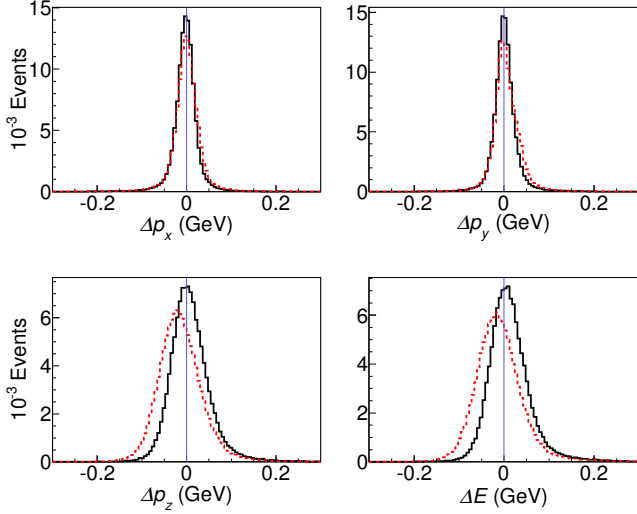


FIG. 15. (Color online) Missing energy and momentum distributions from elastic events in the 4.238 GeV inbending data set before (dashed red line) and after (black solid line) momentum corrections.

ordinates, with distribution widths $\sigma_{p_x} \approx \sigma_{p_y} \approx 17 \text{ MeV}/c$ and $\sigma_{p_z} \approx 30 \text{ MeV}/c$. Overall momentum and angle corrections were generally a few tenths of a percent in electron momentum p and less than one milliradian in polar angle θ . The overall effect of all kinematic corrections can be seen in Figs. 16, 17, and 18. Systematic uncertainties due to the kinematic inaccuracies of p_z , $\sqrt{p_x^2 + p_y^2}$, and E_{beam} were determined by using the smoothly parameterized models of the asymmetries and structure functions as a proxy for the actual data, shifting each bin center by an amount equal to its uncertainty, and subtracting the difference. “Bin smearing” uncertainties due to the distribution widths were estimated by determining the uncertainty in W corresponding to the momentum uncertainty, smearing each bin in the modeled $A_{||}$ by a corresponding Gaussian distribution, and subtracting the difference from the unsmeared model.

3. Charge normalization correction

The calculation of the dilution factor (nominally $\frac{3}{18}$) required a comparison of the normalized counts from the ammonia, carbon, and empty (LHe) targets. Multiple scattering in the target, as well as changes in beam focusing, could affect the measurement of beam charge determined by the Faraday cup, which was 29 m downstream from the target. The contribution of multiple scattering in the target on beam divergence can be estimated with a Moliere distribution [98]. At the lowest energies the size of the beam at the FC exceeded its 5.0 cm aperture.

The (ungated) upstream BPMs were used to establish a relative correction to the FC signal for different targets. The BPM to FC ratio at 5.7 GeV (with multiple scattering

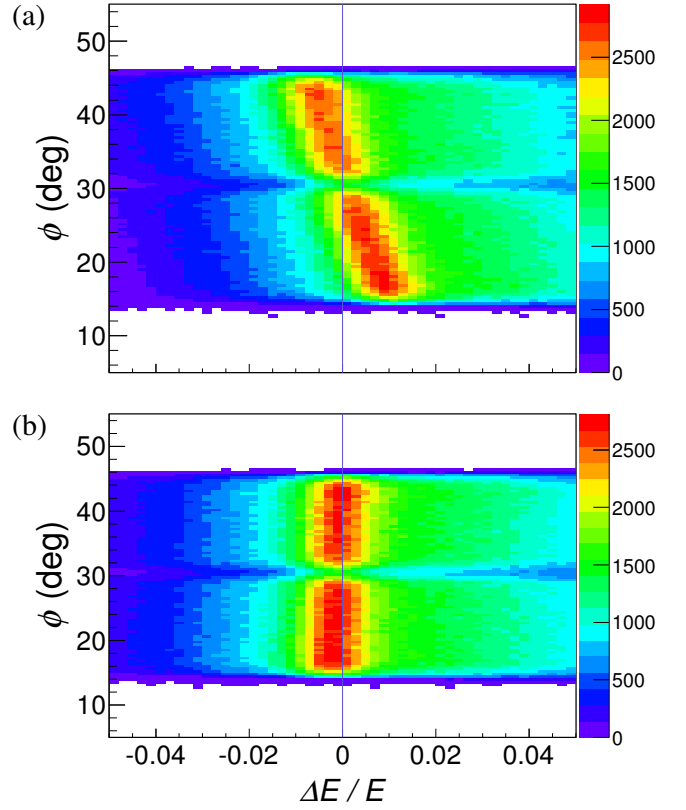


FIG. 16. (Color online) Measured energy mismatch $\Delta E'/E'$ versus ϕ for elastically scattered electrons (a) before and (b) after the kinematic corrections for the 1.723– data set. After corrections, $\Delta E'/E'$ is centered on zero for all azimuthal angles.

suppressed) provided the overall normalization. For beam energies $E < 3 \text{ GeV}$, this ratio provided a correction factor with an approximate accuracy of 0.001.

The difference in the FC correction factors for the ammonia target and the empty target was especially large because of the significant difference in their radiation lengths. The relative factor was ~ 1.14 at 1.6 GeV and ~ 1.05 at 2.4 GeV. These corrections were needed for dilution factor extractions from data (see below) but played no role in the extracted physics asymmetries.

E. Asymmetries and corrections

The raw asymmetry

$$A_{raw} = \frac{n^+ - n^-}{n^+ + n^-} \quad (47)$$

was determined, where $n^+(n^-)$ is the live-time gated, FC-normalized, inclusive electron count rate for (anti)-aligned beam and target polarizations. Except for a few small corrections, $A_{||}$ is derived from A_{raw} by dividing out the di-

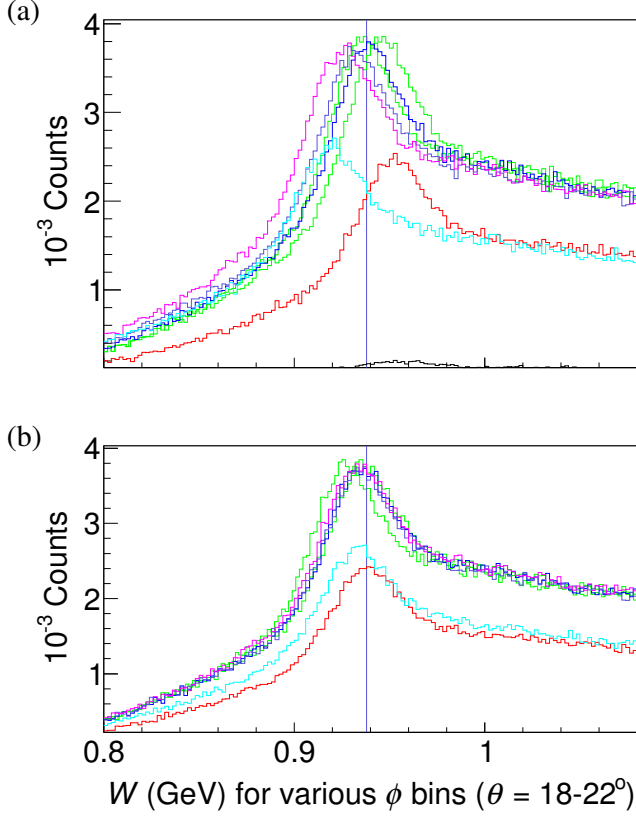


FIG. 17. (Color online) Elastic W peaks (different colors/shades) for seven ϕ bins spanning the detector acceptance, (a) before and (b) after kinematic corrections to the 2.286-GeV data set. The plots represent one sector and one polar-angle bin. The spurious ϕ dependence of the elastic W peak location is removed by these corrections.

lution factor F_{DF} (which accounts for unpolarized backgrounds), the electron beam polarization P_b , and the proton target polarization P_t , such that

$$A_{||} \approx \frac{1}{F_{DF} P_b P_t} \frac{n^+ - n^-}{n^+ + n^-}. \quad (48)$$

Smaller contributions due to radiative corrections and other possible backgrounds were also taken into account. The modeled radiative contribution to the polarized and unpolarized cross-sections was characterized by an additive term A_{RC} and a “radiative dilution factor” f_{RC} . Contributions due to misidentified inclusive electrons (C_{back}) and polarized ^{15}N (P_{15N}^*) were also taken into account, yielding

$$A_{||} = \frac{C_{back}}{F_{DF} P_b (P_t + P_{15N}^*) f_{RC}} A_{raw} + A_{RC} \quad (49)$$

as the final experimental measurement. C_{back} has already been described; the remaining terms will be discussed in sequence.

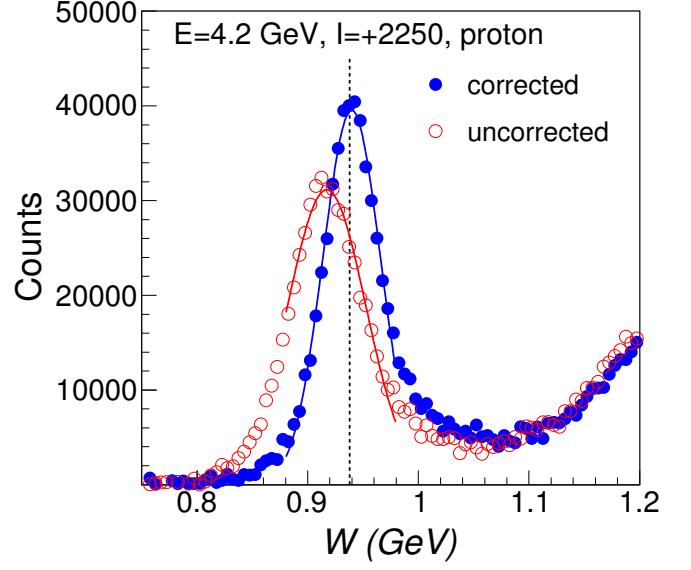


FIG. 18. (Color online) Missing mass W before (red, open circles) and after (blue, solid dots) the kinematic corrections for the 4.238+ data set. The corrections decrease the distribution width and center the mean on the 0.938 GeV proton mass, which is indicated by the vertical black dashed line.

1. Dilution factor

$F_{DF} \equiv n_p/n_A$ is defined as the ratio of scattering rates for the proton (n_p) and the whole ammonia target (n_A). It varies as a function of Q^2 and W , and was calculated directly from the radiated cross sections. In terms of densities (ρ), material thicknesses (ℓ), and cross-sections (σ),

$$n_p \propto \frac{3}{18} \rho_A \ell_A \sigma_p \quad (50)$$

$$n_A \propto \rho_A \ell_A \sigma_{Al} + \rho_K \ell_K \sigma_K + \rho_A \ell_A \left(\frac{3}{18} \sigma_p + \frac{15}{18} \sigma_N \right) + \rho_{He} (L - \ell_A) \sigma_{He} \quad (51)$$

with the subscripts A , p , Al , K , N , and He denoting ammonia ($^{15}\text{NH}_3$), proton, aluminum foil, kapton foil, nitrogen (^{15}N), and helium (^4He), respectively. The acceptance-dependent proportionality constant is identical in both of the above relations. Inclusive scattering data from the empty (LHe) and ^{12}C targets were analyzed to determine the total target cell length (L) and effective NH_3 thickness (ℓ_A). Scattering rates from the carbon (n_C) and empty (n_{MT}) targets were expressed as

$$n_C \propto \rho_A \ell_A \sigma_{Al} + \rho_K \ell_K \sigma_K + \rho_C \ell_C \sigma_C + \rho_{He} (L - \ell_C) \sigma_{He} \quad (52)$$

and

$$n_{MT} \propto \rho_A \ell_A \sigma_{Al} + \rho_K \ell_K \sigma_K + \rho_{He} L \sigma_{He} \quad (53)$$

with again the same proportionality constant assumed.

The inelastic scattering model employed Fermi-smear cross sections calculated for each nucleus [104], which included (unpolarized) radiative corrections and corrections for the nuclear EMC effect. Free proton cross sections were calculated from a fit to world data for F_1^p and F_2^p [105]. For cross sections on heavier nuclei, a Fermi convolution of the smearing of free nucleon Born cross sections was fit to inclusive scattering data, including EG1b data from ^{12}C , solid ^{15}N , and empty (LHe) targets [106]. The nuclear EMC effect was parameterized using SLAC data [107]. Radiative corrections used the treatment of Mo and Tsai [108]; external Bremsstrahlung probabilities incorporated all material thicknesses in CLAS from the target vertex through the inner layer DC. Radiated cross-sections (relative to that of ^{12}C) were calculated for each target material for radiation length fractions $0.01X_0$ and $0.02X_0$, and were linearly interpolated to correspond to the fraction $\rho\ell/X_0$ for each material in the appropriate target.

To apply the model, FC charge-normalized inclusive electron counts were first binned in Q^2 and W for all runs in each of the 11 data sets (see Fig. 19). From these sums, the ratios n_{MT}/n_C and n_A/n_C were formed. The ratio n_{MT}/n_C then determines L through solution of Eqs. (52) and (53). With L determined, the ratio n_A/n_C determines ℓ_A through solution of Eqs. (51) and (52). L and ℓ_A were statistically averaged in the inelastic region ($W > 1.10$ GeV) over all Q^2 values, with $1.75 < L < 2.05$ cm and $0.55 < \ell_A < 0.65$ cm over the 11 data sets. Upper bounds in W used in calculating the average were Q^2 -dependent. To evaluate the effect of the choice of the cutoff on the measurement of $L(\ell_A)$, the W -averaging range was increased (decreased) by approximately 33% in a reanalysis (to account for small variations in our measurement at high- W) and the resulting difference in F_{DF} was used to estimate the systematic uncertainties due to these parameters.

Dilution factors $F_{DF} \equiv n_p/n_A$ were then calculated for each data set. This model was checked against an older data-driven method [12, 15, 17] that used the three target count rates, only one (unradiated) model for the ratio of neutron/proton cross-sections, and the assumption that $\sigma_C = 3\sigma_{He}$ (see Fig. 20). Values of L and ℓ_A varied by less than 2% between the two methods. Division of A_{raw} by F_{DF} removes the contributions of the ^{15}N , LHe and target foil materials, leaving only the contribution from scattering by the polarized protons (see Fig. 21).

The densities and thicknesses of all target materials were varied within their known tolerances to determine systematic uncertainties. Only the variations of $\rho_C\ell_C$ and ρ_{He} had any significant ($>0.1\%$) effect on F_{DF} . Uncertainties due to the cross section model were estimated by comparing F_{DF} to a third-degree polynomial fit to the data-based dilution factors determined using the alternate method.

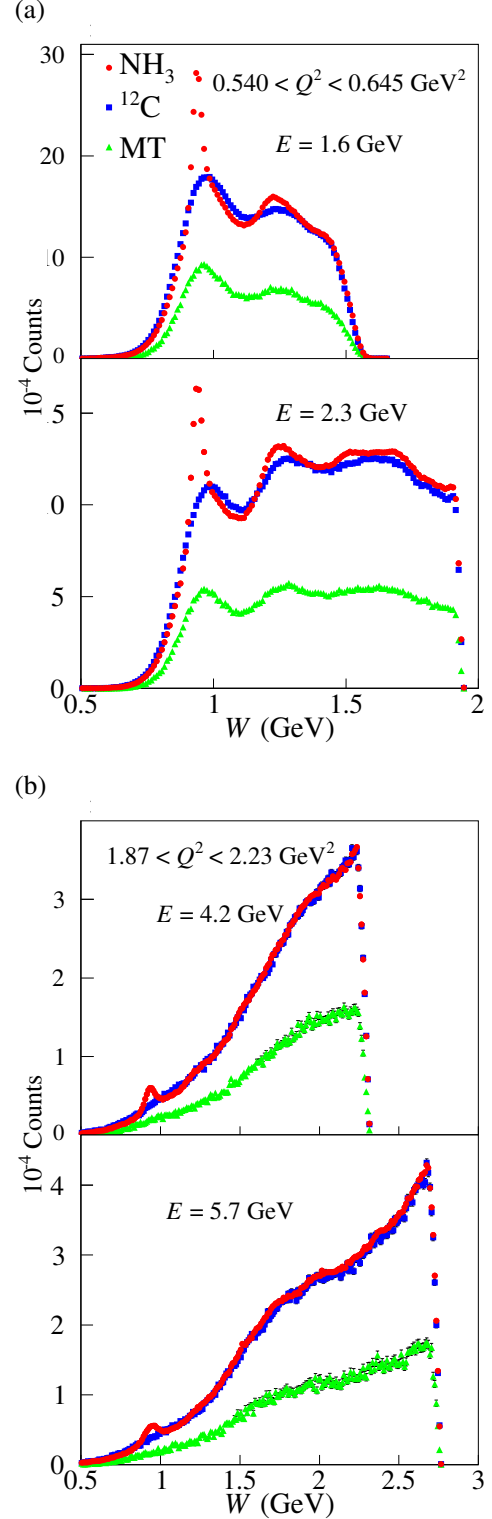


FIG. 19. (Color online) Inclusive W spectra normalized to the integrated Faraday cup charge for each target (ammonia, red circles; carbon, blue squares; and empty (MT), green triangles) in a selected Q^2 bin, at (a) the lower two beam energies and (b) the higher two beam energies.

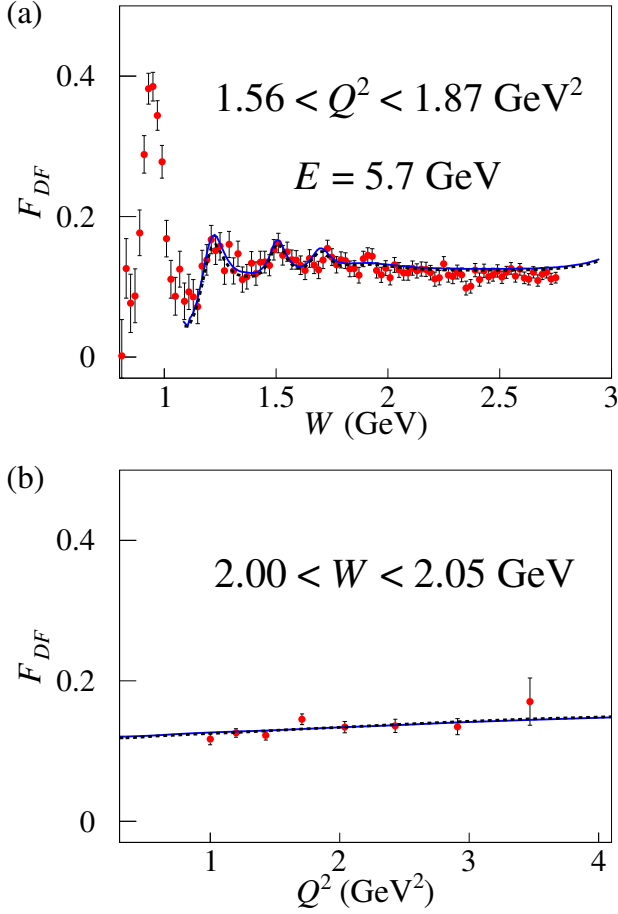


FIG. 20. (Color online) Dilution factors (a) F_{DF} vs W and (b) F_{DF} vs Q^2 , for the 5.7 GeV beam energy. The solid blue line shows the modeled dilution factor used in the analysis, and the dotted black line (most visible in plot (a) at low W) is a two-dimensional polynomial fit (in Q^2 and W) to the red points from the data-driven method. The difference between the solid blue and black dotted lines is an estimate of the model systematic uncertainty. Over much of the kinematics, F_{DF} is close to the naive ratio $3/18$ of polarized to unpolarized nucleons in the target.

2. Beam and target polarizations ($P_b P_t$)

Because NMR measurements are dominated by the material near the edge of the target cell [86] (which was not exposed to the beam and therefore had higher polarization than the bulk of the target), the polarization product $P_b P_t$ was determined experimentally using the double-spin asymmetry of elastic ep events, taking advantage of the low background levels for these exclusive events. The asymmetry $A_{||}$ for elastic scattering corresponds to the case when $A_1^p = 1$, $A_2^p = \sqrt{R^p}$, and $R^p = G_E^p / (\tau G_M^p)$, as given in Eqs. (14) and (18). The proton's electric and magnetic form factors $G_E^p(Q^2)$ and $G_M^p(Q^2)$ (see Section II F) were calculated using parametrizations of world data [109]. The polarization product $P_b P_t$ was determined by dividing

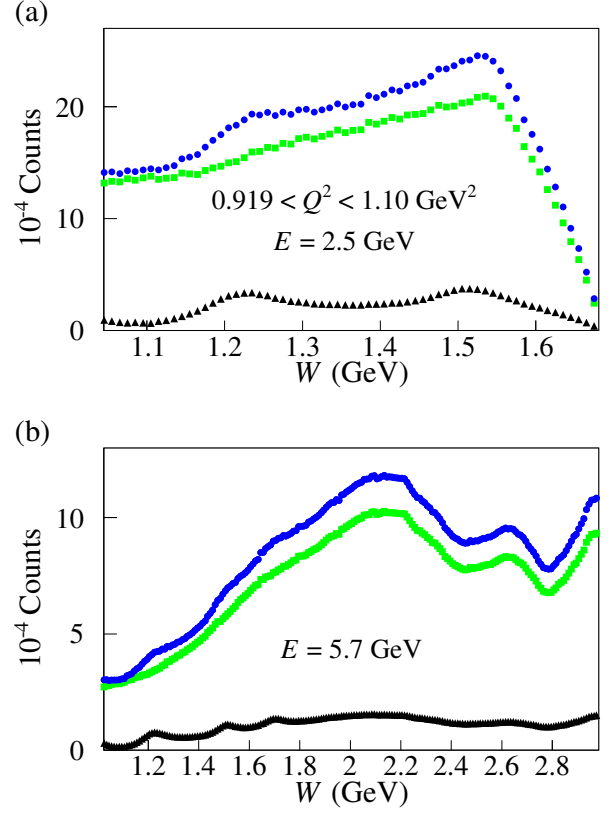


FIG. 21. (Color online) Background subtraction (using dilution factors) for inclusive inelastic W spectra for a selected Q^2 bin at (a) 2.5 GeV and (b) 5.7 GeV beam energies. The blue circles are the inclusive counts for ammonia. The green squares show the subtracted background, as determined by the dilution factors, and the black triangles are the difference, which represents the free proton counts in the ammonia target.

the measured elastic ep asymmetry by the calculated elastic $A_{||}(W = M_p, Q^2)$.

Background contamination in elastic ep events was determined by scaling the scattering spectra of the carbon target to match that of the ammonia target away from the vicinity of the free proton peak. Scattering events were selected from ^{12}C using all elastic ep cuts except the $\Delta\phi$ cut, and were normalized to the ep $\Delta\phi$ spectrum in the region $2^\circ < |\Delta\phi| < 6^\circ$ (Fig. 22). Nuclear background contributed less than 5% of the events; systematic effects due to miscalculating this background were tested by shifting the normalization region by 2° and reevaluating.

The derived $P_b P_t$ values were checked for consistency across Q^2 for each beam energy, torus current and target polarization direction. As a comparison check, a less accurate method using inclusively scattered electrons in the elastic peak was also employed to measure $P_b P_t$. This method required the subtraction of much larger backgrounds and did not incorporate radiative corrections. Within its larger uncertainty, this second method agreed with the first.

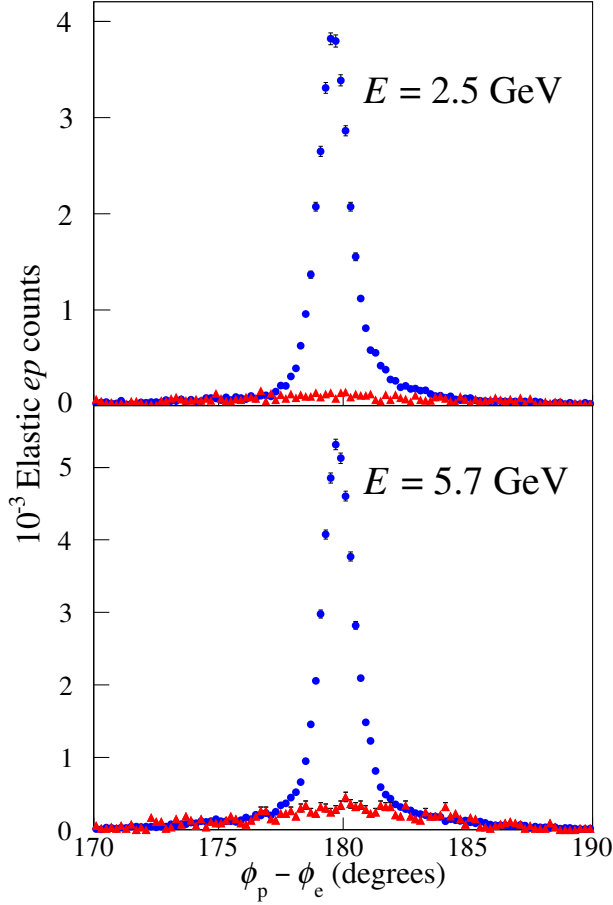


FIG. 22. (Color online) Histogram of the azimuthal angular difference $\phi_p - \phi_e$ for elastic scattering events from the NH_3 target (blue circles) overlaid with the scaled distribution from the carbon target (red triangles) for two different data sets.

The calculated elastic asymmetry is plotted against the $P_b P_t$ -normalized measured elastic asymmetry for each of the 11 data sets in Fig. 23 to demonstrate the precision of the elastic ep data. Older parametrizations of G_E and G_M [110] were substituted to evaluate the systematic uncertainty due to the $A_{||}(W = M_p, Q^2)$ model. The W cut on allowed elastic ep events was also widened by 10 MeV on each side to test for systematic effects due to ep event selection. The systematic uncertainty due to the statistical uncertainty on $P_b P_t$ was determined by adding one standard deviation to $P_b P_t$ for one of the data sets, and repeating the full analysis; this was repeated independently for each set.

3. Polarized nitrogen correction

EST (equal spin temperature) theory predicts the relative polarization ratios between two spin-interacting atoms in a

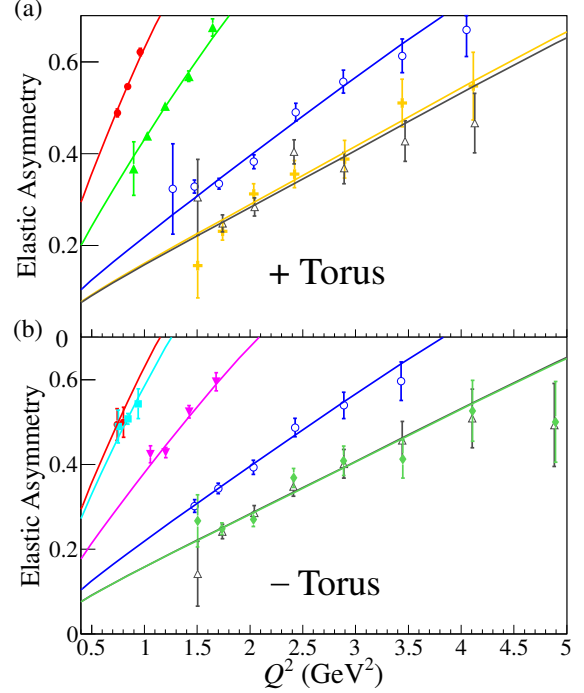


FIG. 23. (Color online) Comparison of the elastic asymmetry $A_{||}(W = M_p, Q^2)$ (solid lines) to the measured elastic asymmetries for all data sets, normalized by $P_b P_t$. (a) Inbending and (b) outbending sets are shown separately. Each line represents a specific beam energy, increasing in energy with descending order from the upper left. Each color and marker style (red circles, cyan squares, light green triangles, magenta inverted triangles, blue open circles, orange crosses, gray open triangles, dark green diamonds) represents a different beam energy (1.606, 1.723, 2.286, 2.561, 4.238, 5.615, 5.725 and 5.743 GeV, respectively).

homogeneous medium as the ratio of their magnetic moments ($P_{^{15}\text{N}}/P_H \approx \mu_{^{15}\text{N}}/\mu_H \approx -0.09$) at small polarizations, with higher order terms increasing the magnitude of this ratio at larger polarizations [89]. An empirical fit for ^{15}N polarization as a function of proton polarization,

$$P_{^{15}\text{N}} = -(0.136P_p - 0.183P_p^2 + 0.335P_p^3), \quad (54)$$

derived in the SLAC E143 experiment for $^{15}\text{NH}_3$ [37], was applied to determine the nitrogen polarization.

The 3:1 $^1\text{H}/^{15}\text{N}$ ratio and the relative alignment of the proton and ^{15}N polarizations in the nuclear shell model [111] require factors of $\frac{1}{3}$ and $-\frac{1}{3}$, respectively, on this polarization, such that $P_{^{15}\text{N}}^* = -\frac{1}{9}P_{^{15}\text{N}}$ in Eq. (49). Systematic uncertainties were estimated by replacing the fit of Eq. (54) with the leading-order EST estimate ($P_{^{15}\text{N}} = 0.09P_p$) and reanalyzing.

Elastic ep events were also affected by the nuclear polarization, though the effect was less, due to the smearing of the ^{15}N quasi-elastic peak. We estimated $P_{^{15}\text{N elastic}} \approx \frac{1}{2}P_{^{15}\text{N}}$, and set $P_{^{15}\text{N elastic}} = 0$ to determine the uncertainty of this effect.

4. Radiative corrections

Radiative corrections to the measured asymmetries $A_{||}$ were computed using the program RCSLACPOL, which was developed at SLAC for the spin structure function experiment E143 [107]. Polarization-dependent internal and external corrections were calculated according to the prescriptions in Refs. [112] and [108], respectively.

The polarized and unpolarized radiated cross sections can be expressed as

$$\Delta\sigma_r = \Delta\sigma_B(1 + \Delta\delta_v) + \Delta\sigma_{el} + \Delta\sigma_{qe} + \Delta\sigma_{in} \quad (55)$$

and

$$\sigma_r = \sigma_B(1 + \delta_v) + \sigma_{el} + \sigma_{qe} + \sigma_{in} \quad (56)$$

respectively, in which σ_B is the Born cross section; δ_v is the combined electron vertex, vacuum polarization, and internal bremsstrahlung contributions; and σ_{el} , σ_{qe} , and σ_{in} are the nuclear elastic, quasi-elastic, and inelastic radiative tails (the quasi-elastic tail is, of course, absent for a proton target). The radiated asymmetry is given by

$$A_r = \frac{\Delta\sigma_r}{\sigma_r}. \quad (57)$$

For a given bin, one can write the Born asymmetry as

$$A_B = \frac{A_r}{f_{RC}} + A_{RC} \quad (58)$$

in which $f_{RC} = 1 - \sigma_{el}/\sigma_r$ is a radiative dilution factor (accounting for the “dilution” of the denominator of the asymmetry due to the radiative elastic tail) and A_{RC} is an additive correction accounting for all other radiative effects. We calculated these two terms using parametrizations of the world data for elastic form factors G_E and G_M , structure functions F_2^p and R^p , and virtual photon asymmetries A_1^p and A_2^p (see Sec. VC).

External corrections, dependent on the polar angle of scattering, were calculated using a realistic model of all the materials in the beam path within the vertex cuts for good electrons. RCSLACPOL is equipped to integrate over target raster position and scattering point within the target. However, studies have shown little difference from the case of fixing the scattering at the target center, which was assumed here. The peaking approximation, which speeds the calculation and has a negligible effect on the final result, was also exploited.

Both the internal and external corrections were combined and used to extract the Born asymmetries from the data. Radiative effects tend to be large near threshold (below $W = 1.2$ GeV) and at large W where the radiative tails begin to dominate.

Systematic uncertainties on these corrections were estimated by running RCSLACPOL for a range of reasonable variations of the models for F_2^p , R^p , A_1^p and A_2^p (see Section VC) and for different target and LHe thicknesses ℓ_A and L . The changes due to each variation were added in quadrature and the square root of this quantity is taken as the systematic uncertainty on radiative effects.

5. Systematic uncertainties

Estimation of systematic uncertainties on each of the observables discussed in the following section was done by varying a particular input parameter, model, or analysis method (as described in the preceding subsections), repeating the analysis, and recording the difference in output for each of the final asymmetries, structure functions, and their moments. Final systematic uncertainties attributable to each altered quantity were then added in quadrature to estimate the total uncertainty.

Sources of systematic uncertainties have been extensively discussed in the preceding text. These sources include kinematic accuracy, bin smearing, target model (radiative corrections), nuclear dilution model, elastic asymmetry measurement, $P_b P_t$ statistics, and background contamination.

The magnitudes of the effects of the various systematic uncertainties on the ratio g_1^p/F_1^p for the four beam energies are listed in Table I. Note that for each quantity of interest (A_1^p, g_1^p, Γ_1^p) the systematic uncertainty was calculated by the same method (instead of propagating it from other quantities), therefore ensuring that all correlations in these uncertainties were properly taken into account.

The results shown in the next section incorporate these systematic uncertainties.

Systematic uncertainty	Max. Relative Magnitude (g_1^p/F_1^p)			
	1.6 GeV	2.5 GeV	4.2 GeV	5.7 GeV
Kinematic smearing	2.0%	1.5%	1.0%	0.5%
Target material tolerances	2.5%	2.5%	2.5%	2.5%
L, ℓ_A target lengths	1.5%	1.5%	1.5%	1.5%
F_{DF} cross-section model	4.5%	2.0%	2.0%	2.0%
$P_b P_t$ elastic ep cuts	1.5%	1.5%	1.5%	1.5%
$P_b P_t$ statistics	0.8%	1.1%	1.7%	2.2%
π^- contamination	0.1%	0.8%	0.8%	1.5%
e^+e^- contamination	1.0%	1.0%	1.0%	1.0%
^{15}N polarization	0.5%	0.5%	0.5%	0.5%
Models for F_2^p, R^p, A_1^p, A_2^p	2.0%	2.0%	2.0%	2.0%
Totals	6.4%	4.9%	5.0%	5.2%

TABLE I. Systematic uncertainties

V. RESULTS AND COMPARISON TO THEORY

A. Extraction of $A_{||}$

The raw double-spin asymmetry [Eq. (47)] was evaluated for each group of data with a given beam energy, torus polarity, direction of the target polarization, and status of the HWP (in-out). For each group, the raw data were combined in (W, Q^2) bins with bin width $\Delta W = 10$ MeV. The Q^2 bins were defined logarithmically, with 13 bins in each decade of Q^2 . These bin sizes were chosen to provide a compromise between statistical significance and expected structure in the asymmetries.

The data in the various groups were combined as follows. First, raw asymmetries with the same beam energy, target spin direction, and torus polarity, but opposite half-wave-plate (HWP) orientation, were combined, bin by bin, weighting the data in each bin according to their statistical uncertainty. Next, the data sets with opposite target polarizations were combined using the product $\sigma_A^2 (P_b P_t)_{rel}^2$ as the weighting factor to optimize the statistical precision of the result. Here, σ_A is the statistical uncertainty of the raw asymmetry and $(P_b P_t)_{rel}$ is a quantity proportional to the product of beam and target polarization for a given data set. To get the highest possible statistical precision for this quantity, we calculated it by using not only elastic (exclusive) scattering data (c.f. Sec. IV E 2), but by taking the ratio of the measured raw asymmetry to that predicted by our model (see Sec. V C) for *all* kinematic bins (including elastic scattering) and averaging over the entire data set. The resulting value for $(P_b P_t)_{rel}$ deviates from the “true” product of polarizations by a constant unknown scale factor which is the same for the two data sets with opposite target polarization and therefore plays no role for the purpose of deriving a relative weight for these two sets.

All corrections except radiative corrections were then applied to the combined sets. Next, the asymmetries from sets with opposite torus polarity (but identical beam energy) were averaged (again weighted by statistical uncertainty). Finally, radiative corrections, described in Sec. IV E 4, were applied, resulting in measurements of $A_{||}$ for each beam energy (see Fig. 24).

B. Extraction of polarized asymmetries and structure functions

The asymmetries $A_1(Q^2, W)$ and $A_2(Q^2, W)$ are linearly related to $A_{||}(Q^2, W)$ by Eq. (18). The kinematical depolarization factor D in this equation is given in Eq. (14). The structure function R^p was calculated from a fit to the world data (see next section). For each final set discussed in the previous section, the values of $A_{||}/D = A_1^p + \eta A_2^p$ were calculated for each bin. For sets with beam energies differing by less than 15%, these values for $A_{||}/D$ were combined (with statistical weighting) and the corresponding beam energies averaged (see Fig. 25). These results have a low theoretical bias from modeled asymmetries and structure functions (like A_1 and F_1) compared to other extracted quantities. They can be found (along with the other results presented here) in the CLAS database [113] and in the Supplemental Material [114] for this paper.

Over a large kinematic region, asymmetries in the same (Q^2, W) bins were measured at multiple beam energies. Consequently, for these bins, A_1^p and A_2^p can be obtained from a Rosenbluth-type of separation, as follows. For fixed values of Q^2 and W , $A_{||}/D$ is a linear function of the parameter η which depends on the beam energy. A linear fit in η determines both A_1^p and A_2^p . An example of this is shown in Fig. 26. One disadvantage of the method is its large sensitivity to uncertainties in the dilution factor and in

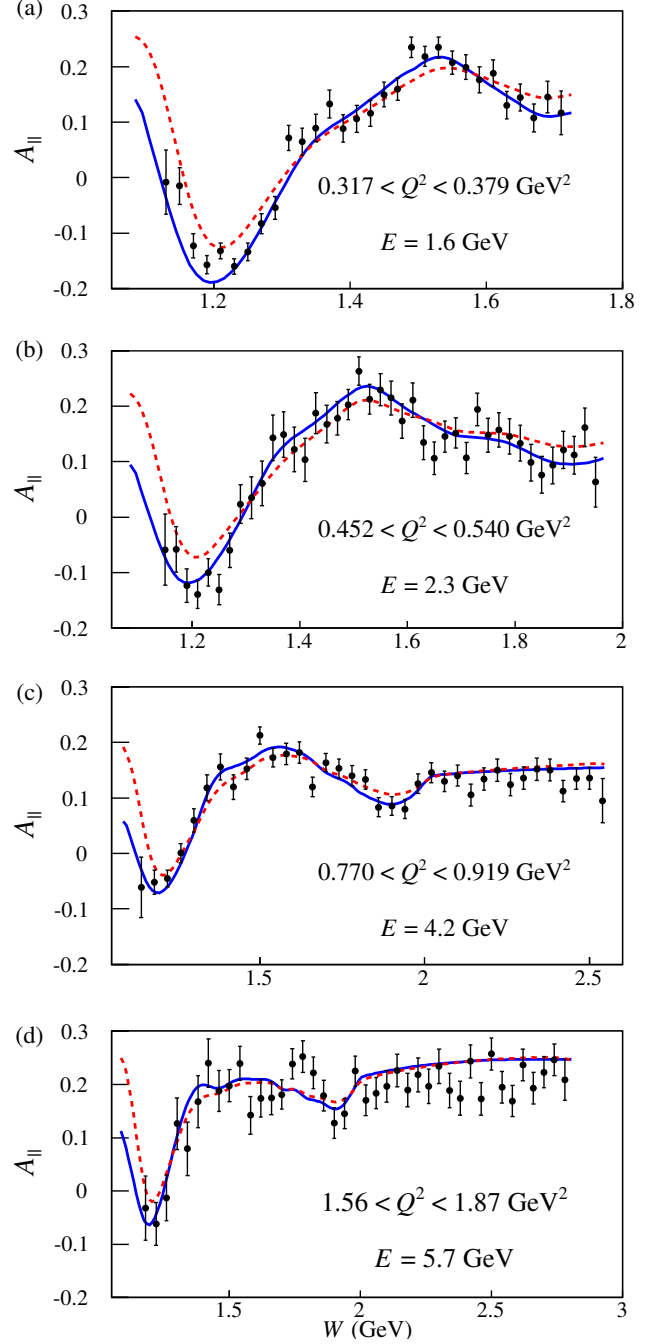


FIG. 24. (Color online) Values of $A_{||}$ (including radiative corrections) shown at beam energies of (a) 1.6, (b) 2.3, (c) 4.2, and (d) 5.7 GeV. The curves correspond to our model with (blue solid line) and without (red dotted line) radiative corrections, as discussed in the text.

$P_b P_t$ values for different beam energies.

For $W < 2$ GeV, the model-independent results for A_2^p are shown in Fig. 27, and compared to our model for A_2^p , as well as to data from RSS [22] (limited to $Q^2 = 1.3$ GeV²), MIT Bates [44], and NIKHEF (unpublished). For these plots, bins have been combined to increase the statistical resolu-

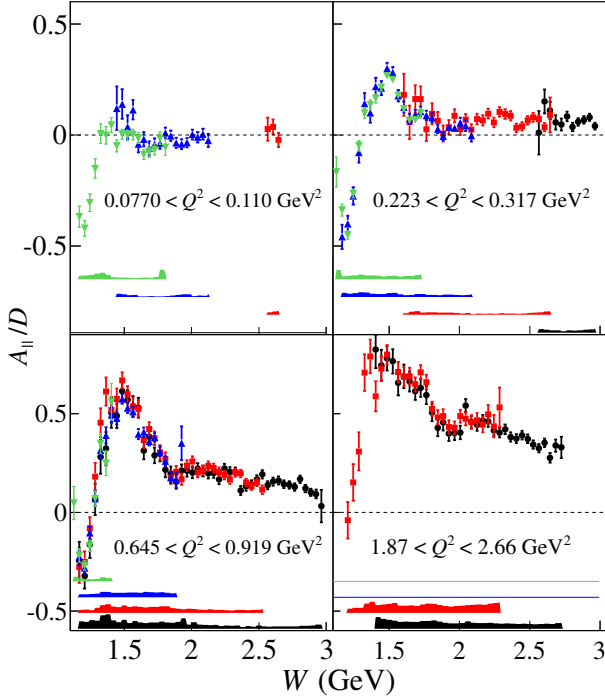


FIG. 25. (Color online) Values of A_{\parallel}/D vs W for each beam energy, including systematic uncertainties. The green inverted triangles, blue triangles, red squares and black circles correspond to data from approximate beam energies of 1.6, 2.5, 4.2 and 5.7 GeV, respectively.

tion. Although our results for A_2^p lack the precision of the RSS [48] experiment, they extend over a wider range of Q^2 .

For $W > 2$ GeV, we rarely have more than two beam energies contributing to any given kinematic point, and usually only the highest two beam energies. This yields a rather poor lever arm in η and makes any check of the linear fit (as well as its uncertainty) impossible. For this reason, we do not quote any results for A_2^p in the DIS region.

The spin structure function g_2^p

A model-independent value of g_2^p can be obtained if one expresses A_{\parallel} directly as a linear combination of g_1^p and g_2^p , again with energy dependent coefficients and a model for the unpolarized structure function F_1^p [see Eq. (15)]. For (Q^2, W) bins measured at more than one energy, g_1^p and g_2^p can then be determined with a straight-line fit, along with a straight-forward calculation of the statistical uncertainty. As already discussed, this is not the best way to determine g_1^p , but it does provide model-independent values for g_2^p . The results for the product xg_2^p averaged over four different Q^2 ranges are displayed as a function of x in Fig. 28. Although the precision is not particularly good, these data could provide some constraints on models of g_2^p .

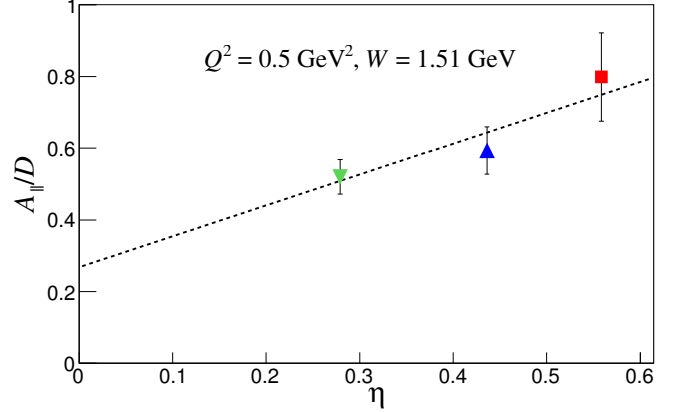


FIG. 26. (Color online) Representative linear fit of A_{\parallel}/D versus η for one W, Q^2 bin (at $W = 1.51$ GeV and $Q^2 = 0.5$ GeV²). The three points were taken at three different beam energies (color and style coded as in Fig. 25). The y intercept gives A_1^p and the slope gives A_2^p .

C. Models

In order to extract high-precision observables of interest from our data on A_{\parallel} , we need to use models for the unmeasured structure functions F_1^p and F_2^p (or, equivalently, F_1^p and R^p), as well as for the asymmetry A_2^p , which is only poorly determined by our own data (see above). Using these models, we can extract A_1^p and g_1^p from the measured A_{\parallel} , as explained in Sec. II B. In addition, we also need a model for A_1^p , covering a wide kinematic range, in order to evaluate radiative corrections stemming from both the measured and the unmeasured kinematic regions, and to evaluate the unmeasured contributions to the moments of the structure function g_1^p .

For the unpolarized structure functions F_1^p and R^p , we used a recent parametrization of the world data by Bosted and Christy [105]. This parametrization fits both DIS and resonance data with an average precision of 2–3%. In particular, it includes the extensive data set on separated structure functions collected at Jefferson Lab’s Hall C [115] which is very well matched kinematically to our own asymmetry data. Furthermore, the fit has been modified to connect smoothly with data for real photon absorption, thereby yielding a fairly reliable model for the (so far unmeasured) region of very small Q^2 . Systematic uncertainties due to these models were calculated by varying either F_1^p or R^p by the average uncertainty of the fit (2–3%) and recalculating all quantities of interest.

For the asymmetries, we developed our own phenomenological fit to the world data, including all DIS results from SLAC, HERA and CERN and all results from Jefferson Laboratory data (see Ref. [2] for a complete list) as well as data in the resonance region from MIT Bates [44]. In particular, we used an earlier version of this fit [13] for a preliminary extraction of A_1^p from our own data, and then iterated the fit including these data.

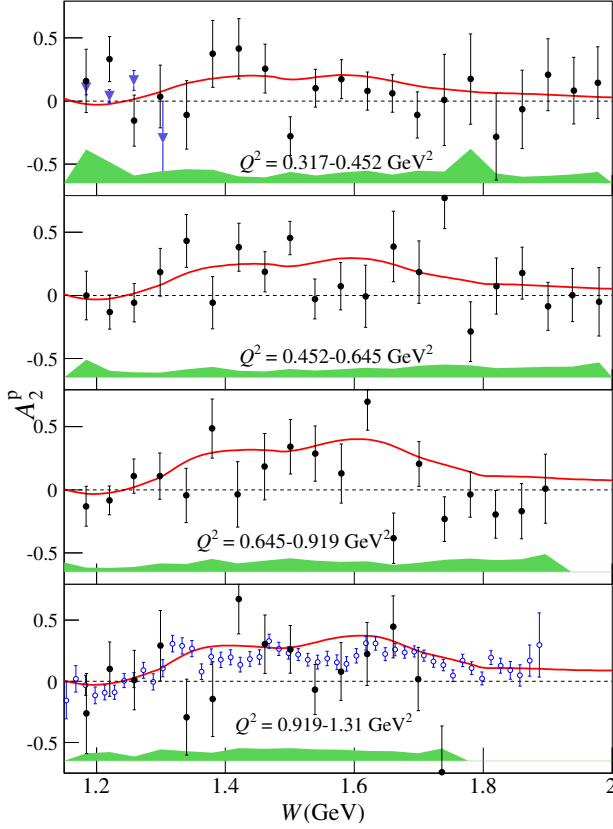


FIG. 27. (Color online) A_2^p vs W extracted from the EG1b data (black filled circles) together with the RSS (blue open circles) [22] and Bates (purple inverted triangles) [44] data. The EG1b model (red solid line) is shown for comparison. The green band shows the systematic uncertainty.

The fit proceeded in the following steps:

1. The asymmetry $A_1^p(x, Q^2)$ in the DIS region, $W > 2$ GeV, was fit using an analytic function of Q^2 and the variable $\xi' = \xi(1 + 0.272 \text{ GeV}^2/Q^2)$, where the Nachtmann variable ξ given in Eq. (24) was modified to allow a smooth connection to a finite value at the real photon point, $Q^2 = 0$. The seven parameters of this function were optimized by fitting this function to all world data at $W > 2$ GeV and the fit function, including real photon data from ELSA and MAMI (see, e.g., the summary by Helbing [116]). Each experiment was given an adjustable normalization factor as an additional parameter which was allowed to vary within the stated uncertainty due to global scale factors like the product $P_b P_t$. Some comparisons of the fit with world data (including the ones reported here) are shown in Figs. 29 and 30. The full error matrix from the fit was used to calculate the uncertainty of our model A_1^p at any particular kinematic point. All values of A_1^p used in radiative corrections or moments were moved by this uncertainty (one standard deviation) to determine the systematic uncertainty from this model.

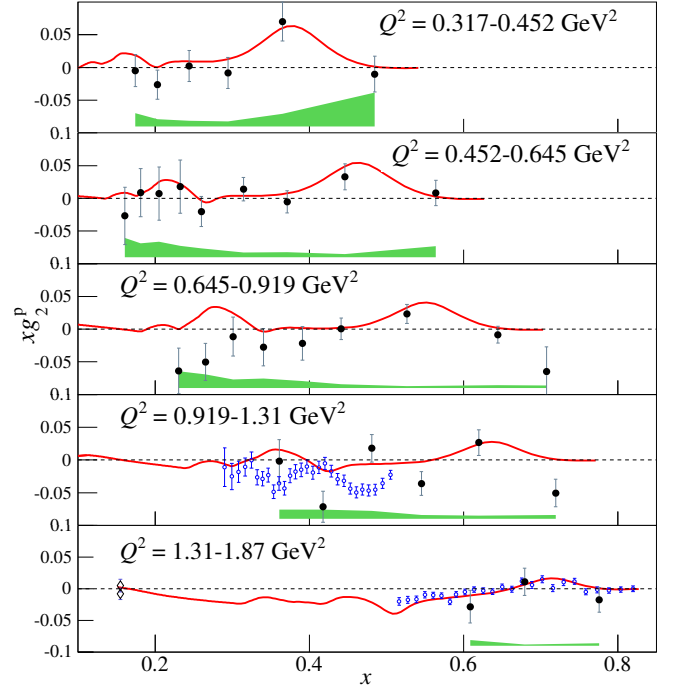


FIG. 28. (Color online) xg_2^p vs Bjorken x for the proton (solid black circles), together with RSS data (blue open circles) [22] and E155x data [41] (diamonds). The red curve is our model for the Q^2 bin median (which differs significantly from the average Q^2 value for the other data sets).

2. The asymmetry $A_2^p(x, Q^2)$ in the DIS region was modeled by using the Wandzura-Wilczek form of the structure function g_T [Eq. (25)] and observing that $A_2^p = \gamma g_T / F_1^p$ [Eq. (17)]. This description was found by SLAC experiments E143 and E155 to hold rather well; as a systematic variation, we also included a simple functional form for an additional “twist-3” term introduced by E155 [41].
3. In the resonance region, we modeled both asymmetries by combining the DIS fits (extrapolated to $W < 2$ GeV) with additional terms emulating resonant behavior. For the latter, we used the MAID parametrization of the cross sections $\sigma_{TT} = \sigma_T^{\frac{1}{2}}(\gamma^*) - \sigma_T^{\frac{3}{2}}(\gamma^*)$, $\sigma_T = \sigma_T^{\frac{1}{2}}(\gamma^*) + \sigma_T^{\frac{3}{2}}(\gamma^*)$, and $\sigma_{LT}(\gamma^*)$ for single pion and η production [117, 118]. We fit all data in the resonance region using Q^2 - and W -dependent weighting factors for these two terms, which guaranteed a smooth connection to the DIS fits at $W = 2$ GeV and for $Q^2 \rightarrow 10 \text{ GeV}^2$ (assuming negligible effects from resonances at higher Q^2). We included our model-independent results for A_2^p described in the previous section, as well as the more precise data from RSS [22] and MIT-Bates [44]. Ultimately, we combined this fit with an earlier version [13] for the best possible description of all data, and used the difference with the earlier version as a systematic uncertainty. A total of 28 parameters for A_1^p and 9 parameters for A_2^p were

fit using χ^2 minimization. The data for A_2^p are sparse and therefore fewer parameters were sufficient. We used the Soffer inequality [Eq. (22)] as an additional constraint. The resulting uncertainty on A_2^p was small enough for our purpose of extracting A_1^p and g_1^p as discussed below. The final implementation of our fit is in the form of a fine-grained lookup table that can be interpolated in both W and Q^2 . The reason for this is that we did not have access to a version of the MAID code that would allow us to calculate the necessary input to our model in real time; instead, we used a grid of values. Comparisons of our fit with our own data for A_2^p and A_1^p are shown in Fig. 27 and in Figs. 29 and 30, respectively.

D. Model-dependent extraction of A_1^p

Because of the relatively small contribution of A_2^p to $A_{||}$, even our only moderately constrained model estimation of A_2^p permits a rather accurate extraction of A_1^p over a large range of Q^2 and W . A_1^p was determined directly from Eq. (18), using our models for R^p and A_2^p as input.

A_1^p was extracted for each (Q^2, W) bin, separately for each data set obtained with the four average beam energies (1.6, 2.5, 4.2, and 5.7 GeV). The statistically averaged values of η in each bin were used to prevent weighting uncertainties. Final results for A_1^p measured at each beam energy were then statistically averaged. For each combination, we checked first that the values of A_1^p from different beam energies were statistically compatible (which turned out to be true in all cases). The final results are shown in Figs. 29 and 30.

Inclusive electron scattering at $W < 2$ GeV and low to moderate Q^2 is characterized by a strong W -dependence arising from the excitation of nucleon resonances (see Ref. [119] for a review). One typically observes three cross section peaks, traditionally labeled as the first, second, and third resonance regions. As discussed in Sec. II C, the total spin of an excited resonance is reflected in its contribution to A_1^p . The first resonance region is dominated by excitation of the $\Delta(1232)P_{33}$ resonance, with total spin $S = \frac{3}{2}$ and $W = 1.232$ GeV. As discussed in Sec. II C, $A_1^p \approx -\frac{1}{2}$ in this region from the resonance contribution alone. This is borne out by our data for the lowest Q^2 , while at higher Q^2 non-resonant background and tails from higher-lying resonances begin to dominate, making A_1^p less negative. The second resonance region arises from excitation of a group of closely spaced resonances, in particular $N(1535)S_{11}$ and $N(1520)D_{13}$. Between the first and second regions, the excitation of the Roper resonance $N(1440)P_{11}$ is not prominent in electro-excitation at low Q^2 where the leading amplitude crosses zero, but it contributes significantly above $Q^2 = 2$ GeV² over a region three times as broad in W as the $\Delta(1232)P_{33}$, creating a shoulder in A_1^p around $W = 1.44$ GeV, which is visible in our data. This and other spin- $\frac{1}{2}$ resonances, which have no spin- $\frac{3}{2}$ projection, lead to $A_1^p = 1$ for the resonance contribution only. In the

second region the dominant $N(1535)S_{11}$ resonance drives A_1^p toward unity. The other major resonance in this region, $N(1520)D_{13}$, has $A_1^p = -1$ for real photons ($Q^2 = 0$) but it rapidly tends toward $A_1^p = +1$ for $Q^2 > 3$ GeV², characteristic of pQCD expectations. Indeed, our data exhibit a rapid rise from $A_1^p \approx 0$ at low Q^2 to large positive values at higher Q^2 in this region. The third resonance peak lies at $W = 1.63$ GeV and contains, among others, the $N(1680)F_{15}$ resonance. Additional enhancements in the real photon cross section arise from excitation of a number of resonances with $1.7 < W < 1.9$ GeV, some of which are spin- $\frac{3}{2}$ or higher and therefore tend to have negative A_1^p . These features are visible as well in our data at low Q^2 . Another prominent feature is the nearly uniform increase of A_1^p with increasing Q^2 .

As discussed in Sec. II C, predictions of the high x DIS behavior of A_1^p are strongly model-dependent, although most realistic models predict some sort of smooth approach to the value $A_1^p = 1$ at $x = 1$, which would be consistent with A_1 for elastic scattering. To compare our results for A_1^p to the world's DIS data, we restricted the kinematical region to $W > 2$ GeV to avoid complications from the resonance region, which clearly shows departures from DIS behavior. With this restriction on W , the upper limit of $x = 0.6$ for our data is fixed by the maximum JLab electron energy. The results obtained with this restriction are compared to world DIS data for A_1^p in Fig. 31. This plot also displays several predictions and fits of the x -dependence of A_1^p : a “statistical” model for quark distribution functions by Soffer *et al.* [120], an NLO fit to the world data without constraint at $x = 1$ by Leader, Stamenov and Siderov *et al.* [121], a range of predictions from a relativistic quark model with hyperfine interactions due to one-gluon exchange [24], and two different models based on pQCD expectations, one without (BBS [25]) and one with (BBS+OAM [27]) quark orbital angular momentum.

Several features are obvious. Our data tend to lie lower than the EG1-dvcs data, not because of large discrepancies (as can be seen in Fig. 33), but due to the significantly different kinematics between these two data sets, which affects the Q^2 range over which we average, and the impact of various models (in particular, A_2^p). Our model fit confirms that indeed even in the DIS region, $A_1^p(x, Q^2)$ is not completely Q^2 -independent (scaling), but rather increases as Q^2 increases. Taking this effect into account, our data are in good agreement with the world data set. At moderately high x , our data show an unambiguous increase, as expected, beyond the naive SU(6) quark model prediction of $A_1^p = 5/9$.

E. The spin structure function g_1^p

Analogous to the case for A_1^p , the most precise results for g_1^p can be extracted from our measurement of $A_{||}$ using models for all unmeasured structure functions, including A_2^p [see Eq. (19)]. Over most of our kinematics $|\gamma - \eta| \ll |\eta|$, which ensures that the uncertainty in our A_2^p model is

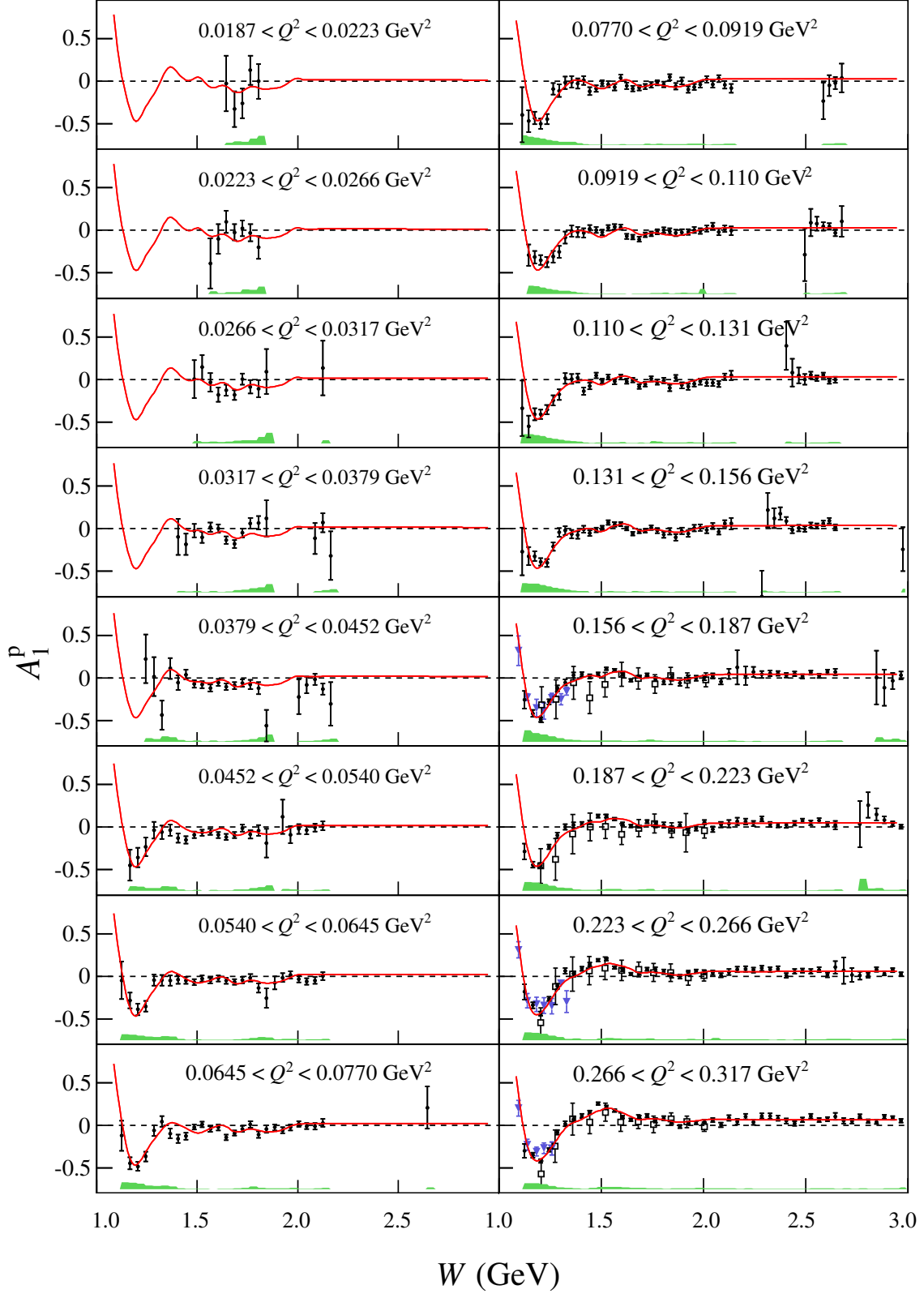


FIG. 29. (Color online) Asymmetries A_1^p vs W for bins in Q^2 . The solid black points are our data with statistical error bars. Open squares represent EG1a data [12], and the purple triangles are Bates data [44], visible on the left side of three of the four highest Q^2 plots shown. The red line shows our model of A_1^p for comparison. The green bands show the systematic uncertainties.

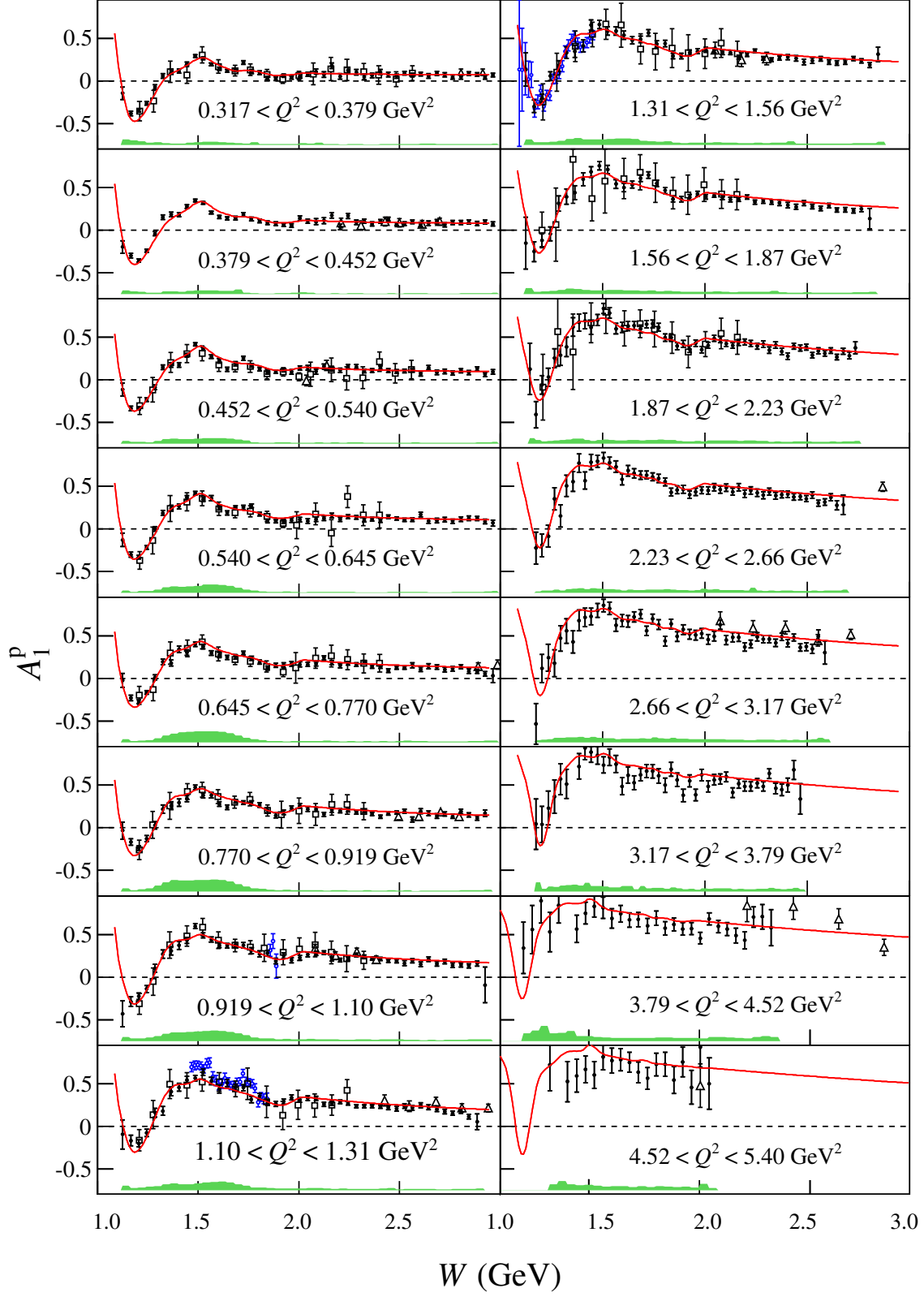


FIG. 30. (Color online) Same as Fig. 29 but for the higher Q^2 bins. Additionally, here, blue hollow circles are RSS data [22], and open triangles are E143 data [37].

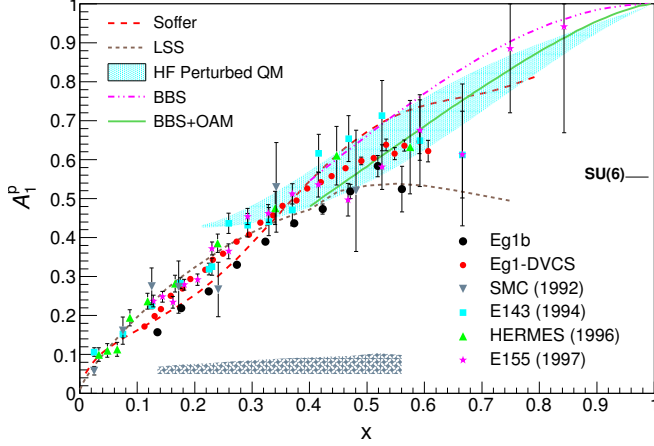


FIG. 31. (Color online) A_1^p vs x for DIS events, $W > 2$ GeV, compared to world data. Curves and models are discussed in the text. The difference between EG1b data and higher energy data is discussed in the main text. The hatched region at the bottom represents the systematic uncertainty on the EG1b data.

even less important in the extraction of g_1^p/F_1^p than for the extraction of A_1^p . Consequently, the uncertainties on g_1^p/F_1^p are primarily statistical.

Our complete data set for the quantity $xg_1^p(x, Q^2)$ is shown in Fig. 32, together with a sample of world data. One can see a clear transition from the resonance-dominated behavior at low Q^2 with the prominent negative peak in the Δ resonance region towards the smooth behavior at high Q^2 , where most of the data lie in the DIS region. At intermediate Q^2 , one can discern an x dependence that still has some prominent peaks and dips, but approaches, on average, the smooth DIS curve at the highest Q^2 . This is a qualitative indication of quark-hadron duality, which is discussed below (see Sec. VH).

Plots of g_1^p/F_1^p as a function of Q^2 for various x bins are shown in Fig. 33. For comparison, these plots also show data from the SLAC E143 and E155 experiments. The solid line on each plot shows the result of our model at the median value of each bin. The systematic uncertainty is shown as the green region near the bottom of each plot. Again, a dramatic Q^2 dependence at low Q^2 (where the low- W region dominates for fixed x) makes way to the smooth approach towards the DIS limit at higher Q^2 . The remaining Q^2 dependence at the upper end of each plot hints at scaling violations of g_1^p/F_1^p due to pQCD evolution.

The quantity g_1^p was derived for all values of $A_{||}/D$ over the entire kinematic range using Eq. (19), with model values used for A_2^p and F_1^p . The complete coverage of g_1^p over the EG1b kinematic range is displayed in Fig. 34.

F. Moments of g_1^p

As discussed in Sec. IIG, moments of g_1^p and g_2^p with powers of x play an important role in the theory of nucleon structure in the form of sum rules and for the determination of matrix elements within the OPE. The n th moment of a structure function \mathcal{S} is defined by $\int_0^1 x^{n-1} \mathcal{S}(x, Q^2) dx$. Experimental data do not cover the complete range in x for each Q^2 bin (see Fig. 34), but the moments can be approximated using a combination of our data along with a model for low x and high x . Thus, the calculation can be expressed as

$$\begin{aligned} & \int_{x_{\text{high}}}^1 x^{n-1} \mathcal{S}(x, Q^2)_{\text{model}} dx \\ & + \int_{x_{\text{low}}}^{x_{\text{high}}} x^{n-1} \mathcal{S}(x, Q^2)_{\text{data}} dx \\ & + \int_{0.001}^{x_{\text{low}}} x^{n-1} \mathcal{S}(x, Q^2)_{\text{model}} dx. \end{aligned} \quad (59)$$

At very low values of x , uncertainties in the model become so large that we have chosen to truncate the lower limit at $x = 0.001$. Ignoring the interval $[0, 0.001]$ is expected to have little effect, especially for $n > 1$.

G. Moments of g_1^p

The n th x -weighted moment of g_1^p was determined from our data as follows. For each Q^2 bin the data were binned in W with $\Delta W = 10$ MeV, so that

$$I_{\text{data}}(Q^2) = \sum_W x_{\text{avg}}^{n-1} \mathcal{S}(Q^2, W) |x_a - x_b|, \quad (60)$$

where x_{avg} is the average value of x for the events contributing to each bin, and x_a and x_b are the lower and upper limits of the W bin. The statistical uncertainty for each bin was added in quadrature to obtain the statistical uncertainty on the integral. Bins with a statistical uncertainty for $A_{||}$ greater than 0.6 were excluded. In kinematic regions where data were absent or insufficient by this criterion, the model was used. The integral ran from the inelastic threshold ($W = 1.07$ GeV) up to the value of W corresponding to $x = 0.001$ for each Q^2 bin. The model was also integrated over the full x range for comparison to the data (see Fig. 35).

In our plots of the calculated moments, the experimental contributions are shown as open circles and the combination of model and data is shown as solid black circles. Systematic uncertainties were calculated using the methods described earlier and are shown in shaded bands.

The moment calculations presented here (with the exception of Fig. 37) do not include the contribution from elastic scattering at $x = 1$, which is the same for all n [see Eq. (30)].

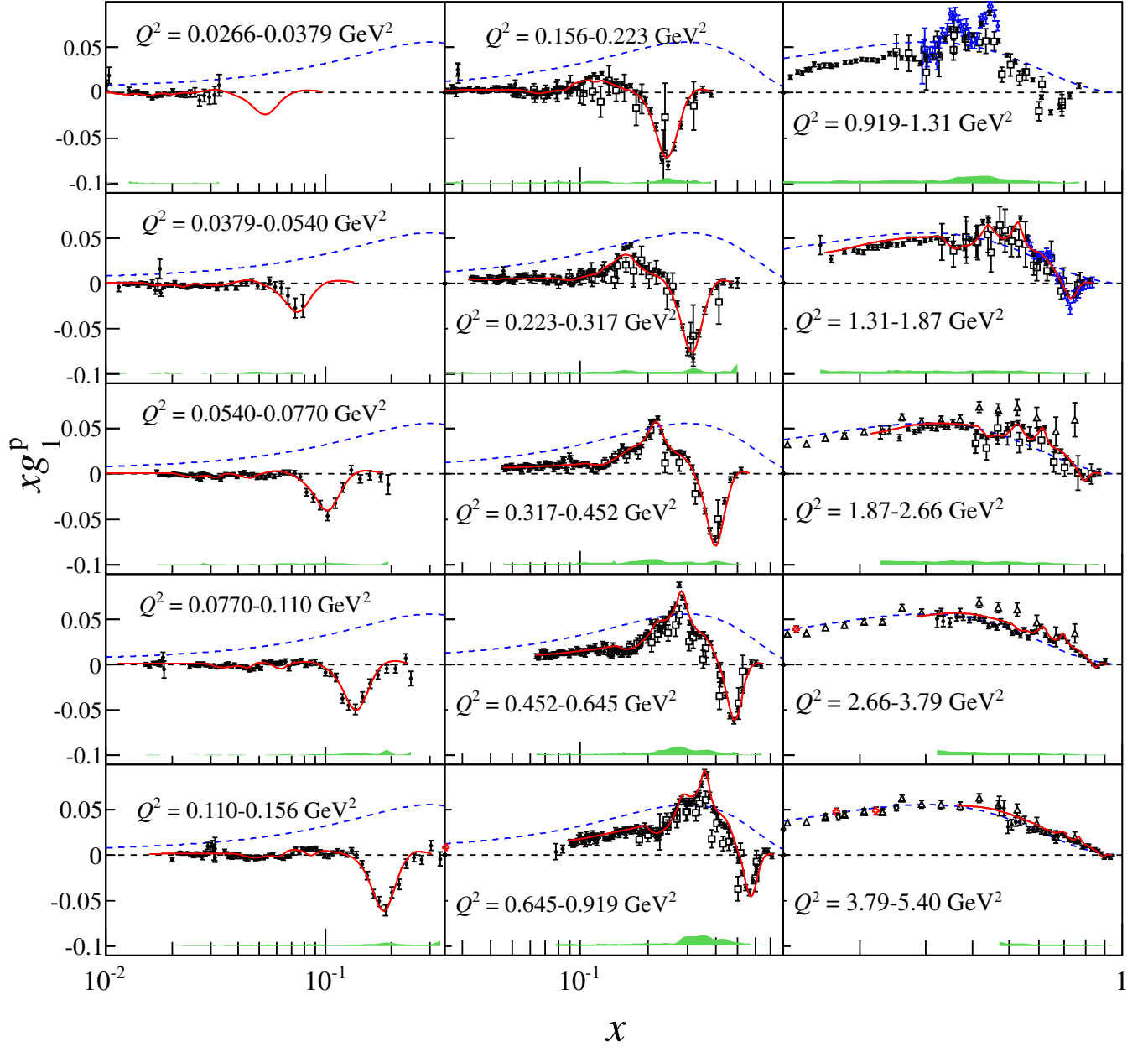


FIG. 32. (Color online) Spin structure function xg_1^p vs Bjorken x , for various bins in Q^2 . Our data (black points) are plotted along with the world data at similar Q^2 : from HERMES (red crosses) [35], E155 (diamonds) [40], E143 (hollow triangles) [37], RSS (blue circles) [22], and EG1a (hollow squares) [12]. The green band indicates total systematic uncertainties; the red solid line is our model for the median of each Q^2 bin, and the blue dashed line is the DIS model at $Q^2 = 10 \text{ GeV}^2$, included for reference.

1. The first moment Γ_1^p

The moments of g_1^p , designated as Γ_n^p have been calculated from our data up to $n = 5$. The first moment Γ_1^p is of special interest. At $Q^2 = 0$ the GDH sum rule constrains the slope of $\Gamma_1^p(Q^2)$ to be -0.456 GeV^{-2} [Eq. (41)]. At large Q^2 , Γ_1^p is related to squared charge-weighted axial charges of all quark species present in the nucleon (see

Sec. II G). From existing DIS data and theoretical expectations, it is well-known that in this limit Γ_1^p is positive and approaches a value of about 0.14–0.15, with a Q^2 dependence given by pQCD. Consequently, at some value of Q^2 , Γ_1^p must pass through zero. The plots of our results for Γ_1^p shown in Fig. 35 are consistent with these expectations, exhibiting a sign change at $Q^2 \approx 0.24 \text{ GeV}^2$.

Various models and parametrizations have been proposed to interpolate between the two extreme Q^2 limits. At high

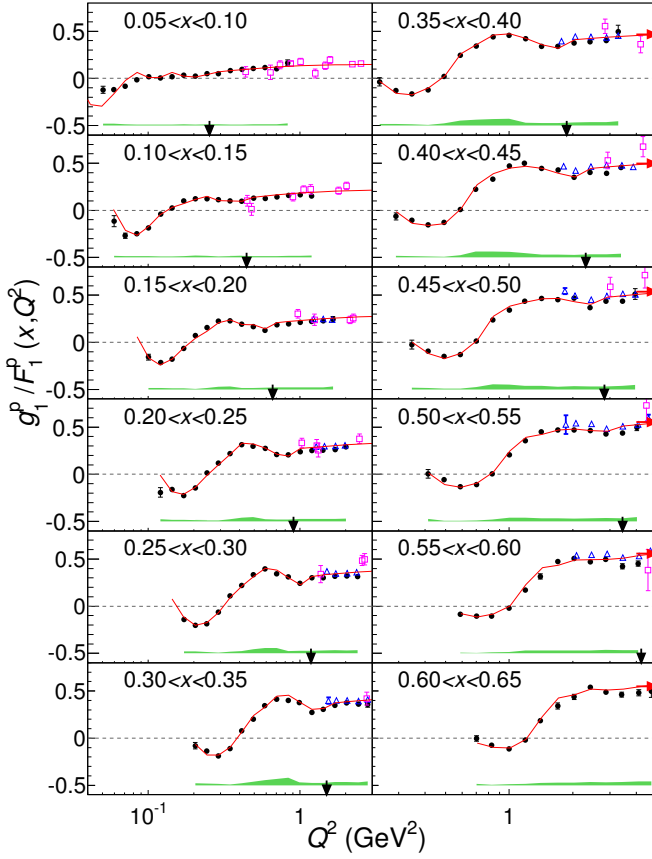


FIG. 33. (Color online) Plots of g_1^p/F_1^p versus Q^2 for different x ranges of the combined EG1b data. The (red) line represents our model. The blue triangles correspond to the EG1-dvcs data [23], while magenta squares represent E143 data [37]. The downward-pointing black arrows indicate the upper limit of the resonance region at $W = 2$ GeV, while the red horizontal arrows indicate the results for g_1^p/F_1^p of a recent analysis of world data for our bin centers and $Q^2 = 5$ GeV².

Q^2 , pQCD corrections up to third order in α_S have been calculated and are shown in Fig. 35, as is the “GDH slope” at $Q^2 = 0$. The next higher order terms in an expansion in Q^2 around the origin can be calculated within the framework of χ PT [125, 126]. Finally, we show two phenomenological curves using the methodology of Burkert, Ioffe, and Li [122, 123, 127] and by Soffer, Pasechnik *et al.* [124, 128, 129], which reproduce the data, at least qualitatively, quite well.

2. Higher moments

The third and fifth moments of g_1^p are shown in Fig. 36. These moments are characterized by small statistical uncertainties, along with very little model dependence for $Q^2 < 3$ GeV². They are useful in the calculation of hydrogen hyperfine splittings [130, 131].

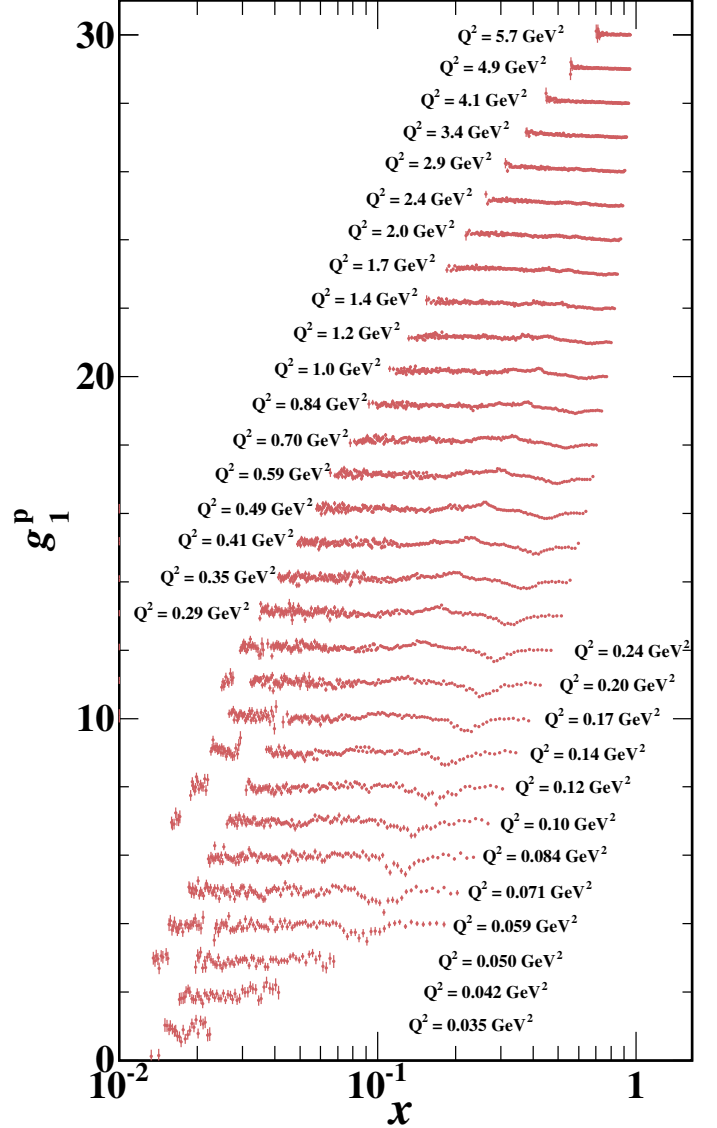


FIG. 34. (Color online) The full g_1^p data set from this experiment. For clarity, the n -th x distribution at fixed Q^2 is shifted upward by $1 + n$.

3. Higher twist analysis

We detail here the analysis performed to extract the twist-4 contribution f_2^p to g_1^p and to determine the contribution of the quarks to the nucleon spin $\Delta\Sigma$. A summary of the formalism describing the higher-twist matrix elements in the OPE has been presented in Sec. II G.

The data set analyzed comprised all the energies used for the EG1b analysis and the doubly polarized data from other JLab experiments (EG1a [12] and EG1-dvcs [23]) as well as the data from the SLAC, CERN and DESY facilities, including the recent COMPASS results [46]. The low- x ex-

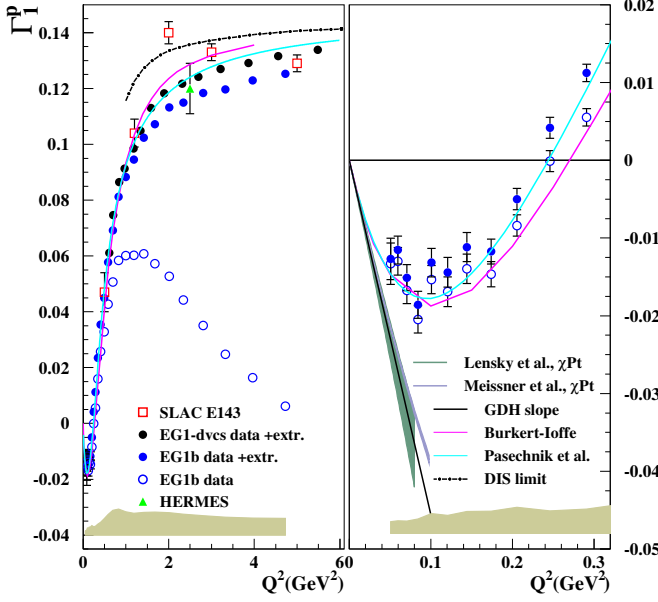


FIG. 35. (Color online) Γ_1^p vs Q^2 for EGIb data and selected world data. The right panel shows an expanded scale at small Q^2 . The open circles represent our data, integrated over the measured region. The filled blue circles are the full integral from $x = 0.001 \rightarrow 1$, excluding the elastic region. The curves show phenomenological parametrizations by Burkert and Ioffe [122, 123] (magenta) and Pasechnik *et al.* [124] (cyan). The limiting cases of large Q^2 (“DIS limit”) and $Q^2 \rightarrow 0$ (“GDH slope”) are also shown, as well as two bands showing χ PT calculations, (Lensky *et al.* [125] and Meissner *et al.* [126]). The green band at the bottom represents the total systematic uncertainty.

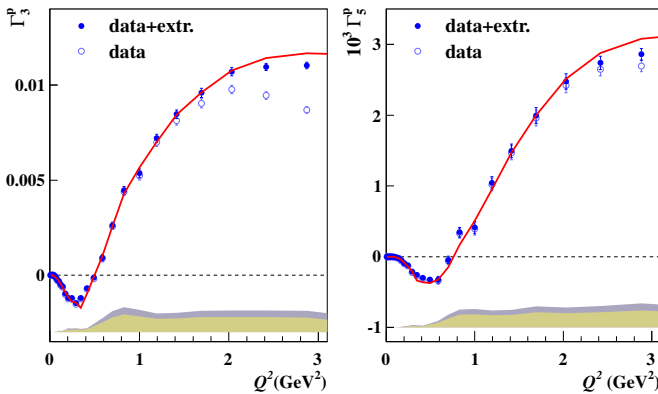


FIG. 36. (Color online) Γ_2^p and Γ_5^p vs Q^2 for EGIb data. Solid (blue) circles are the total integral, whereas the open (blue) circles are the integral over measured data. The curve (red) is our model. The gold and gray bands at the bottom represent the systematic uncertainties on the data and the data + model contributions, respectively.

parameter	starting value
f_2	0.
μ_6	0.
μ_8	0.
g_A	1.267 ± 0.035
a_8	0.579 ± 0.025
$\Delta\Sigma$	0.154 ± 0.2
$a_2(Q_0^2)$	0.0281 ± 0.0028
$d_2(Q_0^2)$	0.0041 ± 0.0011
Λ_{QCD}	0.340 ± 0.008

TABLE II. The nine parameters used in the fits, together with their starting values. Free parameters started at zero, whereas the fixed parameters (given with uncertainties) were varied from their central values to estimate uncertainties in the free parameters.

trapolation of world data was redone using our model (see Sec. VC) to obtain a consistent set of data. The model was used down to $x = 0.001$. The uncertainty was estimated by varying the model parameters and taking the quadratic sum of the resulting differences. Beyond $x = 0.001$ a Regge form [132] was used for which an uncertainty of 100% was assumed. The elastic contribution to the moments was estimated using the proton form factor parametrization of Arrington *et al.* [63]. The uncertainty was taken as the linear difference with another fit from Gayou *et al.* [133]. In the fitting procedure used to extract the higher-twist coefficients, all the uncertainties (experimental statistics and systematics, elastic and low- x extrapolation) are added in quadrature to obtain a total uncertainty. There are point-to-point correlations between the total uncertainties on different data points within individual experiments. They are also present between data points from different experiments (for example, the EGI-dvcs data are supplemented with a high- x extrapolation from a model significantly dependent on the EGIb data). To account for these correlations in the fit procedure, we use the *unbiased estimate* procedure, i.e. the total uncertainties are uniformly scaled so that the χ^2 per degree of freedom (dof) of the fit is forced to 1. It turns out that the global factor scaling the total uncertainties is close to 1 (see the last column of Table III).

First, we fit the world data (re-estimated using our model) for $Q^2 \geq 5 \text{ GeV}^2$ and assuming no higher-twist contribution above $Q^2 = 5 \text{ GeV}^2$. This yields $\Delta\Sigma = 0.169 \pm 0.084$. Next, we account for higher twists. The target mass correction $a_2(Q_0^2) = \int_0^1 dx (x^2 g_1^{LT}(x, Q_0^2))$, in which $g_1^{LT}(x, Q_0^2)$ contains only the twist-2 contribution to g_1 , was estimated with the parton distribution parametrization of Bluemlein and Boettcher [134]. Q_0^2 is a reference scale taken to be 5 GeV^2 . The twist-3 contribution $d_2(Q_0^2)$ was obtained from the SLAC E155x experiment [41]. A Q^2 -dependence of the form $A(Q^2) = A(Q_0^2) (\alpha_s(Q_0^2)/\alpha_s(Q^2))^b$ was assumed for $a_2(Q^2)$ and $d_2(Q^2)$ with the anomalous dimensions $b = -0.2$ and $b = -1$, respectively. A value of $\Lambda_{QCD} = 0.340 \pm 0.008$ [135] was used for computing $\alpha_s(Q^2)$. The variations of the six quantities g_A , a_2 , d_2 , A_8 , Σ and Λ_{QCD} during the χ^2 minimization were bounded

fit	Q_{min}^2 (GeV ²)	μ_{max}	f_2	μ_6/M^4	μ_8/M^6	$\Delta\Sigma$	Λ_{QCD} (GeV)	gf
0	5.00	2	-	-	-	0.169 ± 0.084	0.340 (kept fixed)	1.40
1	0.61	8	-0.087 ± 0.074	0.067 ± 0.055	0.003 ± 0.026	0.283 ± 0.051	0.347 ± 0.015	1.08
2	0.61	6	-0.102 ± 0.025	0.072 ± 0.009	-	0.335 ± 0.026	0.339 ± 0.013	1.06
3	0.81	8	-0.027 ± 0.017	0.000 ± 0.007	0.046 ± 0.012	0.256 ± 0.030	0.336 ± 0.005	1.11
4	0.81	6	-0.108 ± 0.038	0.076 ± 0.016	-	0.286 ± 0.035	0.332 ± 0.011	1.09
5	1.00	8	-0.018 ± 0.018	-0.009 ± 0.013	0.050 ± 0.021	0.261 ± 0.035	0.332 ± 0.009	1.22
6	1.00	6	-0.076 ± 0.066	0.060 ± 0.031	-	0.274 ± 0.060	0.336 ± 0.004	1.21

TABLE III. Results of the fits for various minimal Q^2 values (column 2) and truncations of the twist series. Data at Q^2 lower than Q_{min}^2 were not included in the fit. In column 3, μ_{max} indicates the order at which the twist series is truncated (μ_8 or μ_6). Column 4 gives the pure twist-4 coefficient, columns 5 and 6 give the $1/Q^4$ and $1/Q^6$ power correction coefficients, respectively. Column 7 gives the quark spin contribution to the nucleon spin, $\Delta\Sigma$. Column 8 lists Λ_{QCD} , and column 9 gives the global factor used to scale the total uncertainties in order to force $\chi^2/ndf = 1$.

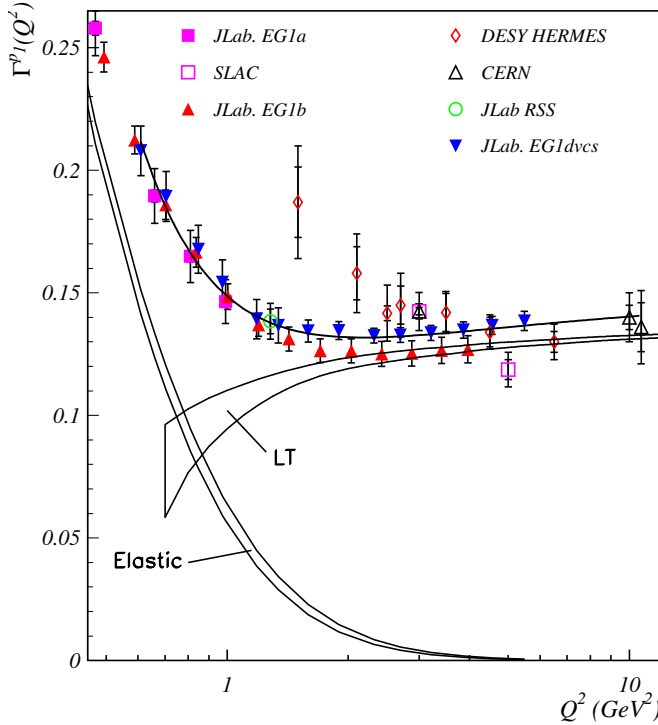


FIG. 37. World data on $\Gamma_1^p(Q^2)$. The band (LT) is the pQCD leading-twist evolution. The error bars represent statistical (inner bars) and total (outer bars) uncertainties after applying the unbiased estimate procedure. The solid black line is a fit of the data starting at $Q_{min}^2 = 0.6$ GeV². The band labeled “Elastic” shows the elastic contribution to $\Gamma_1^p(Q^2)$ with its uncertainty.

For a given higher-twist truncation order, the fit results are consistent with each other (see Table III), indicating that the Q_{min}^2 choice has an acceptably small influence. On the other hand, the results are not consistent for fits with different higher-twist truncation orders. This is to be expected since generally, $\mu_8 > \mu_6$. This is seen too in the higher-twist

within their respective error bars; see Table II for the values used and their bounds. Those, together with the (unbounded) fit parameters f_2 , μ_6 and μ_8 , made a total of nine fit parameters (three unbounded and six bounded).

The world data together with the OPE leading-twist evolution (LT) of $\Gamma_1^p(Q^2)$ and the elastic contribution to $\Gamma_1^p(Q^2)$ are shown in Fig. 37. The solid black line is the result of fit 1 (see Table III).

To check the convergence of the OPE series, the lowest Q^2 value, Q_{min}^2 , was varied, as well as the order of the OPE series (truncated to twist-6 or twist-8). The results are given in Table III.

analysis of the non-singlet part of Γ_1 , the Bjorken sum [131].

The f_2 results show the same trend as the results from the neutron [136] and Bjorken sum analysis [131]: The f_2 coefficient tends to display a sign opposite to the sign of the next significant higher twist coefficient. This may explain why the approach towards hadron-parton duality [54]

at fairly moderate Q^2 holds for g_1 at the scale at which the higher twist coefficients are extracted (see Sec. VH).

The quark spin sum obtained at lower Q^2 , accounting for higher twists, is $\Delta\Sigma = 0.289 \pm 0.014$, obtained from an average of our results. This is larger than, but compatible with, the leading-twist determination $\Delta\Sigma = 0.169 \pm 0.084$. It also agrees with the determinations obtained from global fits of PDFs, which are typically around $\Delta\Sigma = 0.24$ (see, e.g., Ref. [3] for a review). The discrepancy between the $\Delta\Sigma$ extracted from the proton and neutron analyses [137, 138] (with $\Delta\Sigma^{(n)} = 0.35 \pm 0.08$) is resolved by the new data.

Our results on f_2 can be compared to non-perturbative model predictions: $f_2 = -0.037 \pm 0.006$ [68], $\mu_4/M^2 = -0.040 \pm 0.023$ (QCD sum rules [71]), $f_2 = -0.10 \pm 0.05$ (MIT bag model [69]), and $f_2 = -0.046$ (instanton model [139]). As for the extracted f_2 , all the predictions are negative. The MIT bag model and QCD sum rules agree best with the typical fit result of $f_2 \simeq -0.1$, although the other predictions are not ruled out.

From the result of fit 6, we extract the proton color polarizabilities which are the responses of the color magnetic and electric fields to the spin of the proton [68, 69]. We obtain $\chi_E^p = -0.045 \pm 0.044$ and $\chi_B^p = 0.031 \pm 0.022$ [see Eq. (39)]. As is the case for the neutron [136] and p - n [131, 140], the extracted electric and magnetic polarizabilities are of opposite sign.

4. Spin polarizability γ_0^p

In the real photon limit $Q^2 \rightarrow 0$, the ep scattering cross section can be expressed in terms of Compton amplitudes, with coefficients α_E , β_M , and γ_0^p , called polarizabilities. The quantity γ_0^p , the forward spin polarizability, is given by

$$\gamma_0^p = \frac{1}{4\pi} \int_{\nu_{th}}^{\infty} \frac{\sigma_{\frac{3}{2}} - \sigma_{\frac{1}{2}}}{\nu} d\nu. \quad (61)$$

Converting the integration variable from ν to x yields Eq. (43), which can be recast as

$$\begin{aligned} \gamma_0^p &= \frac{16M^2\alpha}{Q^6} \int_0^{x_{th}} x^2 [g_1^p(x, Q^2) - \gamma^2 g_2^p(x, Q^2)] dx \\ &= \frac{16M^2\alpha}{Q^6} \int_0^{x_{th}} x^2 A_1^p(x, Q^2) F_1^p(x, Q^2) dx, \end{aligned} \quad (62)$$

in which x_{th} , the pion production threshold, excludes the elastic contribution. The polarizability in units of fm^{-4} is plotted in Fig. 38 (blue open circles, measured data; blue dots, extrapolated data), along with the real photon γ_0^p ($Q^2 = 0$) obtained from the MAMI GDH experiment [141–143]:

$$\gamma_0^p = [-1.01 \pm 0.08 \pm 0.10] \times 10^{-4} \text{ fm}^{-4}. \quad (63)$$

Within experimental uncertainties, our measurements at low Q^2 are consistent with the MAMI measurement.

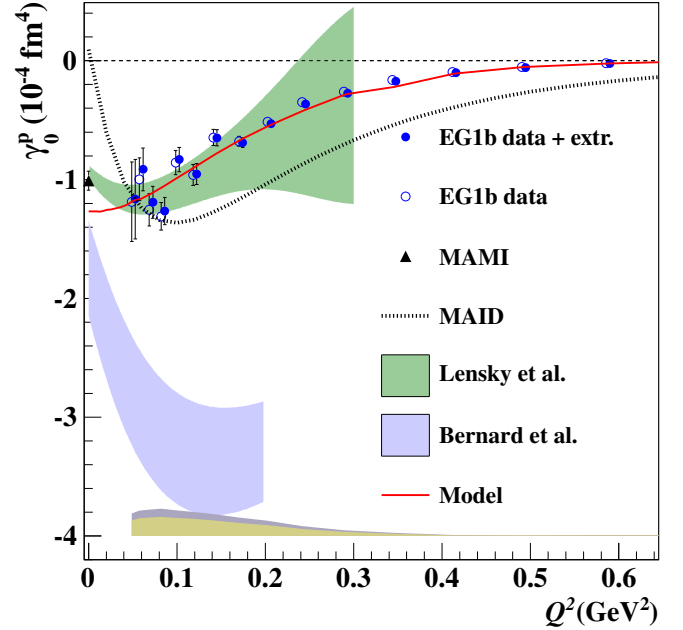


FIG. 38. (Color online) The forward spin polarizability γ_0^p vs Q^2 . Open and closed circles represent the contribution to the integral from the data only and the data plus model, respectively (slightly offset horizontally for clarity). Our model is shown as a solid red line. Our results are compared to χ PT calculations (as in Fig. 35), the MAID parametrization for single-pion production, and real photon data at $Q^2 = 0$ from MAMI [141–143].

H. Bloom-Gilman duality

As discussed in Sec. IID, our data provide a substantial test of Bloom-Gilman duality in polarized electron scattering. Comparisons of theory and experiment have shown that unpolarized structure functions exhibit both a “global duality” (integration over the entire resonance region at $W < 2$ GeV) and a “local duality” in each of the three main resonance regions. For polarized scattering at low Q^2 , the importance of the hadronic picture is clearly shown by the observed values of g_1^p in the resonance region, where the interplay of $\sigma_{\frac{1}{2}}$ and $\sigma_{\frac{3}{2}}$ is obvious. The Δ region, where $g_1^p < 0$, is an extreme case, since for DIS in the scaling region $g_1^p > 0$ for all x . It may still be possible, however, for global duality to apply in the resonance region at relatively low Q^2 .

Hence, we looked for evidence of local and global duality for $0.5 < Q^2 < 5 \text{ GeV}^2$ by applying duality tests to determine at what values of (Q^2, W) the DIS behavior represents the average polarization response in the resonance region. A first study of duality for spin structure functions using the CLAS data for both polarized proton and deuteron targets was carried out and reported in an earlier publication [16].

For comparison with our data above $Q^2 = 1 \text{ GeV}^2$, QCD fits to DIS polarized structure function data above the res-

onance region were evolved towards lower Q^2 by an NLO calculation. This evolution is expected to give reasonable results down to $Q^2 \approx 1 \text{ GeV}^2$. The NLO evolution was chosen to give the best estimate of the Q^2 dependence of g_1^p . Target mass effects were taken into account using the prescription of Blümlein and Tkabladze [58] as before. Recent fits to the unpolarized structure functions F_1 for the proton and deuteron were used to extract g_1 for both the proton and the deuteron from our data for $E=1.6 \text{ GeV}$ and 5.7 GeV .

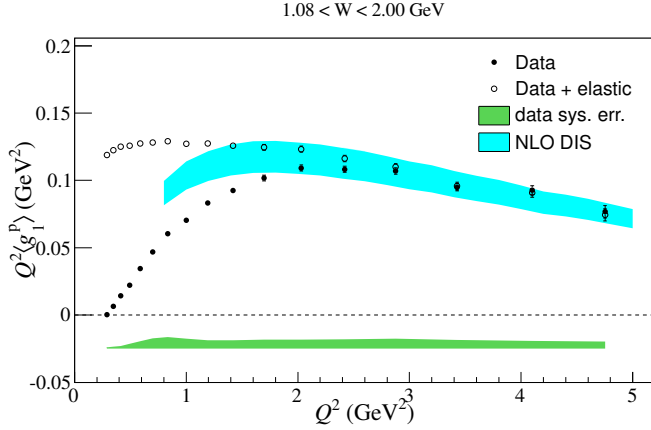


FIG. 39. (Color online) The Q^2 dependence of $Q^2 g_1^p(x, Q^2)$ averaged over a region in x corresponding to $1.08 < W < 2 \text{ GeV}$ (solid circles) for the proton, with the green band showing systematic uncertainties. The open circles represent the data after adding the contribution from ep elastic scattering. The shaded cyan band represents the range of the averages calculated from extrapolated NLO DIS fits.

To test both local and global duality, the data for g_1^p were averaged over x in four Q^2 -dependent intervals corresponding to four regions in $W < 2 \text{ GeV}$, with boundaries at 1.08, 1.38, 1.58, 1.82 and 2.00 GeV (corresponding to the three prominent “resonance bumps” and the region of high-mass resonances observed in our data). Global duality was tested by a single average over x in this entire range in W .

The results for the global duality test are shown in Fig. 39. In this plot we also show the effect of including elastic scattering, following a suggestion of Close and Isgur [144] that including elastic scattering may improve the agreement between the data and the DIS extrapolation. The averaged resonance data agree quite well with the extrapolated DIS data above $Q^2 \approx 2 \text{ GeV}^2$ (without the elastic contribution), suggesting a possible onset of global duality. For $Q^2 < 2 \text{ GeV}^2$, however, the data lie significantly above the DIS extrapolation without the elastic contribution and significantly below the DIS extrapolation with the elastic contribution.

Figure 40 shows the results of the local duality tests for the proton, averaged over x , for four W regions, plotted as a function of Q^2 . At low Q^2 , the data in the first resonance region lie substantially above (below) the NLO curves without (with) the elastic contribution, and the deviation behaves like a power law. Above $Q^2 = 3 \text{ GeV}^2$, the data begin to converge with the NLO curves. The data in the

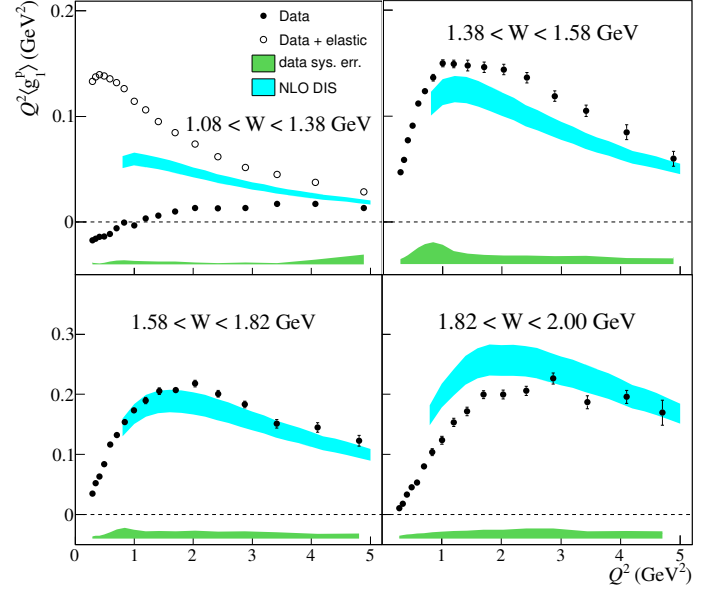


FIG. 40. (Color online) Averages of $Q^2 g_1^p(x, Q^2)$ vs Q^2 over limited spans in x corresponding to prominent “resonance regions” as indicated by the ranges in W . Symbols are the same as in Fig. 39.

second region lie well above the NLO curve. The data in the third resonance region appear in good agreement with the DIS extrapolation. The data in the fourth resonance region lie slightly below the NLO curve. The various local regions seem to compensate each other to yield global duality. However, the approach towards duality is much slower for g_{1p} than in the unpolarized case.

VI. CONCLUSIONS

We have presented the final analysis of the most extensive and precise data set on the spin structure functions A_1^p and g_1^p of the proton collected at Jefferson Laboratory so far. The data cover nearly two orders of magnitude in squared momentum transfer, $0.05 \leq Q^2 \leq 5 \text{ GeV}^2$, which encompasses the transition from the region where hadronic degrees of freedom and effective theories like χ PT near the photon point are relevant to the regime where pQCD is applicable. At lower $W < 2 \text{ GeV}$, our data give more detailed insight in the inclusive response of the proton in the resonance region and how, on average, this connects with the DIS limit (quark-hadron duality). Duality applies both to individual resonances [except the $\Delta(1232)$], and to the resonance region as a whole ($1 \text{ GeV} < W < 2 \text{ GeV}$) above $Q^2 \approx 2 \text{ GeV}^2$. At higher W , $2 \text{ GeV} < W < 3 \text{ GeV}$, and $Q^2 > 1 \text{ GeV}^2$, our data can constrain NLO fits (including higher twist corrections) of spin structure functions. This improves the knowledge of polarized PDFs and sheds new light on the valence quark structure of the nucleon at large x .

Our data also allow a very precise determination of moments of g_1^p , which can be used to test the GDH sum rule limit, compare to χ PT calculations, and extract higher-twist contributions and nucleon polarizabilities. We find that some χ PT are commensurate with our results for γ_0^p at low Q^2 and that the model by Lensky *et al.* [125] agrees with the values obtained for the polarizability γ_0^p at and near the photon point.

Our OPE analysis extracted the twist-4 contribution f_2^p to the first moment of the spin structure function g_1^p . It is found to be negative and the sign of the significant twist coefficients (μ_2 , μ_4 , μ_6 , or μ_8) appears to alternate. This sign alternation is important to understand quark-hadron duality or early scaling seen at relatively low Q^2 . The color polarizabilities extracted from the higher twist analysis are small. The quark spin contribution to the nucleon spin has been extracted in the same process and found to be $\Delta\Sigma = 0.289 \pm 0.014$. The discrepancy previously seen between the $\Delta\Sigma$ extracted from the proton or neutron analyses is resolved by the new data.

Additional data from this experiment on the deuteron with similar precision have already been published [14]. Further information will come from the analysis of the completed EG4 experiment with CLAS, which extends the kinematic coverage of the present data set to even lower Q^2 for a more rigorous test of χ PT. At the highest values of Q^2 ,

spin structure function data from the EG1-dvcs experiment [23] have improved our knowledge of A_1^p at large x and further reduced the uncertainty with which g_1^p is known in the DIS region. Finally, additional information on the structure functions g_2^p and A_2^p is forthcoming from “SANE” in Hall C [49] and “g2p” in Hall A [145]. Extending EG1b to 11 GeV has been approved and will run in the coming years using CLAS12 at Jefferson Laboratory.

ACKNOWLEDGMENTS

We would like to acknowledge the outstanding efforts of the staff of the Accelerator and the Physics Divisions at Jefferson Lab that made this experiment possible. This work was supported in part by the U.S. Department of Energy and the National Science Foundation, the Italian Istituto Nazionale di Fisica Nucleare, the French Centre National de la Recherche Scientifique, the French Commissariat à l’Energie Atomique, the Emmy Noether grant from the Deutsche Forschungsgemeinschaft, the United Kingdom’s Science and Technology Facilities Council, and the National Research Foundation of Korea. The Jefferson Science Associates (JSA) operates the Thomas Jefferson National Accelerator Facility for the United States Department of Energy under Contract No. DE-AC05-06OR23177.

-
- [1] J. Ashman *et al.* (European Muon Collaboration), Phys. Lett. **B206**, 364 (1988).
 - [2] S. Kuhn, J.-P. Chen, and E. Leader, Prog. Part. Nucl. Phys. **63**, 1 (2009).
 - [3] C. A. Aidala, S. D. Bass, D. Hasch, and G. K. Mallot, Rev. Mod. Phys. **85**, 655 (2013).
 - [4] N. Sato, W. Melnitchouk, S. E. Kuhn, J. J. Ethier, and A. Accardi (Jefferson Lab Angular Momentum Collaboration), Phys. Rev. **D93**, 074005 (2016).
 - [5] Y. L. Dokshitzer, Sov. Phys. JETP **46**, 641 (1977).
 - [6] V. N. Gribov and L. N. Lipatov, Yad. Fiz. **15**, 781 (1972).
 - [7] G. Altarelli and G. Parisi, Nucl. Phys. **B126**, 298 (1977).
 - [8] E. V. Shuryak and A. I. Vainshtein, Nucl. Phys. **B201**, 141 (1982).
 - [9] E. V. Shuryak and A. I. Vainshtein, Nucl. Phys. **B199**, 451 (1982).
 - [10] B. Ehrnsperger, A. Schafer, and L. Mankiewicz, Phys. Lett. **B323**, 439 (1994).
 - [11] B. Mecking *et al.* (CLAS Collaboration), Nucl. Instrum. Meth. **A503**, 513 (2003).
 - [12] R. Fatemi *et al.* (CLAS Collaboration), Phys. Rev. Lett. **91**, 222002 (2003).
 - [13] J. Yun *et al.* (CLAS Collaboration), Phys. Rev. **C67**, 055204 (2003).
 - [14] N. Guler *et al.* (CLAS Collaboration), Phys. Rev. **C92**, 055201 (2015).
 - [15] K. Dharmawardane *et al.* (CLAS Collaboration), Phys. Lett. **B641**, 11 (2006).
 - [16] P. Bosted *et al.* (CLAS Collaboration), Phys. Rev. **C75**, 035203 (2007).
 - [17] Y. Prok *et al.* (CLAS Collaboration), Phys. Lett. **B672**, 12 (2009).
 - [18] G. Baum, M. Bergstrom, J. Clendenin, R. Ehrlich, V. Hughes, *et al.*, Phys. Rev. Lett. **45**, 2000 (1980).
 - [19] K. Abe *et al.* (E143 Collaboration), Phys. Rev. Lett. **78**, 815 (1997).
 - [20] M. Amarian *et al.*, Phys. Rev. Lett. **92**, (Jefferson Lab E94-010 Collaboration), 022301 (2004).
 - [21] X. Zheng *et al.* (Jefferson Lab Hall A Collaboration), Phys. Rev. **C70**, 065207 (2004).
 - [22] F. R. Wesselmann *et al.* (RSS Collaboration), Phys. Rev. Lett. **98**, 132003 (2007).
 - [23] Y. Prok *et al.* (CLAS Collaboration), Phys. Rev. **C90**, 025212 (2014).
 - [24] N. Isgur, Phys. Rev. **D59**, 034013 (1999).
 - [25] S. J. Brodsky, M. Burkardt, and I. Schmidt, Nucl. Phys. **B441**, 197 (1995).
 - [26] G. R. Farrar and D. R. Jackson, Phys. Rev. Lett. **35**, 1416 (1975).
 - [27] H. Avakian, S. J. Brodsky, A. Deur, and F. Yuan, Phys. Rev. Lett. **99**, 082001 (2007).
 - [28] J. Soffer and O. V. Teryaev, in *Polarized protons at high-energies—accelerator challenges and physics opportunities. Proceedings, Workshop, Hamburg, Germany, May 17-20, 1999* (1999), hep-ph/9906455, http://inspirehep.net/record/502194/files/teryaev_2.ps.
 - [29] X. Artru, M. Elchikh, J.-M. Richard, J. Soffer, and O. V. Teryaev, Phys. Rept. **470**, 1 (2009).
 - [30] J. Ashman *et al.* (European Muon Collaboration), Nucl. Phys. **B328**, 1 (1989).

- [31] B. Adeva *et al.* (Spin Muon Collaboration), Phys. Rev. **D58**, 112001 (1998).
- [32] E. Ageev *et al.* (COMPASS Collaboration), Phys. Lett. **B647**, 330 (2007).
- [33] V. Alexakhin *et al.* (COMPASS Collaboration), Phys. Lett. **B647**, 8 (2007).
- [34] K. Ackerstaff *et al.* (HERMES Collaboration), Phys. Lett. **B464**, 123 (1999).
- [35] A. Airapetian *et al.* (HERMES Collaboration), Phys. Rev. **D75**, 012007 (2007).
- [36] P. Anthony *et al.* (E142 Collaboration), Phys. Rev. **D54**, 6620 (1996).
- [37] K. Abe *et al.* (E143 collaboration), Phys. Rev. **D58**, 112003 (1998).
- [38] K. Abe *et al.* (E154 Collaboration), Phys. Rev. Lett. **79**, 26 (1997).
- [39] P. Anthony *et al.* (E155 Collaboration), Phys. Lett. **B463**, 339 (1999).
- [40] P. Anthony *et al.* (E155 Collaboration), Phys. Lett. **B493**, 19 (2000).
- [41] P. Anthony *et al.* (E155 Collaboration), Phys. Lett. **B553**, 18 (2003).
- [42] X. Zheng *et al.* (Jefferson Lab Hall A Collaboration), Phys. Rev. Lett. **92**, 012004 (2004).
- [43] A. Airapetian *et al.* (HERMES Collaboration), Eur. Phys. J. **C72**, 1921 (2012).
- [44] O. Filoti, Doctoral Dissertation, University of New Hampshire 2007 (unpublished).
- [45] K. Kramer, D. Armstrong, T. Averett, W. Bertozzi, S. Binet, *et al.*, Phys. Rev. Lett. **95**, 142002 (2005).
- [46] C. Adolph *et al.* (COMPASS Collaboration), Phys. Lett. **B753**, 18 (2016), 1503.08935.
- [47] D. Flay *et al.*, Phys. Rev. **D94**, 052003 (2016).
- [48] O. A. Rondon Aramayo, *Spin Structure at Long Distance: Workshop Proceedings*, edited by J. Chen, K. Slifer, and W. Melnitchouk, AIP Conf.Proc. **1155**, 82 (2009).
- [49] H. Kang (SANE Collaboration), PoS **DIS2013**, 206 (2013).
- [50] E. D. Bloom and F. J. Gilman, Phys. Rev. Lett. **25**, 1140 (1970).
- [51] O. Nachtmann, Nucl. Phys. **B63**, 237 (1973).
- [52] A. De Rujula, H. Georgi, and H. Politzer, Annals Phys. **103**, 315 (1977).
- [53] A. De Rujula, H. Georgi, and H. Politzer, Phys. Lett. **B64**, 428 (1977).
- [54] W. Melnitchouk, R. Ent, and C. Keppel, Phys. Rept. **406**, 127 (2005).
- [55] A. Airapetian *et al.* (HERMES Collaboration), Phys. Lett. **B442**, 484 (1998).
- [56] A. Airapetian *et al.* (HERMES Collaboration), Phys. Rev. Lett. **84**, 2584 (2000).
- [57] P. Solvignon *et al.*, (Jefferson Lab E01-012 Collaboration), Phys. Rev. Lett. **101**, 182502 (2008).
- [58] J. Blumlein and A. Tkabladze, Nucl. Phys. **B553**, 427 (1999).
- [59] S. Wandzura and F. Wilczek, Phys. Lett. **B72**, 195 (1977).
- [60] M. Burkardt, *Spin Structure at Long Distance: Workshop Proceedings*, edited by J. Chen, K. Slifer, and W. Melnitchouk, AIP Conf.Proc. **1155**, 26 (2009).
- [61] H. Burkhardt and W. N. Cottingham, Annals Phys. **56**, 453 (1970).
- [62] O. Gayou, K. Wijesooriya, A. Afanasev, M. Amarian, K. Aniol, *et al.*, Phys. Rev. **C64**, 038202 (2001).
- [63] J. Arrington, W. Melnitchouk, and J. A. Tjon, Phys. Rev. **C76**, 035205 (2007).
- [64] K. Hagiwara *et al.* (Particle Data Group), Phys. Rev. **D66**, 010001 (2002).
- [65] J. D. Bjorken, Phys. Rev. **148**, 1467 (1966).
- [66] J. D. Bjorken, Phys. Rev. **D1**, 1376 (1970).
- [67] S. Larin, T. van Ritbergen, and J. Vermaseren, Phys. Lett. **B404**, 153 (1997).
- [68] E. Stein, P. Gornicki, L. Mankiewicz, and A. Schafer, Phys. Lett. **B353**, 107 (1995).
- [69] X.-D. Ji, in *Baryons '95. Proceedings, 7th International Conference on the Structure of Baryons, Santa Fe, USA, October 3-7, 1995*, edited by B. Gibson, P. Barnes, J. McClelland, and W. Weise (World Scientific Publishing, Singapore, 1995).
- [70] A. Signal, Nucl. Phys. **B497**, 415 (1997).
- [71] I. Balitsky, V. M. Braun, and A. Kolesnichenko, Phys. Lett. **B242**, 245 (1990).
- [72] D. Dolgov, R. Brower, J. W. Negele, and A. Pochinsky, Nucl. Phys. Proc. Suppl. **73**, 300 (1999).
- [73] S. Gerasimov, Sov. J. Nucl. Phys. **2**, 430 (1966).
- [74] S. Drell and A. C. Hearn, Phys. Rev. Lett. **16**, 908 (1966).
- [75] X.-D. Ji, C.-W. Kao, and J. Osborne, Phys. Lett. **B472**, 1 (2000).
- [76] M. Gorchtein, D. Drechsel, M. M. Giannini, E. Santopinto, and L. Tiator, Phys. Rev. **C70**, 055202 (2004).
- [77] A. Deur, P. Bosted, V. Burkert, D. Crabb, V. Dharmawardane, *et al.*, Phys. Rev. **D78**, 032001 (2008).
- [78] C. Leeman, D. Douglas, and G. Krafft, Ann. Rev. Nucl. Part. Sci. **51**, 413 (2001).
- [79] C. Sinclair, P. Adderley, B. Dunham, J. Hansknecht, P. Hartmann, M. Poelker, J. S. Price, P. M. Rutt, W. J. Schneider, and M. Steigerwald, Phys. Rev. ST Accel. Beams **10**, 023501 (2007).
- [80] R. Kazimi *et al.*, in *9th European Particle Accelerator Conference (EPAC 2004) Lucerne, Switzerland, July 5-9, 2004* (2004), <http://accelconf.web.cern.ch/AccelConf/e04/PAPERS/TUPLT154.PDF>.
- [81] M. Stutzman, P. Adderley, J. Brittian, J. Clark, J. Grames, *et al.*, Nucl. Instrum. Meth. **A574**, 213 (2007).
- [82] D. Schultz, J. E. Clendenin, J. Frisch, E. W. Hoyt, L. Klaisner, M. Woods, D. M. Wright, and M. Zolotarev, Conf. Proc. **C920324**, 1029 (1992).
- [83] H. Liu, Nucl. Instrum. Meth. **A400**, 213 (1997).
- [84] J. Grames, Jefferson Lab Technical Note **JLAB-TN-01-029** 2001 (unpublished).
- [85] B. Wagner, H. G. Andresen, K. H. Steffens, W. Hartmann, W. Heil, and E. Reichert, Nucl. Instrum. Meth. **A294**, 541 (1990).
- [86] C. Keith, M. Anghinolfi, M. Battaglieri, P. E. Bosted, D. Branford, *et al.*, Nucl. Instrum. Meth. **A501**, 327 (2003).
- [87] W. de Boer, CERN 74-11, Laboratory I, Nuclear Physics Division 1974 (unpublished).
- [88] M. Borghini, CERN 68-32, Nuclear Physics Division 1974 (unpublished).
- [89] D. Crabb and W. Meyer, Ann. Rev. Nucl. Part. Sci. **47**, 67 (1997).
- [90] M. Mestayer, D. Carman, B. Asavapibhop, F. Barbosa, P. Bonneau, *et al.*, Nucl. Instrum. Meth. **A449**, 81 (2000).
- [91] E. Smith, T. Carstens, J. Distelbrink, M. Eckhause, H. Egiian, *et al.*, Nucl. Instrum. Meth. **A432**, 265 (1999).
- [92] G. Adams, V. Burkert, R. Carl, T. Carstens, V. Frolov, *et al.* Nucl. Instrum. Meth. **A465**, 414 (2001).

- [93] M. Amarian, G. Asryan, K. Beard, W. Brooks, V. Burkert, *et al.* Nucl. Instrum. Meth. **A460**, 239 (2001).
- [94] V. Dharmawardane, Ph.D. dissertation, Old Dominion University 2004 (unpublished).
- [95] R. Dalitz, Proc. Phys. Soc., London, Sect. **A64**, 667 (1951).
- [96] T. Gehrmann and M. Stratmann, Phys. Rev. **D56**, 5839 (1997).
- [97] P. Bosted, S. Kuhn, and Y. Prok, CLAS Note 2003-008, Jefferson Lab 2003, https://www.jlab.org/Hall-B/notes/clas_notes03/03-008.pdf.
- [98] W. Yao *et al.* (Particle Data Group), J.Phys.G **G33**, 1 (2006).
- [99] W. R. Leo, *Techniques for Nuclear and Particle Physics Experiments* (Springer, Berlin, 1994).
- [100] M. Bellis, CLAS Note 2002-016, Jefferson Lab (2002), https://www.jlab.org/Hall-B/notes/clas_notes02/02-016a.pdf.
- [101] P. Bosted and H. Avakian, CLAS Note 2006-006, Jefferson Lab 2006 (unpublished).
- [102] A. Klimenko and S. Kuhn, CLAS Note 2003-005, Old Dominion University (2003), https://www.jlab.org/Hall-B/notes/clas_notes03/03-005.pdf.
- [103] F. James and M. Roos, Computer Physics Communications **10**, 343 (1975).
- [104] H. De Vries, C. De Jager, and C. De Vries, Atom.Data Nucl.Data Tabl. **36**, 495 (1987).
- [105] M. E. Christy and P. E. Bosted, Phys. Rev. **C81**, 055213 (2010).
- [106] P. Bosted *et al.* (CLAS Collaboration), Phys. Rev. **C78**, 015202 (2008).
- [107] P. Norton, Rept. Prog. Phys. **66**, 1253 (2003).
- [108] L. W. Mo and Y.-S. Tsai, Rev. Mod. Phys. **41**, 205 (1969).
- [109] J. Arrington, Phys. Rev. **C69**, 022201 (2004).
- [110] P. E. Bosted, Phys. Rev. **C51**, 409 (1995).
- [111] O. A. Rondon-Aramayo, Phys. Rev. **C60**, 035201 (1999).
- [112] T. Kukhto and N. Shumeiko, Nucl. Phys. **B219**, 412 (1983).
- [113] Jefferson Lab Experiment CLAS Database, <http://clasweb.jlab.org/physicsdb>.
- [114] See Supplemental Material at <http://link.aps.org/supplemental/10.1103/PhysRevC.96.065208> for the complete tables of experimental results presented in this publication.
- [115] Y. Liang *et al.* (E94-110 Collaboration), (2004).
- [116] K. Helbing, Prog. Part. Nucl. Phys. **57**, 405 (2006).
- [117] D. Drechsel, O. Hanstein, S. Kamalov, and L. Tiator, Nucl. Phys. **A645**, 145 (1999).
- [118] S. Kamalov, D. Drechsel, O. Hanstein, L. Tiator, and S. Yang, Nucl. Phys. **A684**, 321 (2001).
- [119] I. G. Aznauryan and V. D. Burkert, Prog. Part. Nucl. Phys. **67**, 1 (2012), 1109.1720.
- [120] C. R. Bourrely, J. Soffer, and F. Buccella, Eur. Phys. J. **C41**, 327 (2005).
- [121] E. Leader, A. V. Sidorov, and D. B. Stamenov, Phys. Rev. **D75**, 074027 (2007).
- [122] V. Burkert and B. Ioffe, J. Exp.Theor. Phys. **78**, 619 (1994).
- [123] V. Burkert and B. Ioffe, Phys. Lett. **B296**, 223 (1992).
- [124] R. S. Pasechnik, D. V. Shirkov, O. V. Teryaev, O. P. Solovtsova, and V. L. Khandramai, Phys. Rev. **D81**, 016010 (2010).
- [125] V. Lensky, J. M. Alarcn, and V. Pascalutsa, Phys. Rev. **C90**, 055202 (2014).
- [126] V. Bernard, T. R. Hemmert, and U.-G. Meissner, Phys. Rev. **D67**, 076008 (2003).
- [127] V. Burkert and Z.-j. Li, Phys. Rev. **D47**, 46 (1993).
- [128] J. Soffer and O. Teryaev, Phys. Rev. Lett. **70**, 3373 (1993).
- [129] J. Soffer and O. Teryaev, Phys. Rev. **D70**, 116004 (2004).
- [130] V. Nazaryan, C. E. Carlson, and K. A. Griffioen, Phys. Rev. Lett. **96**, 163001 (2006).
- [131] A. Deur, Y. Prok, V. Burkert, D. Crabb, F. X. Girod, K. A. Griffioen, N. Guler, S. E. Kuhn, and N. Kvaltine, Phys. Rev. **D90**, 012009 (2014).
- [132] S. Bass and M. M. Brisudova, Eur. Phys. J. **A4**, 251 (1999).
- [133] O. Gayou *et al.* (Jefferson Lab Hall A Collaboration), Phys. Rev. Lett. **88**, 092301 (2002).
- [134] J. Blumlein and H. Bottcher, Nucl. Phys. **B636**, 225 (2002).
- [135] K. A. Olive *et al.* (Particle Data Group), Chin. Phys. **C38**, 090001 (2014).
- [136] Z. Meziani, W. Melnitchouk, J.-P. Chen, S. Choi, T. Averett, *et al.*, Phys. Lett. **B613**, 148 (2005).
- [137] A. Deur, arXiv:nucl-ex/0508022 (unpublished).
- [138] J.-P. Chen, A. Deur, and Z.-E. Meziani, Mod.Phys. Lett. **A20**, 2745 (2005).
- [139] N.-Y. Lee, K. Goeke, and C. Weiss, Phys. Rev. **D65**, 054008 (2002).
- [140] A. Deur, P. E. Bosted, V. Burkert, G. Cates, J.-P. Chen, *et al.*, Phys. Rev. Lett. **93**, 212001 (2004).
- [141] J. Ahrens *et al.* (GDH, A2), Phys. Rev. Lett. **87**, 022003 (2001).
- [142] H. Dutz *et al.* (GDH), Phys. Rev. Lett. **91**, 192001 (2003).
- [143] R. P. Hildebrandt, H. W. Griesshammer, T. R. Hemmert, and B. Pasquini, Eur. Phys. J. **A20**, 293 (2004).
- [144] F. E. Close and N. Isgur, Phys. Lett. **B509**, 81 (2001).
- [145] K. Slifer, *Spin Structure at Long Distance: Workshop Proceedings*, edited by J. Chen, K. Slifer, and W. Melnitchouk, AIP Conf. Proc. **1155**, 125 (2009).